

DOT/FAA/TC-21/56

Federal Aviation Administration
William J. Hughes Technical Center
Aviation Research Division
Atlantic City International Airport
New Jersey 08405

T800-F3900 Composite Stacked Ply Laminate Testing and Modeling Using MAT_213

May 2022

Final report



U.S. Department of Transportation
Federal Aviation Administration

NOTICE

This document is disseminated under the sponsorship of the U.S. Department of Transportation in the interest of information exchange. The U.S. Government assumes no liability for the contents or use thereof. The U.S. Government does not endorse products or manufacturers. Trade or manufacturers' names appear herein solely because they are considered essential to the objective of this report. The findings and conclusions in this report are those of the author(s) and do not necessarily represent the views of the funding agency. This document does not constitute FAA policy. Consult the FAA sponsoring organization listed on the Technical Documentation page as to its use.

This report is available at the Federal Aviation Administration William J. Hughes Technical Center's Full-Text Technical Reports page: actlibrary.tc.faa.gov in Adobe Acrobat portable document format (PDF).

Form DOT F 1700.7 (8-72)

Reproduction of completed page authorized

| | | | | | |
|---|--|--|---|---|--|
| 1. Report No. DOT/FAA/TC-21/56 | | 2. Government Accession No. | | 3. Recipient's Catalog No. | |
| 4. Title and Subtitle T800-F3900 Composite Stacked Ply Laminate Testing and Modeling Using MAT_213 | | | | 5. Report Date May 2022 | |
| | | | | 6. Performing Organization Code | |
| 7. Author(s) Nathan Holt, Bilal Khaled, Loukham Shyamsunder and Subramaniam Rajan | | | | 8. Performing Organization Report No. | |
| 9. Performing Organization Name and Address School of Sustainable Engineering and the Built Environment Arizona State University 660 South College Ave Tempe, AZ 85281-3005 | | | | 10. Work Unit No. (TRAIS) | |
| | | | | 11. Contract or Grant No. FAA Grant 12-G-001 | |
| 12. Sponsoring Agency Name and Address Federal Aviation Administration Aircraft Certification Service Policy and Innovation Division (AIR-600) 800 Independence Avenue SW Washington, DC 20591 | | | | 13. Type of Report and Period Covered Final Report | |
| | | | | 14. Sponsoring Agency Code AIR-600 | |
| 15. Supplementary Notes The Federal Aviation Administration Aviation William J. Hughes Technical Center Research Division COR was William Emmerling. | | | | | |
| 16. Abstract Simulating uncontained engine fragment impact to composite aircraft structures requires material models, which can accurately account for the deformation, damage, and failure experienced during these highly dynamic events. The FAA Aircraft Catastrophic Failure Prevention Program sponsored the development of a new material model known as MAT_213 to model composite impact, which has been implemented into the commercial finite element software LS-DYNA. This report provides results for stacked-ply T800/F3900 carbon fiber reinforced polymer composite validation tests conducted at room temperature with uniaxial tension and compression loads applied at quasi-static rates by Arizona State University. Stress concentration validation tests were also conducted on stacked-ply specimens with a centered hole. Digital Image Correlation was used to obtain the experimental surface strain contours. MAT_213 was used to conduct simulations comparing stress-strain relationships, strain profiles, and displacement results to the experiments. The MAT_213 material inputs were obtained from specimen tests performed previously. Additionally, as part of this study, delamination tests were conducted using end notch flexure and double cantilevered beam specimens to characterize mode I and mode II fracture properties of the T800/F3900 composite. These experimental results were used to build models with MAT_138 cohesive zone elements for the interlaminar polymer matrix between the composite ply layers modeled with MAT_213. The test results were necessary to calibrate numerical inputs to the traction separation laws governing the delamination behavior. Scanning electron microscope analysis was also utilized to examine specimens in the untested, damaged, and failed states. The results provided insight to the microstructural damage induced from manufacturing, specimen preparation processing, and loading of the T800/F3900 composite. | | | | | |
| 17. Key Words MAT_213, T800/F3900, composite, orthotropic plasticity, material characterization testing, damage, failure, cohesive zone modeling, LS-DYNA, explicit finite element analysis, impact simulation | | | 18. Distribution Statement This document is available to the U.S. public through the National Technical Information Service (NTIS), Springfield, Virginia 22161. This document is also available from the Federal Aviation Administration William J. Hughes Technical Center at actlibrary.tc.faa.gov . | | |
| 19. Security Classif. (of this report) Unclassified | | 20. Security Classif. (of this page) Unclassified | | 21. No. of Pages 153 | 19. Security Classif. (of this report) Unclassified |

Contents

| | | |
|----------|--|-----------|
| 1 | Overview | 1 |
| 1.1 | Introduction | 1 |
| 2 | Background | 3 |
| 2.1 | Stacked-ply validation..... | 3 |
| 2.2 | Fracture mode tests..... | 4 |
| 2.3 | SEM imaging..... | 5 |
| 3 | General experimental test procedures | 6 |
| 3.1 | Sample preparation..... | 6 |
| 3.2 | Test machines, fixtures, equipment, and software | 10 |
| 3.3 | Typical test procedure | 14 |
| 3.4 | Post-processing of test data | 14 |
| 4 | Stacked-ply experimental test details and results | 18 |
| 4.1 | Overview | 18 |
| 4.2 | Stacked-ply tension test..... | 18 |
| 4.3 | Stacked-ply compression test..... | 22 |
| 4.4 | Stacked-ply tension stress concentration test..... | 26 |
| 4.5 | Stacked-ply compression stress concentration test | 31 |
| 4.6 | Experimental observations | 36 |
| 5 | QS-RT fracture mode test details and results | 37 |
| 5.1 | Overview | 37 |
| 5.2 | General experimental procedures..... | 38 |
| 5.2.1 | Sample preparation | 38 |
| 5.2.2 | Test machines, fixtures, equipment and software | 41 |
| 5.2.3 | Typical test procedure..... | 44 |
| 5.2.4 | Post-processing of test data..... | 48 |
| 5.3 | Experimental results..... | 49 |

| | | |
|----------|--|-----------|
| 5.3.1 | ENF Test | 49 |
| 5.3.2 | DCB Test | 53 |
| 5.4 | Simulation details | 60 |
| 5.5 | Simulation results | 64 |
| 5.5.1 | ENF test | 64 |
| 5.5.2 | DCB test | 66 |
| 6 | LS-DYNA simulation of QS-RT stacked-ply validation tests using MAT213 | 69 |
| 6.1 | LS-DYNA simulation overview | 69 |
| 6.2 | General modeling techniques | 69 |
| 6.3 | LS-DYNA simulation of stacked-ply tension | 72 |
| 6.3.1 | Simulation modeling | 72 |
| 6.3.2 | Validation metrics | 74 |
| 6.3.3 | Results | 77 |
| 6.3.4 | Discussion | 80 |
| 6.4 | LS-DYNA simulation of stacked-ply compression | 82 |
| 6.4.1 | Simulation modeling | 82 |
| 6.4.2 | Validation metrics | 83 |
| 6.4.3 | Results | 83 |
| 6.4.4 | Discussion | 88 |
| 6.5 | LS-DYNA simulation of stacked-ply tension – stress concentration test | 88 |
| 6.5.1 | Simulation modeling | 88 |
| 6.5.2 | Validation metrics | 92 |
| 6.5.3 | Results | 96 |
| 6.5.4 | Discussion | 103 |
| 6.6 | LS-DYNA simulation of stacked-ply compression – stress concentration test | 104 |
| 6.6.1 | Simulation modeling | 104 |
| 6.6.2 | Validation metrics | 105 |
| 6.6.3 | Results | 107 |

| | | |
|----------|--|------------|
| 6.6.4 | Discussion..... | 115 |
| 7 | SEM imaging for MAT213 model validation | 116 |
| 7.1 | Objective | 116 |
| 7.2 | Procedure..... | 116 |
| 7.3 | Results | 121 |
| 7.3.1 | Virgin sample..... | 121 |
| 7.3.2 | Damaged sample..... | 124 |
| 7.3.3 | Failed sample | 125 |
| 7.3.4 | Failed shear sample..... | 130 |
| 8 | Concluding remarks | 134 |
| 9 | References | 135 |

Figures

| | |
|--|----|
| Figure 1. Microscopy images of T800/F3900 (a) SEM 3600x (b) SEM 65x (c) Optical 1500x (d) Optical 200x..... | 2 |
| Figure 2. Stacked-ply layup | 2 |
| Figure 3. Optical microscopy images of finished edges (after grinding) (a) 200x, (b) 400x, (c) 500x, (d) 1000x..... | 8 |
| Figure 4. Close up of a typical speckled surface | 10 |
| Figure 5. Experimental equipment (a) Test frame, (b) Hydraulic grips, (c) CLC compression fixture top, and (d) CLC fixture front | 11 |
| Figure 6. (a) Two DIC cameras and high-speed camera (b) LED lighting fixture..... | 12 |
| Figure 7. Typical SGS (a) Tension specimens (b) Compression specimens | 13 |
| Figure 8. Dual DIC systems setup | 14 |
| Figure 9. Strain measurement areas for stress concentration tests..... | 16 |
| Figure 10. Typical specimen geometry and layout (all dimensions in inches)..... | 18 |
| Figure 11. Example image of tension specimen prior to testing..... | 19 |
| Figure 12. Tension specimens after testing (a)(b)(c) V-T-4, (d)(e)(f) V-T-5, (g)(h)(i) V-T-6..... | 20 |
| Figure 13. Tension stress-strain curves..... | 21 |
| Figure 14. Typical specimen geometry and layout (all dimensions in inches)..... | 22 |
| Figure 15. Compression specimens prior to testing (a) V-C-2, (b) V-C-3, (c) V-C-4..... | 23 |
| Figure 16. Compression specimens after testing (a) V-C-2 XY surface (b) V-C-2 through thickness (c) V-C-3 XY surface (d) V-C-3 through thickness | 24 |
| Figure 17. Compression stress-strain curves | 25 |
| Figure 18. Typical specimen geometry and layout (all dimensions in inches)..... | 26 |
| Figure 19. Tension specimens prior to testing (a) V-TH-2, (b) V-TH-3, (c) V-TH-4..... | 27 |
| Figure 20. Tension stress concentration specimens after testing (a)(b)(c) V-TH-2, (d)(e)(f) V-TH-3, (g)(h)(i) V-TH-4 | 28 |
| Figure 21. Tension stress concentration RL of hole ϵ_{yy} vs. time..... | 29 |
| Figure 22. Tension stress concentration: above hole ϵ_{xx} vs. time | 30 |
| Figure 23. Tension stress concentration: below hole ϵ_{xx} vs. time..... | 30 |
| Figure 24. Typical specimen geometry and layout (all dimensions in inches)..... | 31 |
| Figure 25. Compression specimens prior to testing (a) V-CH-5, (b) V-CH-7, (c) V-CH-8..... | 32 |
| Figure 26. Compression Stress Concentration specimens after testing (a)(b)(c) V-CH-5, (d)(e)(f) V-CH-7, (g)(h)(i) V-CH-8 | 33 |

| | |
|---|----|
| Figure 27. Compression stress concentration RL of hole ϵ_{yy} vs. time | 34 |
| Figure 28. Compression stress concentration: above hole ϵ_{xx} vs. time..... | 35 |
| Figure 29. Compression stress concentration: below hole ϵ_{xx} vs. time..... | 35 |
| Figure 30. Traction-separation law used in MAT 138..... | 37 |
| Figure 31. ENF and DCB manufactured boards showing test coupons cut from the original panel | 39 |
| Figure 32. Piano hinges for DCB test | 39 |
| Figure 33. Test machines and fixtures (a) MTS load frame (b) Spring loaded grips front view (c) Spring loaded grips side view (d) 3-point bend fixture | 42 |
| Figure 34. Typical camera setup for ENF and DCB tests, Tokina 100 mm lens (top) and Schneider 35 mm lens (bottom)..... | 43 |
| Figure 35. Tokina 100 mm lens on Point Grey Grasshopper 3 camera | 43 |
| Figure 36. DCB test setup..... | 44 |
| Figure 37. DCB test | 45 |
| Figure 38. ENF 3-point test setup..... | 47 |
| Figure 39. ENF test..... | 48 |
| Figure 40. Y-displacement DIC data for DCB test..... | 48 |
| Figure 41. COD tool on ENF specimen..... | 49 |
| Figure 42. COD tool on DCB specimen | 49 |
| Figure 43. Typical specimen geometry and layout..... | 50 |
| Figure 44. Example image of ENF specimen before testing (a) Top surface showing specimen width (b) Side of specimen showing thickness..... | 50 |
| Figure 45. Example image of ENF specimen after testing (a) Top surface showing specimen width (b) Side of specimen showing thickness..... | 51 |
| Figure 46. ENF precrack experimental force vs. displacement | 52 |
| Figure 47. Typical specimen geometry and layout..... | 53 |
| Figure 48. Example image of DCB specimen prior to testing (a) Top surface showing specimen width (b) Side of specimen showing thickness..... | 54 |
| Figure 49. Example image of DCB specimen after testing (a) Exterior top and bottom surfaces (b) Interior surfaces (c) Film (d) Initial crack area | 55 |
| Figure 50. DCB precrack experimental force vs. displacement | 56 |
| Figure 51. DCB tests crack resistance curve | 59 |
| Figure 52. GIC versus crack tip opening displacement | 59 |
| Figure 53. ENF experimental geometry and BCs..... | 60 |
| Figure 54. ENF simulation geometry and BCs..... | 61 |
| Figure 55. DCB experimental geometry and BCs | 61 |

| | |
|---|----|
| Figure 56. DCB simulation geometry and BCs | 61 |
| Figure 57. DCB Mesh 1-1 cohesive zone layer | 62 |
| Figure 58. DCB Mesh 4 - 23 cohesive zone layers..... | 63 |
| Figure 59. Mode II sensitivity study (a) ET (b) S..... | 64 |
| Figure 60. Force vs. displacement simulation and experimental comparison | 65 |
| Figure 61. Mode II final traction separation curve | 66 |
| Figure 62. Mode II sensitivity study (a) ET (b) S..... | 66 |
| Figure 63. Force vs. displacement simulation and experimental comparison | 67 |
| Figure 64. Mode I final traction separation curve..... | 68 |
| Figure 65. Elevation XZ plane view of the FE model | 69 |
| Figure 66. Energy plot for tension simulation | 71 |
| Figure 67. Experimental test conditions, XY plane..... | 72 |
| Figure 68. Experimental test conditions, YZ plane | 72 |
| Figure 69. Simulation test conditions, XY plane..... | 73 |
| Figure 70. Simulation test conditions, YZ plane | 73 |
| Figure 71. VIC 3D digital extensometers used for metric 2..... | 76 |
| Figure 72. Metric 3 y-reaction nodes..... | 77 |
| Figure 73. Metric 1 - ϵ_{xx} comparison | 77 |
| Figure 74. Metric 1 - ϵ_{yy} comparison | 78 |
| Figure 75. Metric 2 - x-displacement comparison | 78 |
| Figure 76. Metric 2 - y-displacement comparison | 79 |
| Figure 77. Metric 3 - stress-strain comparison | 79 |
| Figure 78. Y-Strain fringe plot of tension test, at $t = 250$ s (a) Simulation (b) Experiment..... | 80 |
| Figure 79. Compression comparison node and element..... | 83 |
| Figure 80. Metric 1 - ϵ_{xx} comparison | 84 |
| Figure 81. Metric 1 - ϵ_{yy} comparison | 84 |
| Figure 82. Metric 2 - x-displacement comparison | 85 |
| Figure 83. Metric 2 - y-displacement comparison | 85 |
| Figure 84. Metric 3 - stress-strain comparison | 86 |
| Figure 85. Y-Strain fringe plot of compression test, at $t = 150$ s (a) Simulation (b) Experiment | 87 |
| Figure 86. Experimental test conditions, XY plane..... | 89 |
| Figure 87. Experimental test conditions, YZ plane | 89 |
| Figure 88. Simulation test conditions, XY plane..... | 90 |
| Figure 89. Simulation test conditions, YZ plane | 90 |
| Figure 90. Coarse mesh validation measurement locations..... | 92 |
| Figure 91. Medium mesh validation measurement locations | 93 |

| | |
|---|-----|
| Figure 92. Fine mesh validation measurement locations..... | 93 |
| Figure 93. DIC measurement areas..... | 94 |
| Figure 94. Metric 1 - ϵ_{xx} comparison | 96 |
| Figure 95. Metric 1 - ϵ_{yy} comparison | 96 |
| Figure 96. Metric 1 - ϵ_{xy} comparison | 97 |
| Figure 97. Metric 2 - above hole ϵ_{xx} comparison..... | 97 |
| Figure 98. Metric 2 - above hole ϵ_{yy} comparison..... | 98 |
| Figure 99. Metric 2 - above hole ϵ_{xy} comparison..... | 98 |
| Figure 100. Metric 2 - below hole ϵ_{xx} comparison | 99 |
| Figure 101. Metric 2 - below hole ϵ_{yy} comparison | 99 |
| Figure 102. Metric 2 - below hole ϵ_{xy} comparison | 100 |
| Figure 103. Metric 3 - x-direction displacement | 100 |
| Figure 104. Metric 3 - y-direction displacement | 101 |
| Figure 105. Y-Strain fringe plot of tension-hole test, at t = 325 s (a) Simulation (b) Experiment | 102 |
| Figure 106. Coarse mesh validation measurement locations..... | 106 |
| Figure 107. Medium mesh validation measurement locations | 106 |
| Figure 108. Fine mesh validation measurement locations..... | 107 |
| Figure 109. Metric 1 - ϵ_{xx} comparison | 108 |
| Figure 110. Metric 1 - ϵ_{yy} comparison | 108 |
| Figure 111. Metric 1 - ϵ_{xy} comparison | 109 |
| Figure 112. Metric 2 - above hole ϵ_{xx} comparison..... | 110 |
| Figure 113. Metric 2 - above hole ϵ_{yy} comparison..... | 110 |
| Figure 114. Metric 2 - above hole ϵ_{xy} comparison..... | 111 |
| Figure 115. Metric 2 - below hole ϵ_{xx} comparison | 111 |
| Figure 116. Metric 2 - below hole ϵ_{yy} comparison | 112 |
| Figure 117. Metric 2 - below hole ϵ_{xy} comparison | 112 |
| Figure 118. Metric 3 - x-direction displacement | 113 |
| Figure 119. Metric 3 - y-direction displacement | 113 |
| Figure 120. Y-Strain fringe plot of compression-hole test, at t = 155 s (a) Simulation (b) Experiment..... | 114 |
| Figure 121. Epoxy set components (a) Resin (b) Hardener..... | 117 |
| Figure 122. Epoxy embedding equipment (a) Vacuum chamber (b) Sample holder | 118 |
| Figure 123. Grinding and polishing equipment (a) Allied machine specimen holder (b) Allied machine..... | 118 |

| | |
|---|-----|
| Figure 124. Polishing materials (a) RedLube (b) Diamond suspension (c) Colloidal silica suspension..... | 119 |
| Figure 125. Example of half polished specimen..... | 120 |
| Figure 126. SEM imaging equipment (a) XL30 ESEM FEG (b) Sputter coater..... | 121 |
| Figure 127. Virgin sample before cutting..... | 121 |
| Figure 128. Virgin sample cutting layout..... | 122 |
| Figure 129. Virgin sample 500x..... | 122 |
| Figure 130. Virgin sample (a) 3500x (b) 5000x..... | 123 |
| Figure 131. Virgin sample (a) 5000x (b) 6500x..... | 123 |
| Figure 132. Damaged sample before cutting..... | 124 |
| Figure 133. Damaged sample cutting layout..... | 124 |
| Figure 134. Damaged sample (a) 800x (b) 5000x..... | 125 |
| Figure 135. Damaged sample (a) 2500x (b) 6500x..... | 125 |
| Figure 136. Failed sample before cutting (a) Width (b) Through thickness..... | 126 |
| Figure 137. Failed sample cutting layout..... | 126 |
| Figure 138. Failed sample 36x damage away from complete fracture zone..... | 127 |
| Figure 139. Failed sample (a) 250x (b) 50x..... | 127 |
| Figure 140. Failed sample (a) 36x (b) 250x..... | 128 |
| Figure 141. Failed sample (a) 250x (b) 2000x..... | 128 |
| Figure 142. Failed sample (a) 1000x (b) 3500x..... | 129 |
| Figure 143. Failed-shear sample before cutting (a) Whole specimen (b) Gage area..... | 130 |
| Figure 144. Failed-shear sample cutting layout..... | 131 |
| Figure 145. Failed-shear sample (a) 36x (b) 650x..... | 132 |
| Figure 146. Failed-shear sample (a) 1200x (b) 1200x..... | 132 |
| Figure 147. Failed-shear sample (a) 40x (b) 1000x..... | 133 |

Tables

| | |
|--|----|
| Table 1. T800/F3900 Manufacturer Reported Material Properties | 1 |
| Table 2. Waterjet Specifications | 6 |
| Table 3. 80-Grit (US Std) Specifications | 7 |
| Table 4. Grinding Wheel Specifications | 7 |
| Table 5. 46-Grit (Grinding Wheel) Specifications | 7 |
| Table 6. Descriptions of the parameters used in this report..... | 17 |
| Table 7. Tension test specimen dimensions..... | 18 |
| Table 8. Summary of tension test results | 21 |
| Table 9. Compression test specimen dimensions | 22 |
| Table 10. Summary of compression test results | 24 |
| Table 11. Tension stress concentration test specimen dimensions | 26 |
| Table 12. Summary of tension stress concentration test results | 29 |
| Table 13. Compression stress concentration test specimen dimensions..... | 31 |
| Table 14. Summary of compression stress concentration test results..... | 34 |
| Table 15. MAT 138 parameter summary..... | 38 |
| Table 16. ENF Test Specimen Dimensions | 50 |
| Table 17. Test Summary for ENF Non-precracked Tests..... | 51 |
| Table 18. Test Summary for ENF Precracked Tests..... | 52 |
| Table 19. ENF Experimental Regression Specifications | 53 |
| Table 20. DCB Test Specimen Dimensions | 53 |
| Table 21. DCB experimental regression specifications | 56 |
| Table 22. Test summary for DCB non-precracked tests..... | 57 |
| Table 23. Test summary for DCB precracked tests – non-linear..... | 57 |
| Table 24. Test summary for DCB precracked tests – visible | 57 |
| Table 25. Test summary for DCB precracked tests – maximum..... | 58 |
| Table 26. ENF and DCB meshes | 62 |
| Table 27. ENF and DCB simulation specifications | 63 |
| Table 28. Simulation regression specifications | 65 |
| Table 29. Final Mode II MAT 138 parameters | 65 |
| Table 30. Simulation regression specifications | 68 |
| Table 31. Final Mode I MAT 138 parameters | 68 |
| Table 32. MAT138 input deck..... | 68 |
| Table 33. Model parameter specification..... | 70 |

| | |
|--|-----|
| Table 34. FE model meshes | 74 |
| Table 35. Validation metrics description | 74 |
| Table 36. Tension test metric 1 | 75 |
| Table 37. Tension test metric 2..... | 75 |
| Table 38. Tension test metric 3..... | 76 |
| Table 39. Polynomial regression fitting of tension simulation metrics | 81 |
| Table 40. FE model meshes | 82 |
| Table 41. FE model meshes | 91 |
| Table 42. Validation metrics description | 94 |
| Table 43. Tension hole test metric 1 | 95 |
| Table 44. Tension hole test metric 2..... | 95 |
| Table 45. Tension hole test metric 3..... | 95 |
| Table 46. Polynomial regression fitting of tension with hole simulation metrics | 103 |
| Table 47. FE model meshes | 104 |
| Table 48. MAT213 Specifications..... | 107 |
| Table 49. Polynomial regression fitting of compression with hole simulation metrics..... | 115 |
| Table 50. SEM image samples..... | 116 |
| Table 51. Grinding and polishing procedure | 119 |

Acronyms

| Acronym | Definition |
|----------------|---|
| ASTM | American Society for Testing and Materials |
| CZM | Cohesive Zone Model |
| CLC | Combined Loading Compression |
| CC | Compliance calibration |
| COD | Crack opening data |
| DIC | Digital Image Correlation |
| DCB | Double Cantilever Beam |
| ENF | End Notched Flexure |
| FAA | Federal Aviation Administration |
| FE | Finite Element |
| MCC | Modified compliance calibration |
| NASA | National Aeronautics and Space Administration |
| QS | Quasi-static |
| RCMBT | Rotation corrected modified beam theory |
| RT | Room Temperature |
| SEM | Scanning Electron Microscope |

Executive summary

Simulating uncontained engine fragment impact to composite aircraft structures requires material models, which can accurately account for the deformation, damage, and failure experienced during these highly dynamic events. The FAA Aircraft Catastrophic Failure Prevention Program sponsored development of a new material model known as MAT_213 to model composite impact, which has been implemented into the commercial finite element software LS-DYNA. This report provides results for stacked-ply T800/F3900 carbon fiber reinforced polymer composite validation tests conducted at room temperature with uniaxial tension and compression loads applied at quasi-static rates by Arizona State University. Stress concentration validation tests were conducted on stacked-ply specimens with a centered hole. Digital Image Correlation was used to obtain the experimental surface strain contours.

MAT_213 was used to conduct simulations comparing stress-strain relationships, strain profiles, and displacement results to the experiments. The MAT_213 material inputs were obtained from specimen tests performed previously. Additionally as part of this study, delamination tests were conducted using end notch flexure and double cantilevered beam specimens to characterize mode I and mode II fracture properties of the T800/F3900 composite. These experimental results were used to build models with MAT_138 cohesive zone elements for the interlaminar polymer matrix between the composite ply layers modeled with MAT_213. The test results were necessary to calibrate numerical inputs to the traction separation laws governing the delamination behavior. Scanning electron microscope analysis was utilized to examine specimens in the untested, damaged, and failed states. The results provided insight to the microstructural damage induced from manufacturing, specimen preparation processing, and loading of the T800/F3900 composite.

1 Overview

1.1 Introduction

This report summarizes (a) the experimental procedures and results obtained from testing various structural forms of the T800-F3900 composite material manufactured by Toray Composites, Seattle, WA, and (b) numerical simulation of these tests using the MAT213 material model implemented in the LS-DYNA finite element program [MAT213 V1.3 α -1]. The tests were performed at quasi-static (QS) and room temperature (RT) conditions and include stacked-ply tension and compression tests, as well as fracture mode analysis tests. Details of the MAT213 material model and its implementation in LS-DYNA are available publicly (Goldberg, et al., 2016) (Harrington, et al., 2017) (Hoffarth, et al., 2016) and are not duplicated in this report.

The material properties reported by Toray Composites are shown in Table 1 and are the averages of multiple replicates.

Table 1. T800/F3900 Manufacturer Reported Material Properties

| Characteristic | Reported Value |
|-------------------------------------|-----------------------|
| Resin Content Beginning (%) | 34.8 |
| Resin Content Ending (%) | 35.4 |
| Ultimate Tensile Strength (psi) | 434 000 |
| Tensile Modulus (psi) | 22 000 000 |
| Tensile Strain at Failure (in/in) | 0.0177 |
| Ultimate Compressive Strength (psi) | 214 000 |

Figure 1 shows the structure of the composite. The images show the composite at varying levels of magnification. A scanning electron microscope (SEM) captured Figure 1(a-b) and Figure 1(c-d) were captured using optical microscopy. The images depict the fibers, matrix, and the interlaminar layers.

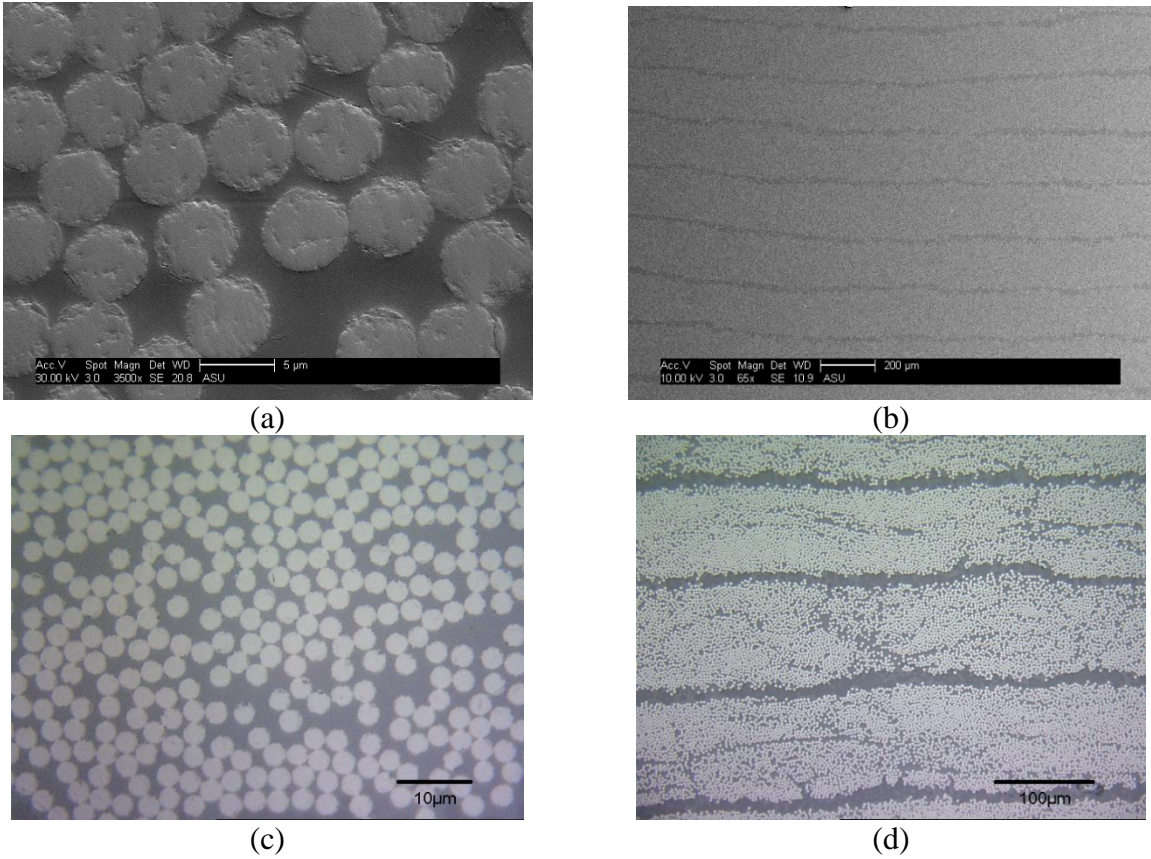


Figure 1. Microscopy images of T800/F3900 (a) SEM 3600x (b) SEM 65x (c) Optical 1500x (d) Optical 200x

All stacked-ply validation tests had a laminate lay-up that was $[0/90/45/-45]_s$. Figure 2 shows the 8-ply layup.

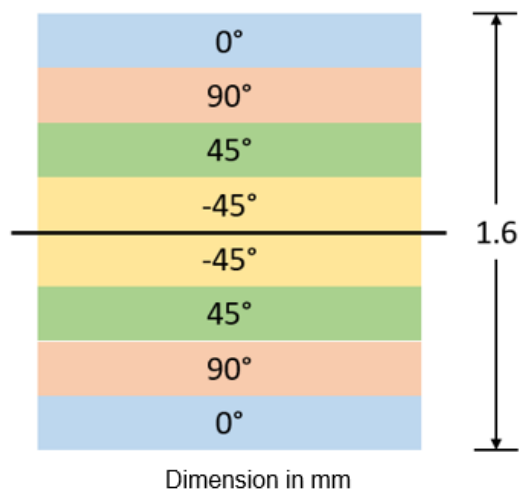


Figure 2. Stacked-ply layup

Four types of stacked-ply validation tests were performed: tension, compression, open-hole tension, and open-hole compression. Dimensions of the test coupons were specific to the type of test performed. These tests served to provide validation data for MAT213's deformation, damage, and failure sub-models. The tension and compression tests validated the model's ability to predict stress-strain relationships for simple geometries, while the stress concentration tests provided validation for more complicated geometries.

Two types of fracture analysis tests were conducted - the end notched flexure test (ENF) and the double cantilever beam test (DCB). Results from these tests are used in developing and calibrating the cohesive zone models (CZM) that were used to characterize composite delamination in the validation tests.

Additionally, an examination of damaged and failed specimens was performed using a SEM. The study helped in gaining an understanding of the microstructure of the composite.

2 Background

2.1 Stacked-ply validation

The use of stacked-ply coupons to compare results with virtual models of fiber-reinforced composites under quasi-static loading conditions has been shown to be a reliable method of model validation. Bruyneel et al. (Bruyneel, et al., 2014) discuss the development of a damage model formulated in SAMCEF, a finite element analysis software, in which they use stacked-ply coupons to validate their model. Using stress-strain curves, based on both longitudinal and transverse strains, they compared simulation and experimental results. The same metric was used by Ladeveze and LeDantec (Ladeveze & LeDantec, 1992) in their stacked-ply validation of a continuum-damage mechanics theory.

Open-hole tests have been used as validation tests for predicting the response of stacked-ply coupons. Achard et al. (Achard, Bouvet, Castanié, & Chirol, 2014) used open-hole tension tests for validating their method of Discrete Ply Modeling, a study in which they compared normalized stress-strain in the longitudinal direction as well as failure patterns and delamination around the hole. In similar fashion, Clay and Knoth (Clay & Knoth, 2017) used stacked-ply, open-hole compression and tension tests to evaluate composite progressive damage analysis methods. In this study, bulk stiffness and strength are used as comparison metrics between simulated and experimental data. In addition, x-ray tomography radiographs are used to evaluate damage and failure of the test coupons near the hole.

2.2 Fracture mode tests

The double cantilever beam (DCB) and end notched flexure (ENF) test are well established methods of characterizing fracture in both mode I and mode II fracture, respectively. While these tests have proven to be very useful, an understanding of their deficiencies is critical to analyzing the results of these tests.

The use of the ENF test alone for mode II fracture has a few disadvantages. Zabala et al. (Zabala, Aretxabaleta, Castillo, & Aurrekoetxea, 2016) state that the mode II strain energy release rate is typically characterized by four tests - the ENF, stabilized end notched flexure (SENF), end loaded split (ELS) and four point bend end notched flexure (4ENF). Kageyama et al. (Kageyama, Kikuchi, & Yanagisawa, 1991) describe a limitation of the ENF test in that crack growth is unstable during the test, thus the test will not produce an R-curve but will only yield an initiation value of the strain-energy release rate. In addition to unstable crack growth, Schuecker and Davidson (Schuecker & Davidson, 2001) studied the effect of friction in the ENF and 4ENF tests. The authors concluded that though friction effects were larger for the traditional ENF test, it was insignificant in both tests and the differences between the results of the ENF and 4ENF were due to other experimental factors.

O'Brien et al. (O'Brien, Johnston, & Toland, 2010) used ENF tests to characterize mode II interlaminar fracture toughness of rotorcraft material. In this study, they followed American Society for Testing and Materials (ASTM) standards to produce results for both non-precracked and precracked specimens. For their study, the authors used a polytetrafluoroethylene film at the mid-plane of a specimen to act as the source of initial delamination.

ASTM D5528 (ASTM, 2013) on the DCB test describes four methods for calculating the strain energy release rate including modified beam theory, rotation corrected modified beam theory, compliance calibration, and modified compliance calibration. Yoshihara and Satoh (Yoshihara & Satoh, 2009) described these methods and their use in correcting the crack tip deformation. In order to use the modified beam theory, it is important that the strain-energy release rate be uniform along the entire crack front. Sun and Zheng (Sun & Zheng, 1996) studied the role of the ply layup in creating a uniform strain-energy release front at the crack tip and recommended a repeated 0°-ply layup.

A study by Nandakumar (Nuggehalli Nandakumar, 2010) on rate effects on interlaminar fracture toughness included the T800/F3900 composite. This study found a mode I fracture toughness of 2.5 to 5 lb/in including a decrease with increasing displacement rate and a mode 2 fracture toughness of 9 to 20 lb/in including an increase with increasing displacement rate. The study also

found that fiber bridging had lesser effect with lower displacement rates. Tamuzs et al. (Tamuzs, Tarasovs, & Vilks, 2001) studied the effect of fiber bridging on double-cantilevered beam specimens and found that fiber bridging can have a significant impact on the later stages of the traction-separation law.

Existing studies have shown that there are multiple ways to model interlaminar layers of fiber-reinforced composites, and the use of cohesive zone elements has proven to be effective. Wasseem and Kumar (Wasseem H.S. & Kumar N.) produced one such study in which cohesive zone elements modeled the delamination zone for the DCB test. The use of the DCB and ENF tests to calibrate the parameters of cohesive zone elements has been studied and used effectively. On a commercial level, Veryst Engineering (Experimental Calibration of Cohesive Zone Models) employs the use of model calibration to get the properties of the interlaminar layer of composites from DCB and ENF tests. They use load and displacement data from experimental tests to produce the traction-separation law of these materials.

While calibration using experimental data has proven to be effective, Arrese et al. (Arrese, Boyano, De Gracia, & Mujika, 2017) developed a new procedure to get the traction-separation law. The procedure developed by the authors of this study employs an analytical approach to directly obtain strain energy release rate, displacement, and, by way of differentiation, the traction-separation law from experimental data. This approach, however, was only shown for the DCB test.

Many existing studies have found success using a bilinear model of the traction-separation law for both the DCB and ENF models. Meo and Thieulot (Meo & Thieulot, 2005) produced one such study in which they used a bilinear softening model in DYNA3D to model the cohesive elements for a double cantilevered beam specimen.

2.3 SEM imaging

To identify types and extent of damage to the fiber-reinforced material, an understanding of the formulation and types of micro damage in these materials was needed. In a study on fatigue damage mechanisms on thermoset and thermoplastic composites, Jollivet et al. (Jollivet, Peyrac, & Lefebvre, 2013) discussed the progression of damage in these materials. They explained that the first damage to occur requires low energy consumption, primarily interface and matrix failure, while higher energy damage such as fiber breakages occur later. The authors also described the development of intralaminar and interlaminar cracks.

Other studies showed SEM images of failed or damage specimens, which gave insight on what specific types of damage typically looked like using a SEM. Llorca et al. (LLorca, González,

Molina-Aldareguía, & López, 2013) produced a study on modeling composites at all scales and SEM images of damaged specimens. This study showed images of fiber interface decohesion as well as formation of matrix damage.

To produce quality SEM images of the composite material depicting the level of damage and types of failure in each specimen, other studies with SEM images were sought out to develop strategies for imaging. One such study, by Li et al. (Li, Zhao, Xu, Leung, & Wang, 2019) showed that a voltage of 20 kV produced good images of carbon fibers, among other SEM settings and methods they used.

3 General experimental test procedures

3.1 Sample preparation

Waterjet was used to cut the test coupons. Table 2 shows the waterjet specifications. The cut speed used for the validation test samples was Quality 3. Table 3 depicts the specifications of the abrasive used in the waterjet. Additionally, when necessary, the waterjet cut edges were ground using a grinding wheel matching the specifications shown in Table 4. Particle size statistics of the abrasive used on the grinding wheel are shown in Table 5. Test samples were generated with planar cut, smooth edges, and were free of any visible damage.

Table 2. Waterjet Specifications

| Specification | 8-ply Samples |
|-------------------------------|---------------|
| Approximate Thickness (in) | 0.125 |
| Abrasive Size (grit) | 80 (US Std) |
| Nozzle Diameter (in) | 0.03 |
| Minimum Nozzle Pressure (psi) | 30000 |
| Maximum Nozzle Pressure (psi) | 45000 |
| Cut Speed (in/min) | |
| Quality 1 | 135.43 |
| Quality 2 | 116.15 |
| Quality 3 | 72.87 |
| Quality 4 | 52.34 |
| Quality 5 | 40.5 |

Table 3. 80-Grit (US Std) Specifications

| Sieve Size (US Std) | Sieve Mesh Diameter (in) | % Retained |
|---------------------|--------------------------|------------|
| 8 | 0.0937 | 0 |
| 12 | 0.0661 | 0 |
| 14 | 0.0555 | 0 |
| 16 | 0.0469 | 0 |
| 20 | 0.0331 | 0 |
| 30 | 0.0234 | 0 |
| 40 | 0.0165 | 0-5 |
| 50 | 0.0117 | 10-35 |
| 60 | 0.0098 | 20-40 |
| 80 | 0.007 | 20-50 |
| 120 | 0.0049 | 0-15 |
| Pan | - | 0-3 |

Table 4. Grinding Wheel Specifications

| | |
|-----------------------------|-------------|
| Frequency of Rotation (rpm) | ~3500 |
| Abrasive Grit (grit) | 46 (US Std) |
| Tolerance (in) | ±0.005 |
| Operation | Manual |

Table 5. 46-Grit (Grinding Wheel) Specifications

| | |
|----------------------------|--------|
| Minimum Particle Size (in) | 0.0095 |
| Maximum Particle Size (in) | 0.022 |
| Average Particle Size (in) | 0.014 |

Figure 3 shows cross-sectional images of a typical cut sample captured using an optical microscope under various magnifications.

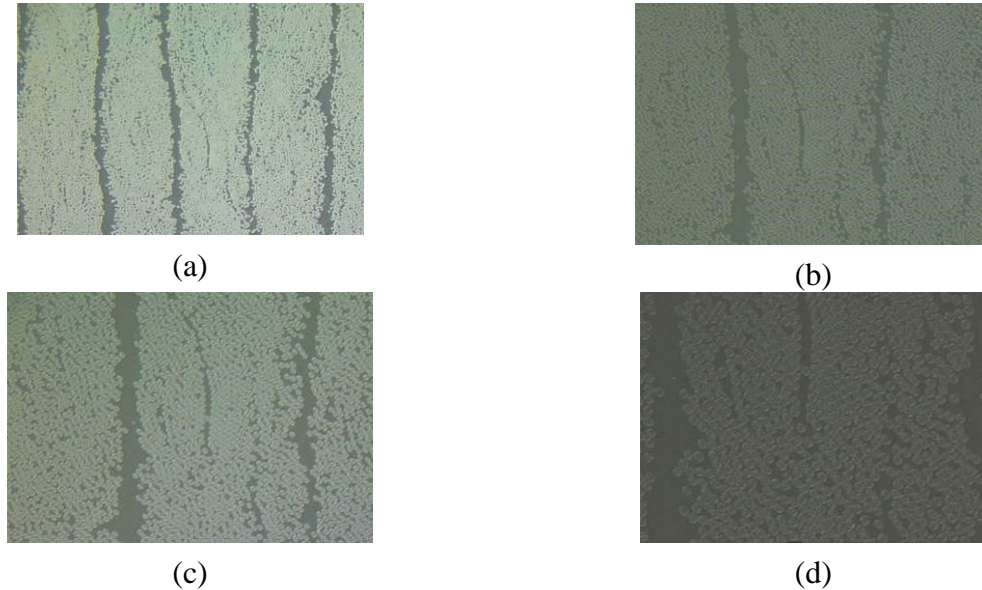


Figure 3. Optical microscopy images of finished edges (after grinding) (a) 200x, (b) 400x, (c) 500x, (d) 1000x

When required, G10 FR4 fiberglass tabs¹ were used with the sample. The fiberglass tabs acted as compliant surfaces that prevented specimens from crushing when placed in the test frame hydraulic grips. The tabs were bonded to the specified specimen surfaces using a two-part epoxy adhesive.

3M DP460 Scotch Weld toughened two-part epoxy² was used to bond fiberglass tabs to the specimens. In an earlier study (Schmidt, 2016); the guidelines set forth in ASTM D3528-96 were used to carry out the adhesive strength study using a double lap shear test. This study proved the DP460 epoxy had an adequate bond strength with G10 fiberglass.

All stacked-ply specimens were prepared in the same manner unless otherwise noted. The following list outlines the steps taken to prepare the specimens for testing.

1. The regions on a typical specimen where fiberglass tabs were bonded, and the surfaces of the fiberglass tabs being bonded to the specimen were lightly sanded using 120 grit

¹ G10, FR4 Laminate Sheets 36"x 48", Epoxyglas™; NEMA Grade FR4, Mil-I-24768/27, <http://www.acculam.com/>
²<http://multimedia.3m.com/mws/media/661220/3mtm-scotch-weld-tm-epoxy-adhesive-dp460-ns-and-off-white.pdf>

sandpaper. Sanding the surfaces ensured a complete bond between the specimen and the tabs.

2. The sanded surfaces that were cleaned using cotton swabs soaked with isopropyl alcohol. The surfaces were air dried until there was no visible moisture on the bonding surfaces.
3. The 3M epoxy was mixed in accordance to the manufacturer's recommendation. A thin layer of the mixed epoxy was applied to the prepared surface of the tabs using a wooden applicator.
4. The tabs were placed on the specimen and positioned until the surfaces of the specimen and the tabs were in complete contact and aligned properly in the desired region.
5. The specimens cured at room temperature and atmospheric pressure for 24 hours.
6. Next, the gage region of the specimen was painted and speckled. Speckling of the specimen involved first spraying the surface of the specimen with a layer of white paint with a flat finish. Paint was sprayed onto the surface until the specimen could no longer be seen. The paint dried completely at room temperature.
7. Black paint with a flat finish was sprayed onto the dry white paint. The black paint was sprayed in a manner that resulted in random array of black dots being deposited on the white area of the specimen.
8. After painting the specimens, they finished curing for another 24 hours as recommended by the manufacturer. A close up of a typical speckled surface is shown in Figure 4.



Figure 4. Close up of a typical speckled surface

3.2 Test machines, fixtures, equipment, and software

All stacked-ply validation experiments were performed using the same test frame and a similar camera system. Post processing of the experimental images was performed using the same software as described next.

Test Frame: The experimental procedures for the stacked-ply tests were performed using an MTS 810 universal testing frame (Figure 5(a)). Flat tension specimens were held in the frame with MTS 647.10A hydraulic grips (Figure 5(b)). The hydraulic grips were aligned by clamping a rigid, flat steel plate and allowing the heads to rotate freely into position. After aligning the hydraulic grips, the specimen was placed into the test frame. The specimen was gripped up to the end of the fiberglass tabs. Compression specimens were tested using a Wyoming Test Fixtures combined loading compression fixture (CLC) as shown in Figure 5(c) and Figure 5(d). The CLC fixture transfers load into the compression specimens through both shear load transfer and end load transfer, thus decreasing the need for large clamping forces.

Force data was gathered using an MTS 661.21A-03 load cell. All experiments were performed under displacement control conditions. The displacement rate refers to the rate of displacement of the test frame actuator. The MTS system controller set the displacement rate.

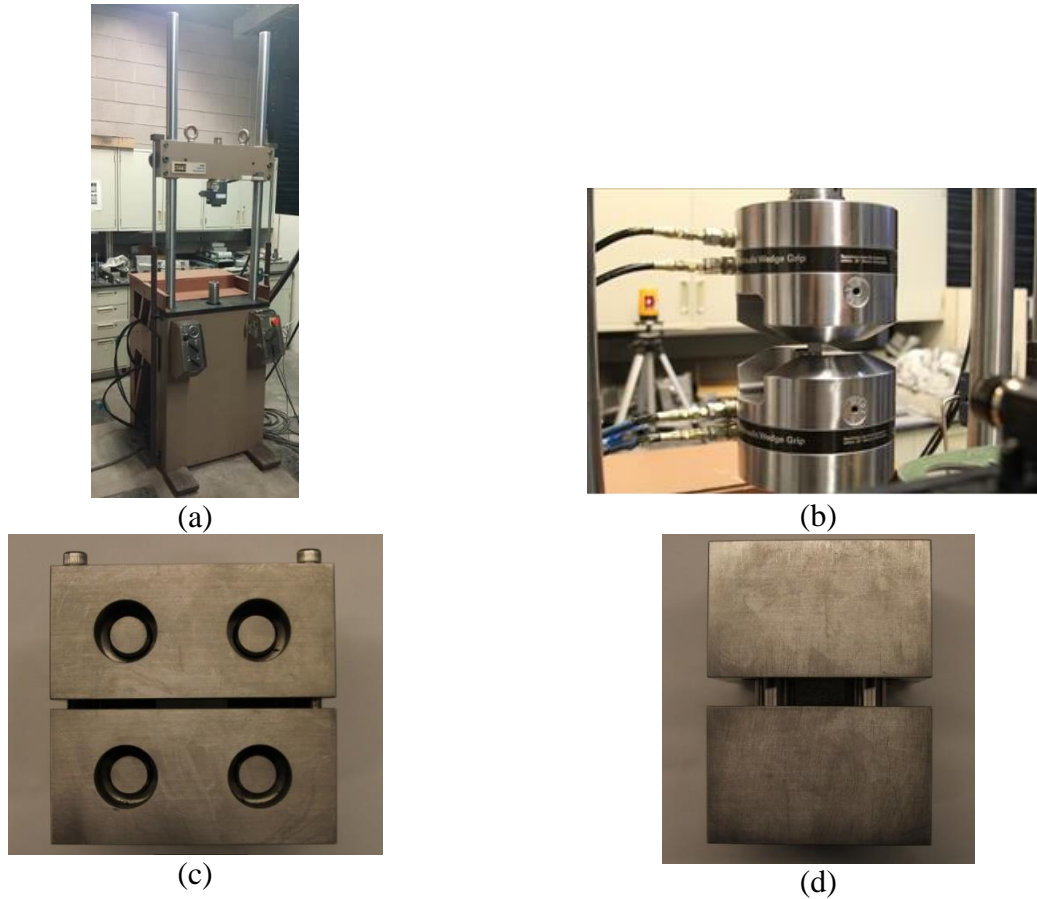


Figure 5. Experimental equipment (a) Test frame, (b) Hydraulic grips, (c) CLC compression fixture top, and (d) CLC fixture front

Digital Image Correlation (DIC) Equipment: Two Point Grey Grasshopper 3³ cameras were used to capture images of the specimen throughout the duration of the experiment as shown in Figure 6(a). LED lamps were used to illuminate the specimen during the experiment. The cameras and lights were fixed to the same frame (Figure 6(b)). The frame was leveled using a bubble level in order to ensure the field of view of the cameras was both horizontal and vertical respectively. A high-speed camera was used to capture the specimen state at the moment of failure (Figure 6(a)). Unless otherwise noted, images were captured at five-second intervals throughout the experiment using Vic-Snap 8 (Correlated Solutions).

³ <https://www.ptgrey.com/grasshopper3-gige-vision-cameras>



(a)



(b)

Figure 6. (a) Two DIC cameras and high-speed camera (b) LED lighting fixture

Post Processing: The images captured during the experiment were processed to obtain full strain field using Vic-3D v7 (Correlated Solutions) software system. The Lagrangian definition of strain was chosen to perform the analysis. Vic-3D software was used to smooth the strain data using a decay filter algorithm. The initial processing analyzed the entire speckled region of the specimen. After the analysis and smoothing were completed, a smaller region with constant strain was taken as the representative strain induced in the specimen during the experiment. The region of interest was typically chosen so that the strain field was as uniform in that region as possible. Typically, this region is away from the edges of the specimen and away from areas of strain concentrations that may have been present where the specimens were gripped. In this report, this area or region (from which the strain values are obtained and reported) is referred to as the *strain gage section* (SGS). Sample images showing various SGS are shown in Figure 7.

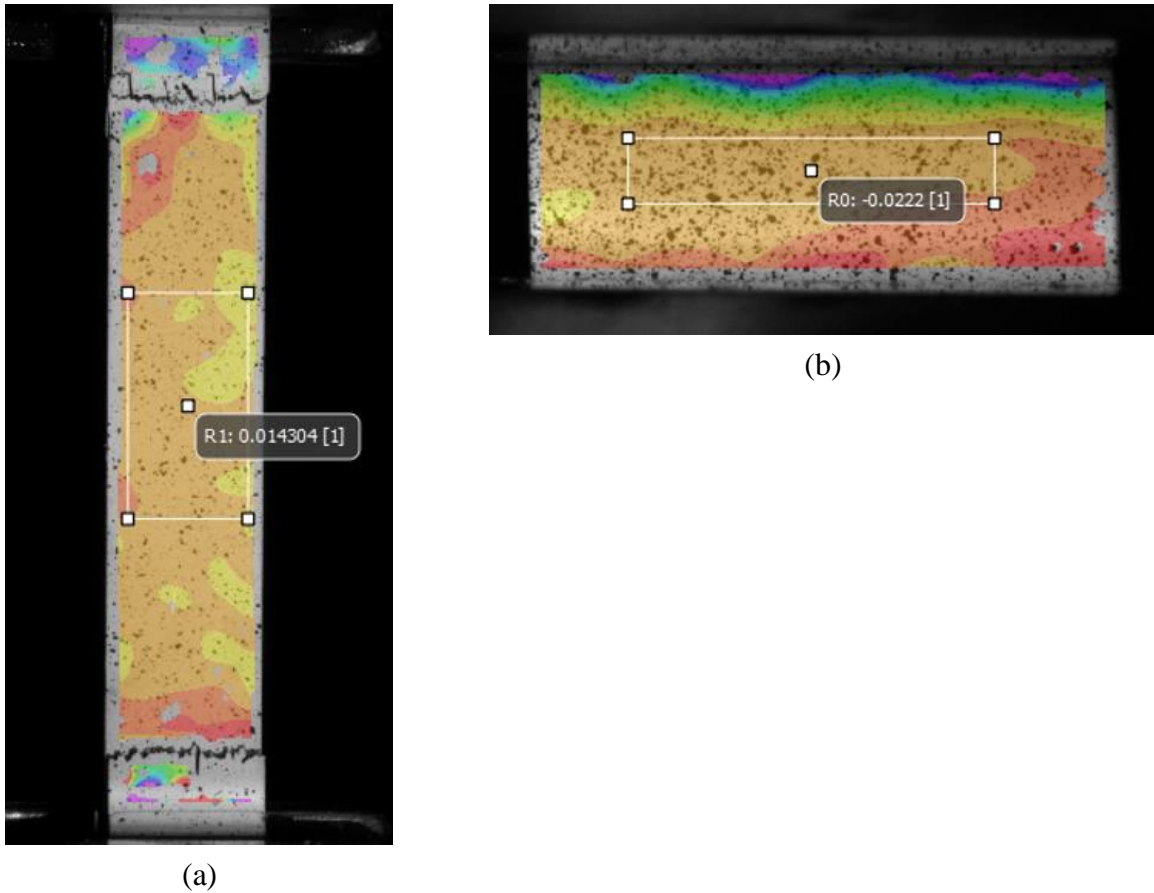


Figure 7. Typical SGS (a) Tension specimens (b) Compression specimens

The tension tests performed used a dual DIC setup that allowed capture of images on two faces of the specimen. Two sets of two Point Grey Grasshopper 3 cameras and LED lights were positioned on either side of the testing frame and directed at the specimen. The resulting images from one side were labeled as System 1 (*Sys1*) and those from the other side were labeled as System 2 (*Sys2*). The goal of this dual system was to measure the strains on two opposite faces of the test specimen to identify the extent of variability between the strains of the two sides. This variability indicated the extent to which the samples may have been warped during the manufacturing process or misaligned in the test fixture. Post processing of *Sys1* and *Sys2* data was completed independently. Figure 8 shows the dual DIC setup.

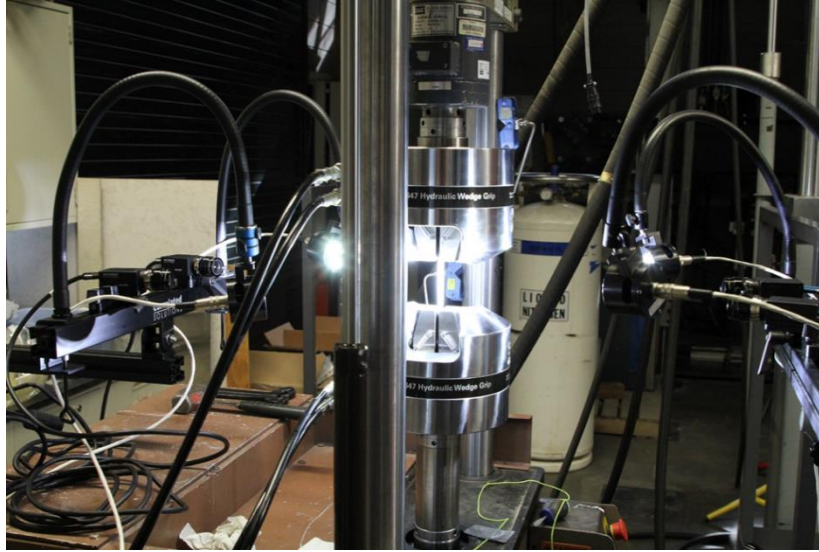


Figure 8. Dual DIC systems setup

Measurement Instruments: Several instruments were used to obtain specimen dimensions, specimen mass, and optical microscope images. Specimen dimensions were measured using a Pittsburgh 4” Digital Caliper⁴. The caliper has a resolution of 0.0005 in. All optical microscopy images were captured using an Olympus MX50 optical microscope⁵.

3.3 Typical test procedure

The procedure for conducting experiments are the same for each specimen unless otherwise noted. For all experiments, prior to loading the specimen, the DIC system was calibrated using Vic 3D v7 software system. Calibration was done only when the cameras were moved, or when the use of new fixtures would cause the plane of the specimen to be different from when the cameras were calibrated. All experimental tests were conducted under displacement-controlled conditions.

3.4 Post-processing of test data

Force data was obtained as a function of time from the MTS controller, and strain data was obtained as a function of time from DIC analysis. The stress in the specimen was taken as the average stress across the respective cross section of the specimen. For tension and compression specimens, the cross section perpendicular to the direction of loading was used to calculate the cross-sectional area. The average stress was calculated using following equation 1.

⁴ <https://www.harborfreight.com/4-inch-digital-caliper-47256.html>

⁵ <https://www.olympus-ims.com/en/service-and-support/obsolete-products/>

$$\sigma = \frac{F}{A}$$

1

F is the normal force reported by the load cell at the current time-step and A is the initial cross-sectional area. The strain reported from Vic 3D v7 in the region of interest was used in conjunction with the calculated stress to generate an engineering stress-strain curve for any given specimen.

Post-processing of test data was handled differently for the stress concentration experiments. The purpose of these tests was primarily in evaluating the ability of MAT213 to predict strain concentrations. For these experiments, strain vs. time plots were used as part of the validation process with these plots being constructed for several regions within the gage area. An example of the areas where strain was measured and analyzed is shown in Figure 9.

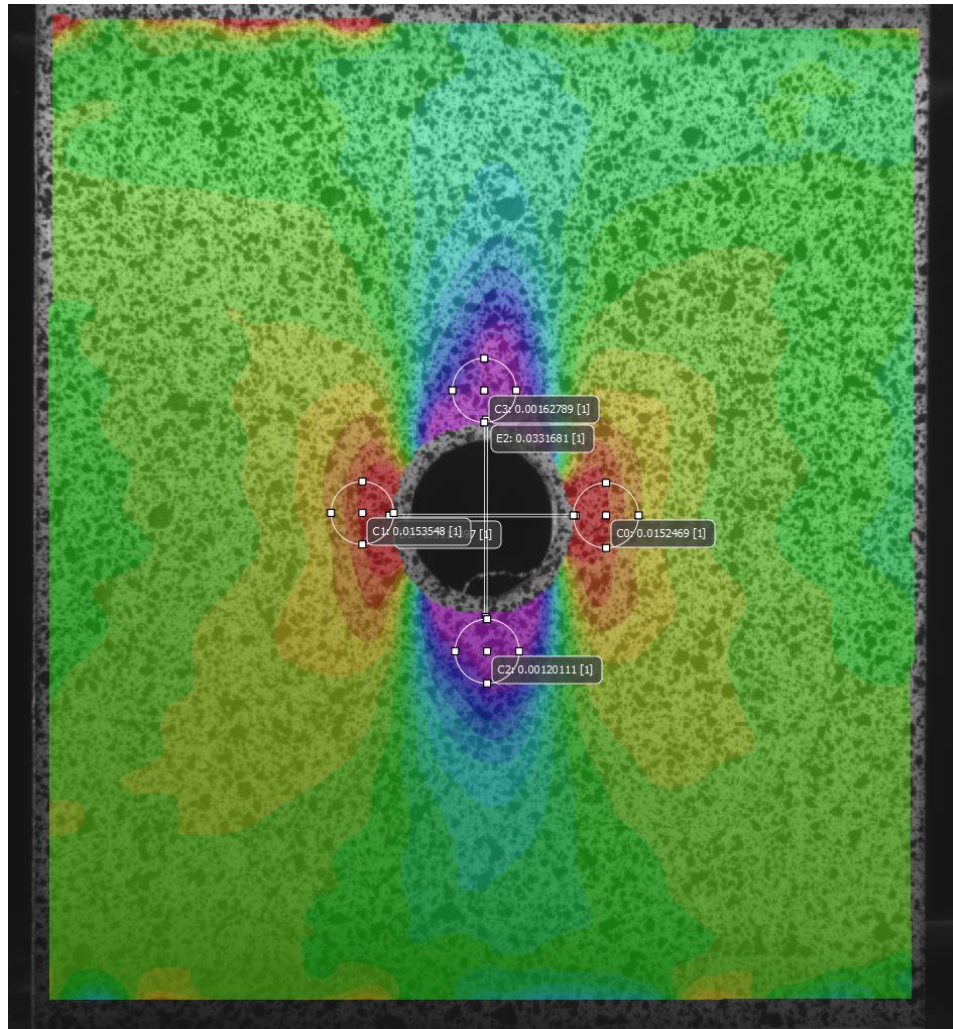


Figure 9. Strain measurement areas for stress concentration tests

There were three areas where SGSs were used to capture strain data - directly to the left and right of the hole, above the hole (top), and below the hole (bottom). Strain data from the left and right of the hole is always averaged together and represented by the abbreviation RL. The area above the hole is synonymous with “top” in this report and is abbreviated by *T*. The area below the hole is synonymous with “bottom” in this report and is abbreviated by *Bot*. Data from the right and left areas was averaged because of symmetry along the vertical axis of the test for the geometry and loading condition. The top and bottom areas were not averaged because the loading was not symmetric about the horizontal axis as shown in Figure 9. In the test frame, the top grip was fixed while the bottom fixture was subjected to a displacement-controlled condition.

In addition to the stress-strain curve, several parameters were obtained from the stress-strain curves of each individual specimen to determine how consistent the data is. Table 6 describes each parameter and how they were obtained.

Table 6. Descriptions of the parameters used in this report

| Parameter | Definition | Method |
|---------------------|--|--|
| Loading rate | Constant rate at which the actuator on the test frame is displaced. | Chosen by the experimenter as a fixed parameter at the beginning of the procedure. The rate is prescribed as a displacement over a certain period. |
| Strain rate | The rate at which strain is induced in the specimen during a given experiment. | The strain measure of interest is plotted as a function of time and the average strain rate during the experiment is obtained by performing a linear regression. The slope of the resulting best-fit line is taken as the average strain rate. |
| Modulus, E | The slope of the initial linear region of the true stress-strain curve. | The analyst determines the region in the initial portion of the curve and performs a linear regression. The slope of the resulting best-fit line is taken as the modulus. |
| Peak stress | Maximum stress achieved during a given experiment. | Selected from stress data obtained through scaling the force data reported by the load cell. |
| Ultimate strain | Strain measured at peak stress. | Selected as the largest strain when the specimen exhibits brittle failure with no post-peak strength. |
| Failure strain | Strain measured when the specimen fails. | Selected as the strain when there is a large drop in stress and the specimen no longer loads back up to that peak stress point. Typically, this occurs when the test is terminated and is used when specimen does not exhibit brittle failure. |
| Transverse strain | Strain induced in the specimen perpendicular to the direction of loading in tension and compression tests. | Obtained through DIC measurements. |
| Longitudinal strain | Strain induced in the specimen parallel to the direction of loading in tension and compression tests. | Obtained through DIC measurements. |

Throughout this report, “EXP” refers to experimental tests and “SIM” refers to LS-DYNA simulations.

4 Stacked-ply experimental test details and results

4.1 Overview

This section discusses details of each test. Experimental procedures used applicable ASTM standards. Deviations from the standards are noted in the report.

4.2 Stacked-ply tension test

Specimen Geometry: ASTM D3039 standard (ASTM, 2017) is applicable for this test. Figure 10 shows the specimen geometry and layout. Shaded regions indicate where fiberglass tabs were bonded to the specimen.

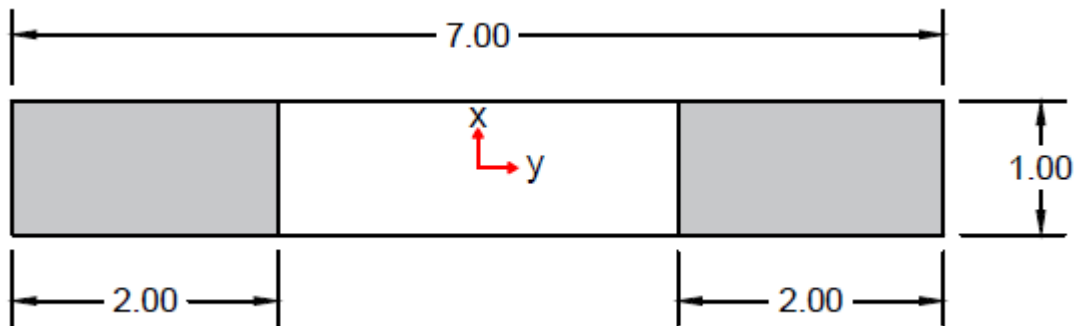


Figure 10. Typical specimen geometry and layout (all dimensions in inches)

Table 7 lists the average specimen dimensions in the gage section.

Table 7. Tension test specimen dimensions

| Replicate ID | Width (in) | Thickness (in) | Cross Sectional Area (in ²) |
|------------------------------|------------|----------------|---|
| V-T-4 | 0.9990 | 0.0660 | 0.0659 |
| V-T-5 | 0.9987 | 0.0633 | 0.0632 |
| V-T-6 | 1.0022 | 0.0632 | 0.0634 |
| Average | 1.0000 | 0.0642 | 0.0642 |
| Standard Deviation | 0.0019 | 0.0016 | 0.0015 |
| Coefficient of Variation (%) | 0.19 | 2.47 | 2.39 |

The stroke rate of the MTS machine for this test was 0.02 in/min. The DIC image capture rate varied between one frame per five seconds and one frame per second.

Specimen Photographs: Figure 11 shows the specimen photographs before the tests. Post-test images include images of the gage area in the XY plane, zoomed in images of this plane, and images of the through thickness. Figure 12 shows the specimens after testing.

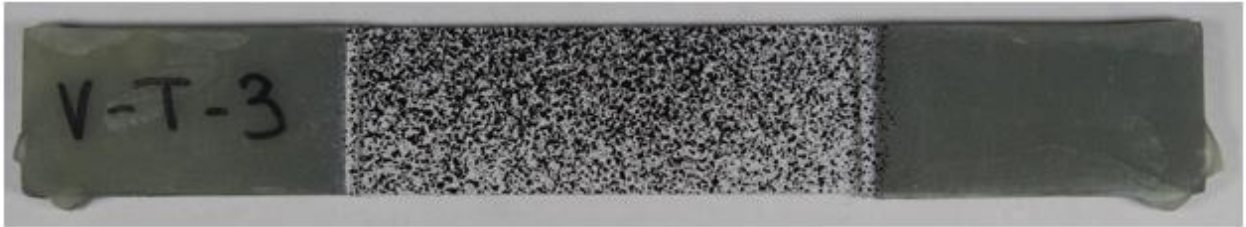
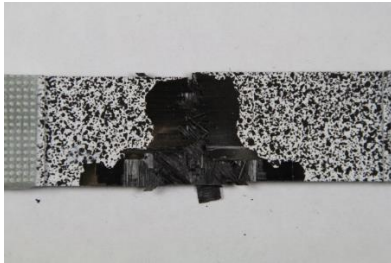


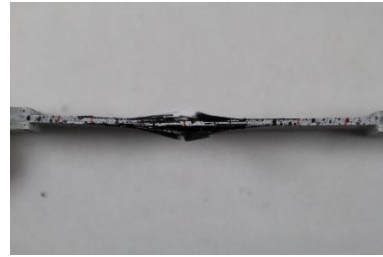
Figure 11. Example image of tension specimen prior to testing



(a)



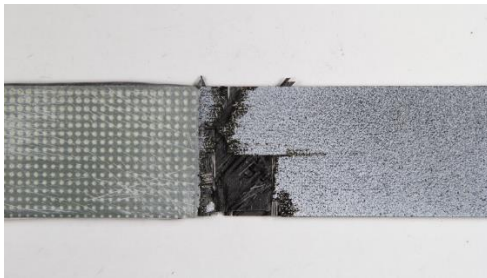
(b)



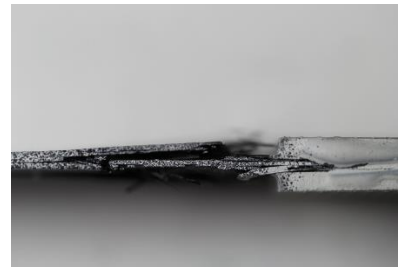
(c)



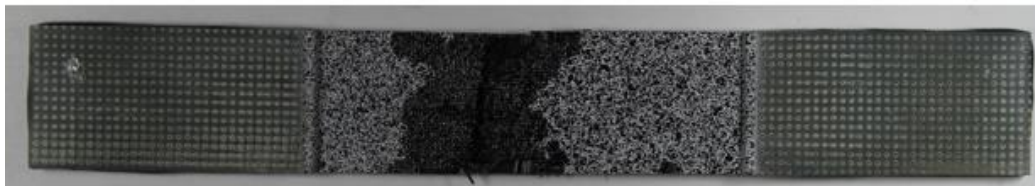
(d)



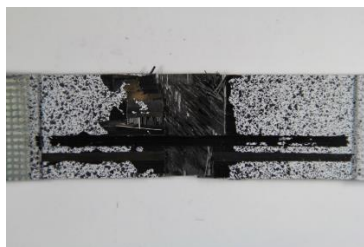
(e)



(f)



(g)



(h)



(i)

Figure 12. Tension specimens after testing (a)(b)(c) V-T-4, (d)(e)(f) V-T-5, (g)(h)(i) V-T-6

Observations during the test and examination of the tested specimens suggested that the 0°-plies failed first. Once these plies failed, the redistribution of stress caused the other plies to fail subsequently.

Test Results: Table 8 shows the summary of the test results.

Table 8. Summary of tension test results

| Replicate ID | Loading Rate (in/min) | Strain Rate $\left(\frac{1}{s}\right)$ | E_{yy} (psi) | Ultimate Strain | Peak Stress (psi) |
|------------------------------|-----------------------|--|----------------|-----------------|-------------------|
| V-T-4 | 0.02 | 7.67E-05 | 6923262 | 0.0169 | 117015 |
| V-T-5 | 0.02 | 7.96E-05 | 7437892 | 0.0164 | 119019 |
| V-T-6 | 0.02 | 8.23E-05 | 7100700 | 0.0178 | 125852 |
| Average | - | 7.95E-05 | 7153951 | 1.7039E-02 | 120628 |
| Standard Deviation | - | 2.80E-06 | 261415 | 7.0138E-04 | 4633 |
| Coefficient of Variation (%) | - | 3.52 | 3.65 | 4.12 | 3.84 |

Figure 13 shows the response was mostly linear since the 0° plies, oriented along the axis of loading, dominate the response of the composite laminate.

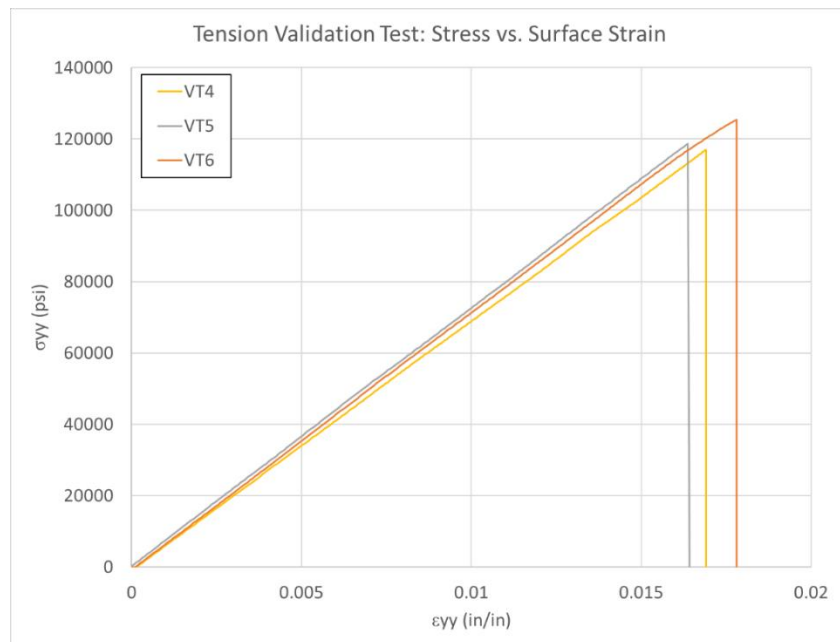


Figure 13. Tension stress-strain curves

4.3 Stacked-ply compression test

Specimen Geometry: ASTM D3410 and D6641 (ASTM, 2016) (ASTM, 2016) standards are applicable for this test. The specimen geometry and layout are shown in Figure 14. Shaded regions indicate where the specimen was gripped in the fixture.

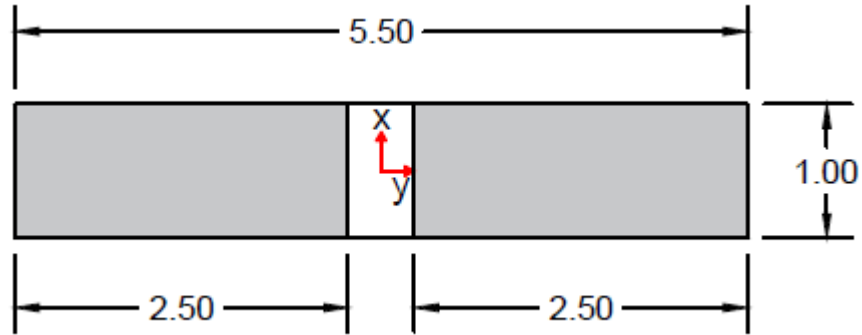


Figure 14. Typical specimen geometry and layout (all dimensions in inches)

Table 9 shows the average specimen dimensions in the gage section for the tested replicates.

Table 9. Compression test specimen dimensions

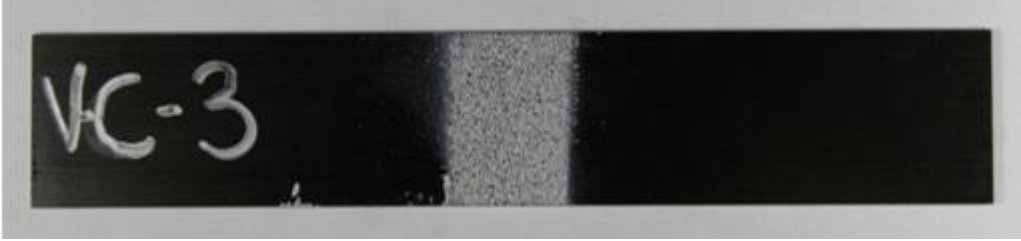
| Replicate ID | Width (in) | Thickness (in) | Cross Sectional Area (in ²) |
|------------------------------|------------|----------------|---|
| V-C-2 | 0.9982 | 0.0632 | 0.0631 |
| V-C-3 | 0.9988 | 0.0624 | 0.0623 |
| V-C-4 | 0.9984 | 0.0616 | 0.0615 |
| Average | 0.9985 | 0.0624 | 0.0623 |
| Standard Deviation | 0.0003 | 0.0008 | 0.0008 |
| Coefficient of Variation (%) | 0.03 | 1.28 | 1.27 |

The stroke rate of the MTS machine for this test was 0.01 in/min. The DIC image capture rate was one frame per five seconds.

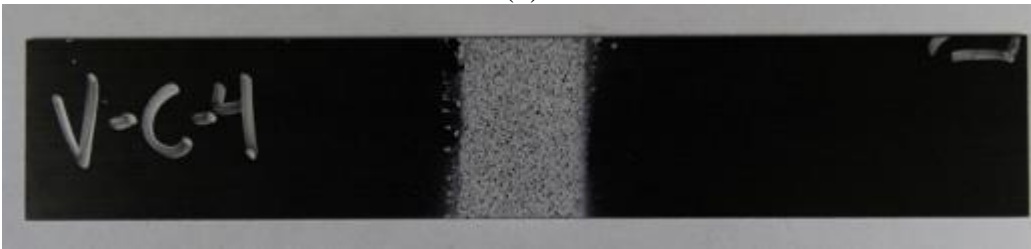
Specimen Photographs: The specimen photographs before the tests are shown in Figure 15. Post-test images include images of the gage area in the XY plane and images of the through thickness state of the specimens. Figure 16 shows the specimens after testing.



(a)

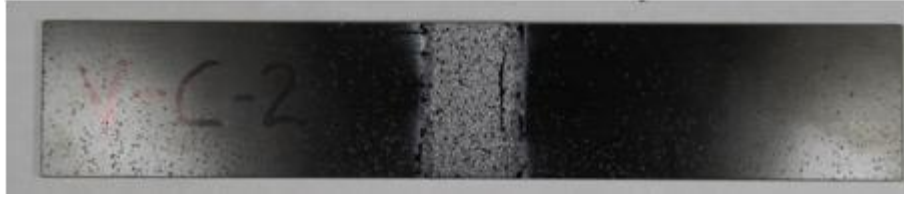


(b)

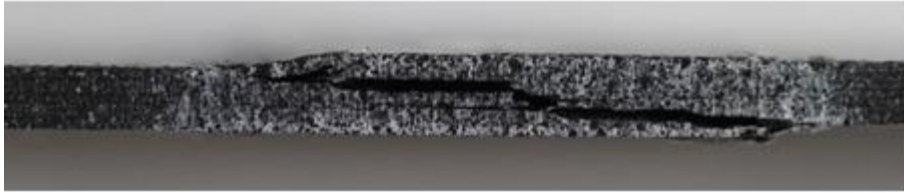


(c)

Figure 15. Compression specimens prior to testing (a) V-C-2, (b) V-C-3, (c) V-C-4



(a)



(b)



(c)



(d)

Figure 16. Compression specimens after testing (a) V-C-2 XY surface (b) V-C-2 through thickness (c) V-C-3 XY surface (d) V-C-3 through thickness

The failure pattern of Figure 16(d) suggested that outer 0^0 and 90^0 -plies failed first, followed by out-of-plane buckling.

Test Results: The summary of the results from the tests is shown in Table 10.

Table 10. Summary of compression test results

| Replicate ID | Loading Rate (in/min) | Strain Rate $\left(\frac{1}{s}\right)$ | E_{yy} (psi) | Ultimate Strain | Peak Stress (psi) |
|--------------|-----------------------|--|----------------|-----------------|-------------------|
| V-C-2 | 0.01 | 4.02E-05 | 6318793 | -0.0064 | -40609 |
| V-C-3 | 0.01 | 3.17E-05 | 6076000 | -0.0062 | -40840 |
| V-C-4 | 0.01 | 3.83E-05 | 6084202 | -0.0060 | -39085 |

| Replicate ID | Loading Rate (in/min) | Strain Rate $\left(\frac{1}{s}\right)$ | E_{yy} (psi) | Ultimate Strain | Peak Stress (psi) |
|------------------------------|-----------------------|--|----------------|-----------------|-------------------|
| Average | - | 3.67E-05 | 6159665 | -0.0062 | -40178 |
| Standard Deviation | - | 4.46E-06 | 137870 | 0.0002 | 954 |
| Coefficient of Variation (%) | - | 12.15 | 2.24 | 2.89 | 2.37 |

Figure 17 shows the individual stress-strain curves for each of the specimens that produced reliable results. The strain was the longitudinal strain measured on the surface of the specimen. The stress was the overall laminate stress (area of all 8 plies).

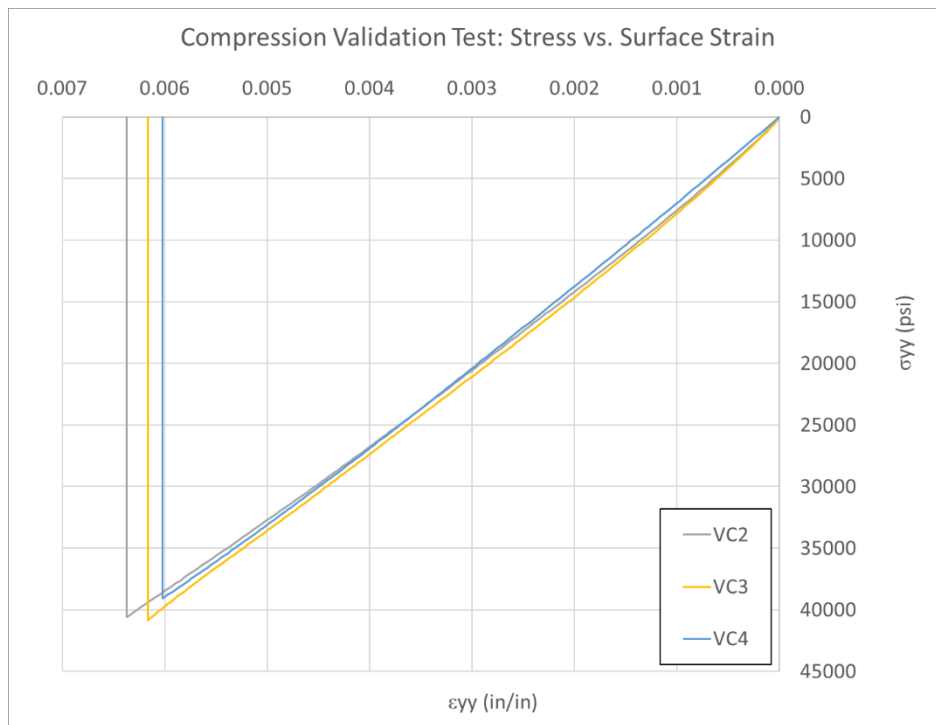


Figure 17. Compression stress-strain curves

4.4 Stacked-ply tension stress concentration test

Specimen Geometry: ASTM D3039 and D5766 standards (ASTM, 2017) (ASTM, 2011) are applicable for this test. The specimen geometry and layout are shown in Figure 18. Shaded regions indicate the location of fiberglass tabs bonded to the specimen.

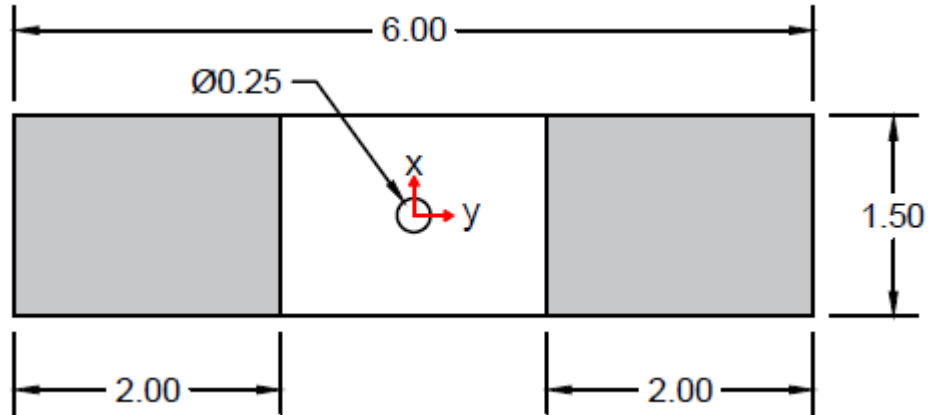


Figure 18. Typical specimen geometry and layout (all dimensions in inches)

Table 11 shows the average specimen dimensions in the gage section for the tested replicates.

Table 11. Tension stress concentration test specimen dimensions

| Replicate ID | Width (in) | Thickness (in) | Cross Sectional Area (in ²) | Hole Diameter (in) |
|------------------------------|------------|----------------|---|--------------------|
| V-TH-2 | 1.5027 | 0.0649 | 0.0975 | - |
| V-TH-3 | 1.4981 | 0.0620 | 0.0929 | - |
| V-TH-4 | 1.4980 | 0.0623 | 0.0933 | - |
| Average | 1.4996 | 0.0631 | 0.0946 | 0.25 |
| Standard Deviation | 0.0027 | 0.0016 | 0.0025 | - |
| Coefficient of Variation (%) | 0.18 | 2.53 | 2.69 | - |

The stroke rate of the MTS machine for this test was 0.01 in/min. The DIC image capture rate was one frame per five seconds.

Specimen Photographs: The specimen photographs before the tests are shown in Figure 193. Post-test images include images of the gage area in the XY plane, zoomed in images of this plane, and images of the through thickness state of the specimens. Figure 20 shows the specimens after testing.



(a)



(b)



(c)

Figure 19. Tension specimens prior to testing (a) V-TH-2, (b) V-TH-3, (c) V-TH-4

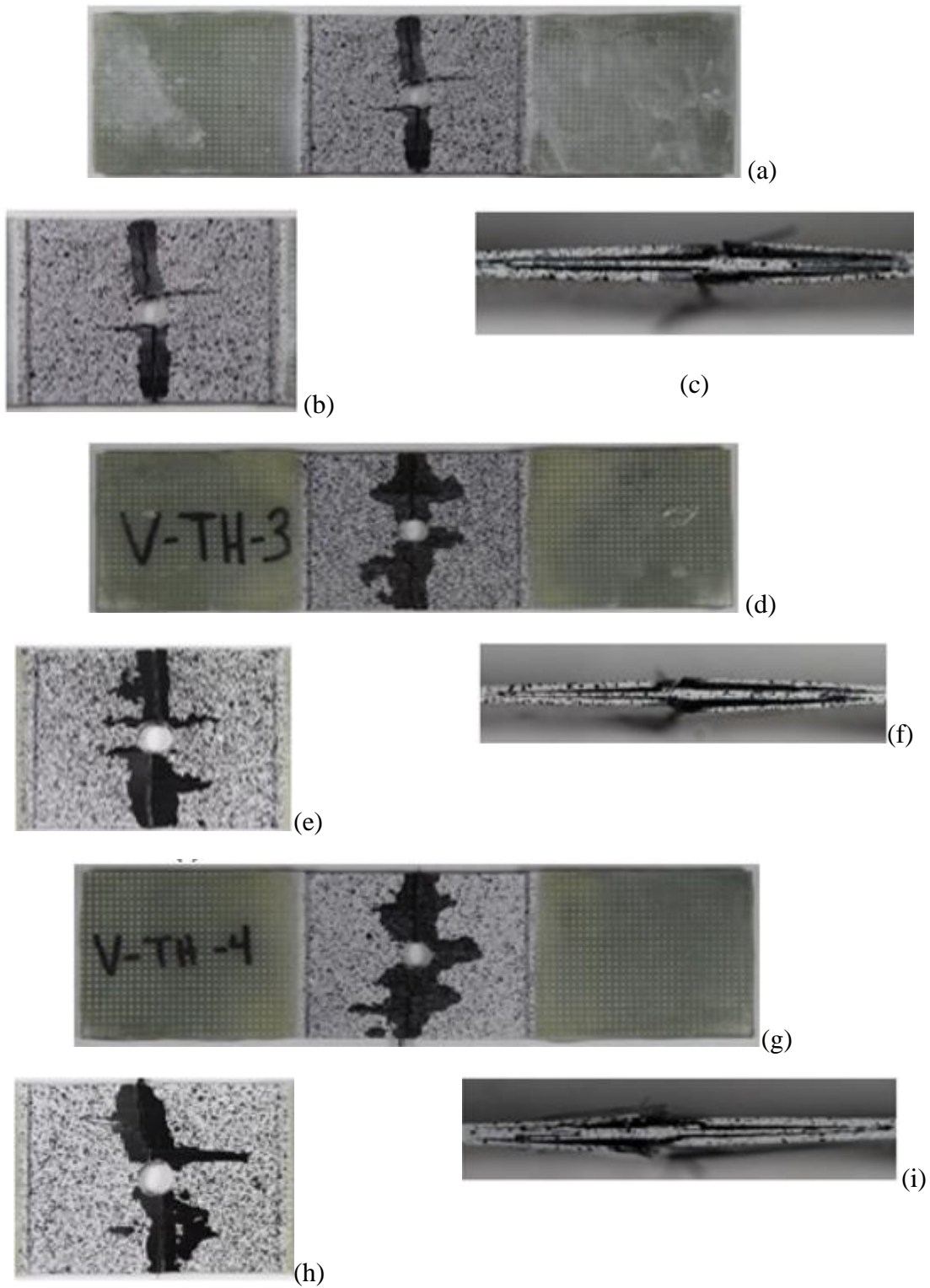


Figure 20. Tension stress concentration specimens after testing (a)(b)(c) V-TH-2, (d)(e)(f) V-TH-3, (g)(h)(i) V-TH-4

Test Results: Table 12 shows the summary of the test results.

Table 12. Summary of tension stress concentration test results

| Replicate ID | Loading Rate (in/min) | Strain Rate ϵ_{yy} (RL of Hole) (1/s) | Strain Rate ϵ_{xx} Magnitude (T of Hole) (1/s) | Maximum ϵ_{yy} (RL of Hole) | Maximum ϵ_{xx} (T of Hole) |
|------------------------------|-----------------------|--|---|--------------------------------------|-------------------------------------|
| V-TH-2 | 0.01 | 5.60E-05 | 1.26E-05 | 1.60E-02 | -4.55E-03 |
| V-TH-3 | 0.01 | 5.42E-05 | 1.29E-05 | 1.51E-02 | -4.05E-03 |
| V-TH-4 | 0.01 | 5.73E-05 | 1.29E-05 | 1.62E-02 | -4.52E-03 |
| Average | - | 5.58E-05 | 1.28E-05 | 1.58E-02 | -4.37E-03 |
| Standard Deviation | - | 1.56E-06 | 1.73E-07 | 5.86E-04 | 2.80E-04 |
| Coefficient of Variation (%) | - | 2.79 | 1.35 | 3.72 | 6.41 |

Strain data in the x and y directions were obtained for areas to right and left of the hole as well as above and below the hole. In these areas, the x and y strains matched closely with the principal strains.

The average strain within the gage area in the y direction for the areas to the left and right of the hole is shown in Figure 21.

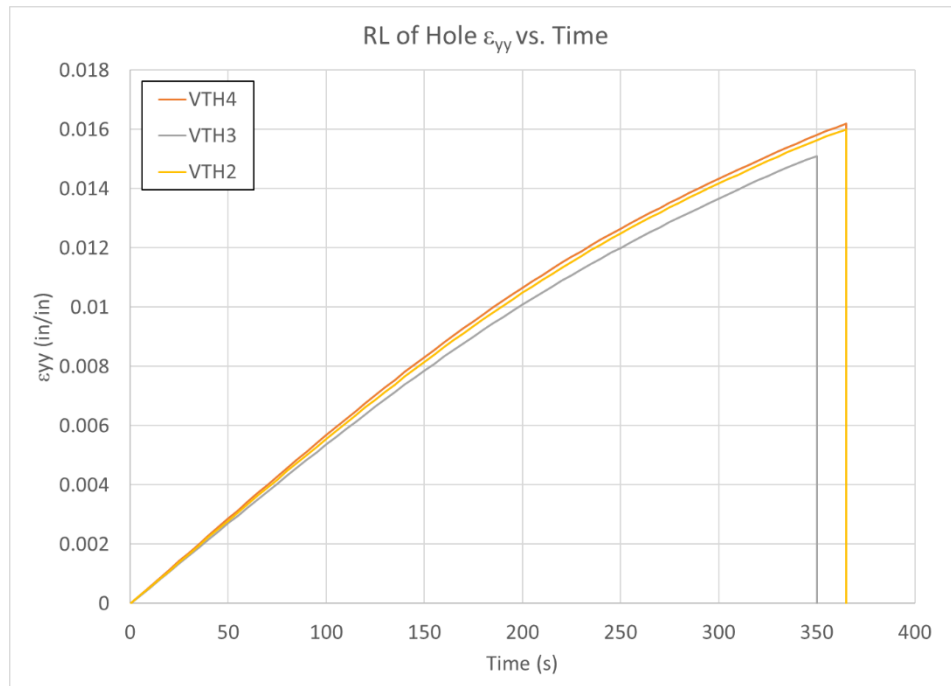


Figure 21. Tension stress concentration RL of hole ϵ_{yy} vs. time

The x strain for the area above the hole is shown in Figure 22 and for the area below the hole in Figure 23.

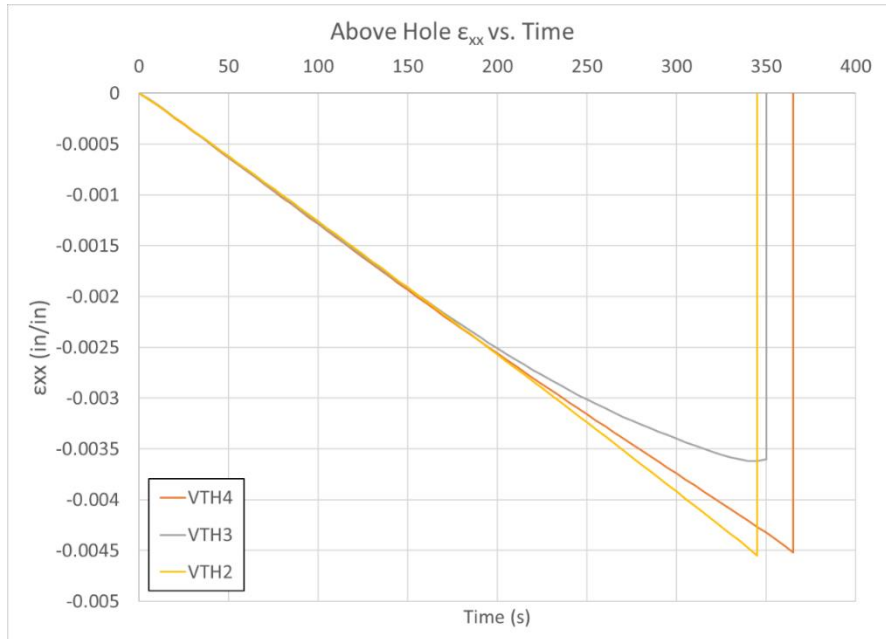


Figure 22. Tension stress concentration: above hole ϵ_{xx} vs. time

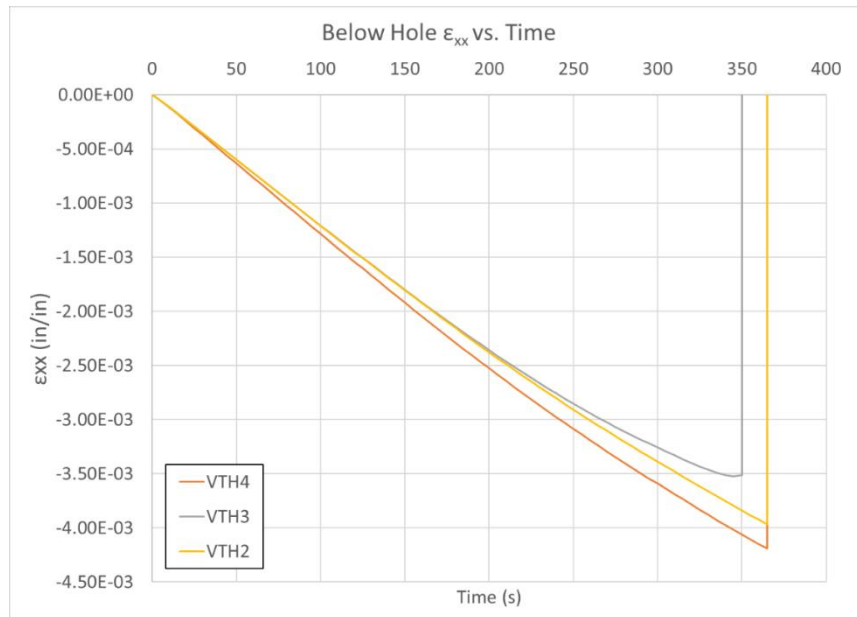


Figure 23. Tension stress concentration: below hole ϵ_{xx} vs. time

4.5 Stacked-ply compression stress concentration test

Specimen Geometry: ASTM D6641 and D6484 (ASTM, 2016) (ASTM, 2014) standards were applicable for this test. The specimen geometry and layout are shown in Figure 24. Shaded regions indicate where the fixture gripped the specimen and applied loading through shear and compression at the ends.

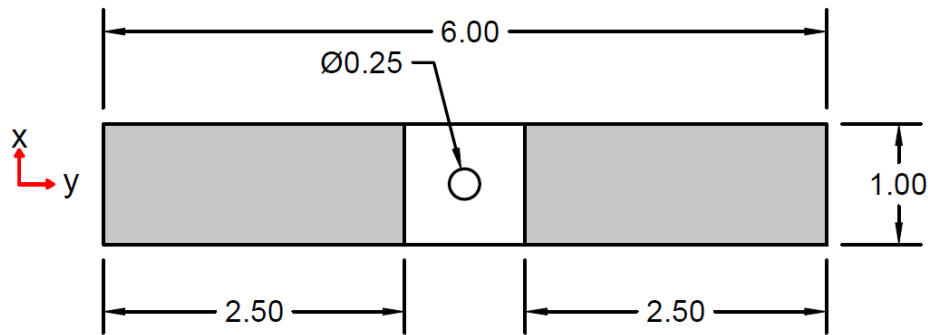


Figure 24. Typical specimen geometry and layout (all dimensions in inches)

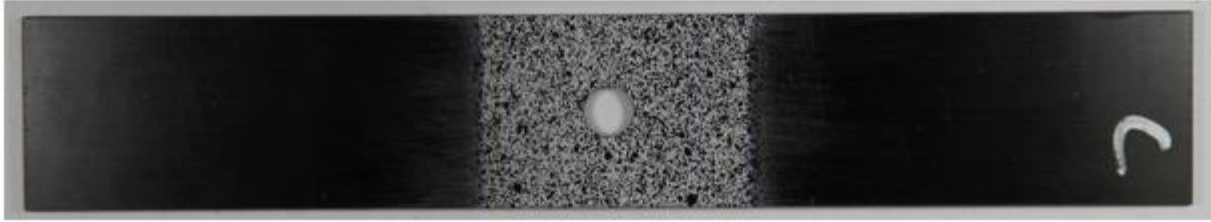
Three replicates were tested with the stated geometry. Table 13 shows the average specimen dimensions in the gage section.

Table 13. Compression stress concentration test specimen dimensions

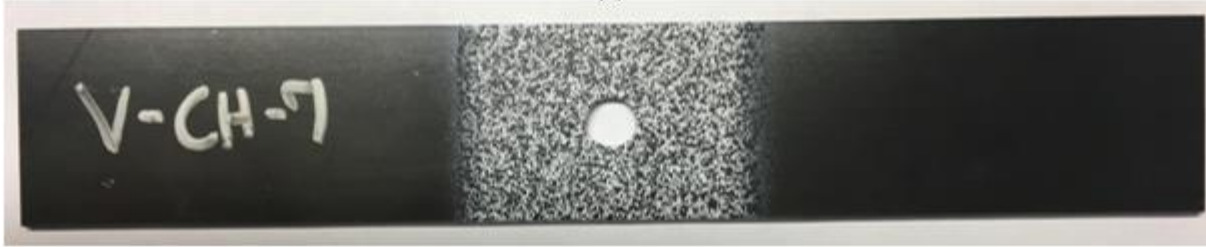
| Replicate ID | Width (in) | Thickness (in) | Cross Sectional Area (in ²) | Hole Diameter (in) |
|------------------------------|------------|----------------|---|--------------------|
| V-CH-5 | 0.9990 | 0.0599 | 0.0598 | - |
| V-CH-7 | 1.0011 | 0.0624 | 0.0624 | - |
| V-CH-8 | 1.0013 | 0.0634 | 0.0634 | - |
| Average | 1.0005 | 0.0619 | 0.0619 | 0.25 |
| Standard Deviation | 0.0013 | 0.0018 | 0.0019 | - |
| Coefficient of Variation (%) | 0.13 | 2.91 | 3.04 | - |

The stroke rate of the MTS machine for this test was 0.01 in/min. The DIC image capture rate was one frame per second.

Specimen Photographs: The specimen photographs before the tests are shown in Figure 25. Post-test images include images of the gage area in the XY plane, zoomed in images of this plane, and images of the through thickness. Figure 26 shows the specimens after testing.



(a)



(b)



(c)

Figure 25. Compression specimens prior to testing (a) V-CH-5, (b) V-CH-7, (c) V-CH-8

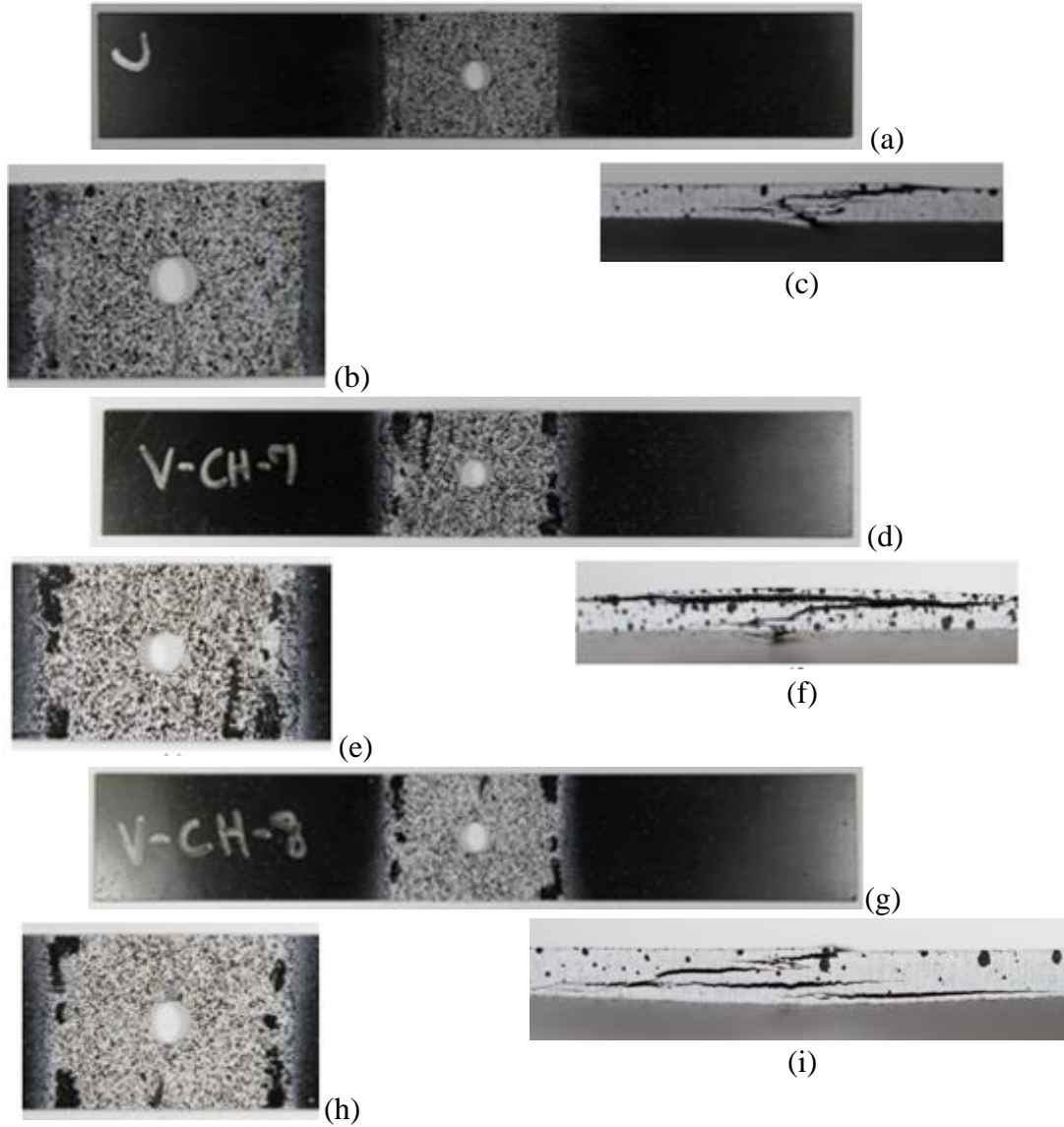


Figure 26. Compression Stress Concentration specimens after testing (a)(b)(c) V-CH-5, (d)(e)(f) V-CH-7, (g)(h)(i) V-CH-8

Test Results: Table 14 shows the summary of the test results.

Table 14. Summary of compression stress concentration test results

| Replicate ID | Loading Rate (in/min) | Strain Rate ϵ_{yy} magnitude (RL of Hole) (1/s) | Strain Rate ϵ_{xx} (T of Hole) (1/s) | Maximum ϵ_{yy} (RL of Hole) | Maximum ϵ_{xx} (T of Hole) |
|------------------------------|-----------------------|--|---|--------------------------------------|-------------------------------------|
| V-CH-5 | 0.01 | 5.27E-05 | 1.16E-05 | -9.85E-03 | 2.11E-03 |
| V-CH-7 | 0.01 | 5.14E-05 | 1.18E-05 | -1.00E-02 | 2.19E-03 |
| V-CH-8 | 0.01 | 5.26E-05 | 1.12E-05 | -7.68E-03 | 1.99E-03 |
| Average | - | 5.22E-05 | 1.15E-05 | -9.19E-03 | 2.10E-03 |
| Standard Deviation | - | 7.33E-07 | 3.06E-07 | 1.31E-03 | 1.01E-04 |
| Coefficient of Variation (%) | - | 1.40 | 2.65 | 14.30 | 4.83 |

Strain data in the x and y directions were obtained for areas to right and left of the hole as well as above and below the hole. In these areas, the x and y strains matched closely with the principal strains.

Figure 27 presents the average strain in the y direction in the areas to the left and right of the hole. The x strain for the area above the hole is shown in Figure 28 and for the area below the hole in Figure 29.

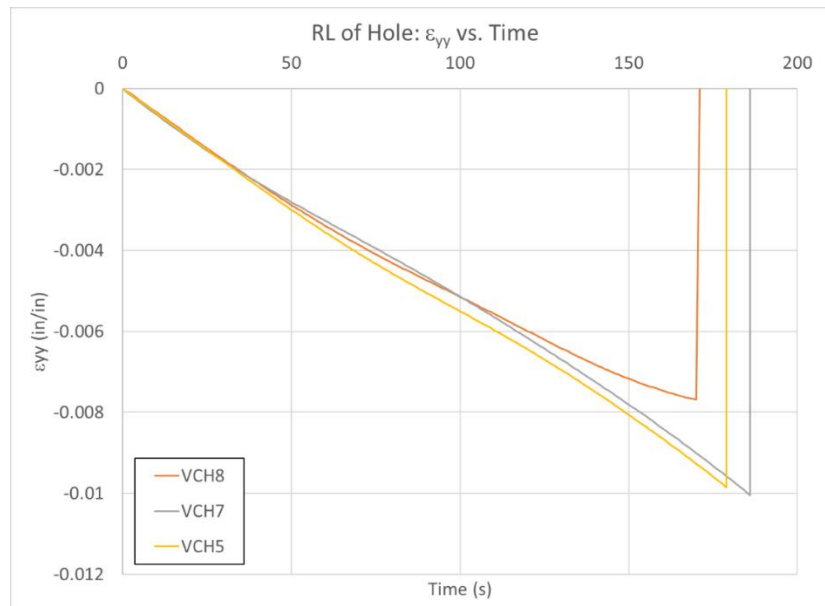


Figure 27. Compression stress concentration RL of hole ϵ_{yy} vs. time

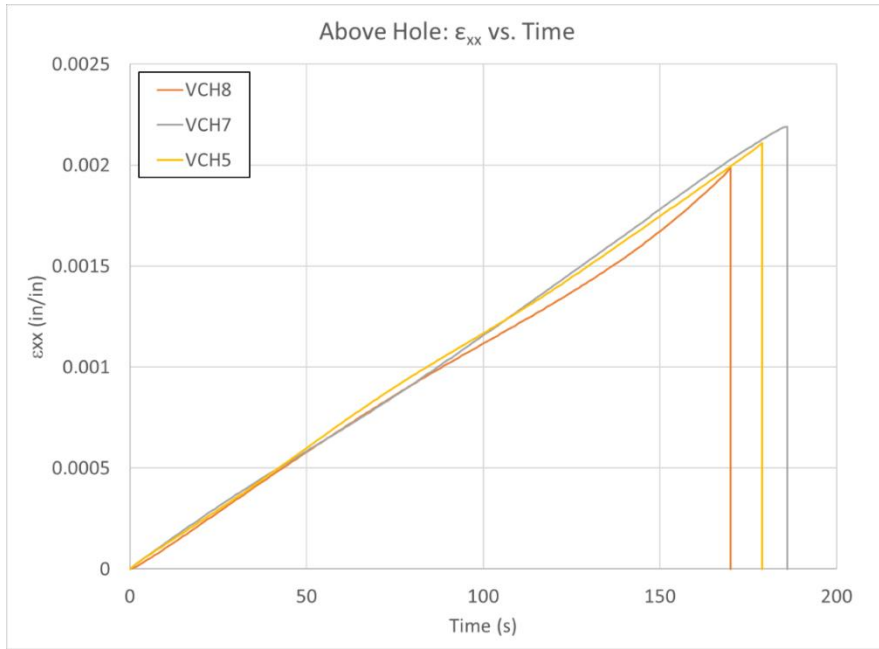


Figure 28. Compression stress concentration: above hole ϵ_{xx} vs. time

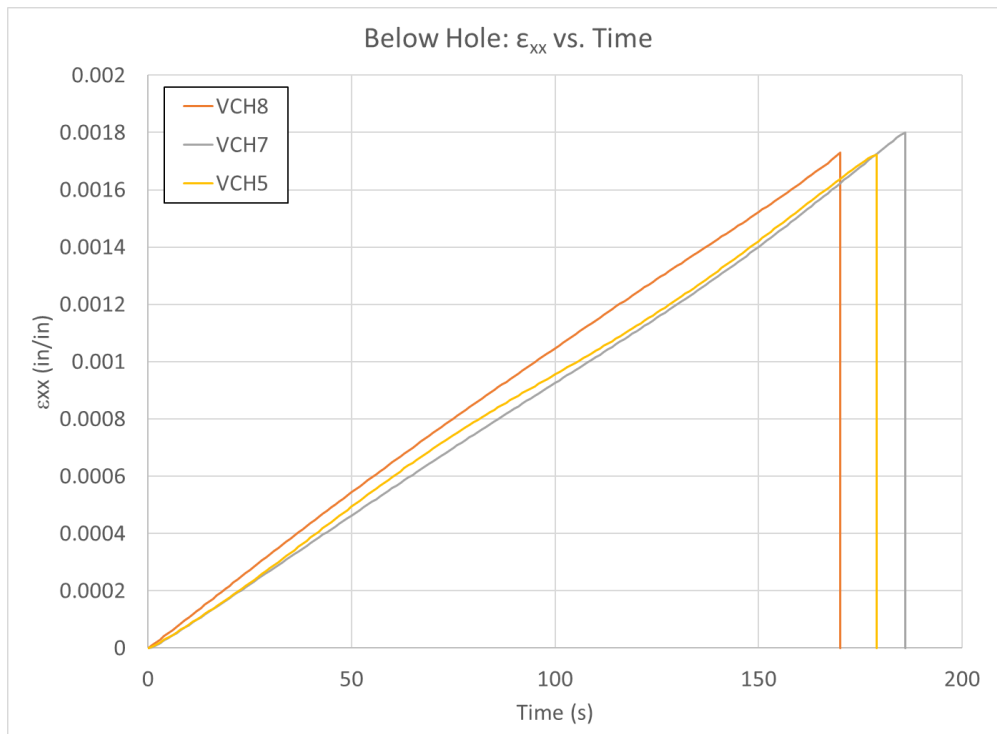


Figure 29. Compression stress concentration: below hole ϵ_{xx} vs. time

4.6 Experimental observations

The failure of all tests occurred very rapidly, much faster than the frame rate of the DIC images, thus no data was obtained through DIC showing failure onset. However, comparisons were still made between the tests as to the deformation shown through DIC. In addition, comparisons between failure patterns were made by visual observations of the failed specimens after completion of the tests.

The tension tests typically failed in a manner that affected nearly one inch of the gage section. Post-test images shown in Figure 12 depict delamination of the outer plies from the inner plies, while the inner plies did not show delamination. After complete failure of the outer plies, they delaminated on either side of the fracture zone by approximately one half inch, this delamination is observed in Figure 12(i).

The tension with hole tests showed a more localized failure for the outer plies. Top down views of the post-test gage section, as in Figure 16(e), show a clear line of fracture along which the outer plies failed. These tests showed delamination on the side of the specimen similar to that of the tension tests without the hole.

The compression tests showed a failure pattern that extended throughout the entirety of the half-inch gage section length. Though the three tested specimens had similar failure strengths, the failure patterns are different. Figure 16(d) shows a tested specimen in which the outer plies failed and delaminated for the length of the gage section, while delamination was not observed for the inner plies. Figure 16(b) shows a tested specimen with a diagonal failure pattern, extending from the top of the thickness on one end of the gage section, to the bottom at the other end of the gage section. This diagonal failure pattern suggests that there was some asymmetry in the loading of the specimen through the CLC fixture.

The compression with hole tests resulted in failure patterns that did not extend for the entire length of the gage section. These tests failed at the center gage section, at the hole, and did not show delamination in the outer plies to the extent that some of the compression without hole tests. The failure pattern on the edge of the specimen through the thickness as shown in Figure 26(c) resembles the diagonal failure pattern of the compression test shown in Figure 16(b). However, other compression with hole tests did not have a distinct diagonal failure, and instead show delamination between multiple layers of the composite, between outer and inner plies, such as those seen in Figure 26(f) and Figure 26(i).

5 QS-RT fracture mode test details and results

5.1 Overview

Delamination testing was performed on the T800/F3900 composite material to help build cohesive zone models (CZM), i.e. for the use of LS-DYNA MAT 138 (MAT_COHESIVE_MIXED_MODE). Experimental tests were performed characterizing delamination of the material and these tests were then replicated in LS-DYNA simulations to calibrate the CZM.

Two types of fracture analysis tests were conducted - the end notch flexure test (ENF) and the double cantilevered beam test (DCB). The DCB and ENF tests were used to characterize mode I and mode II fracture properties respectively. The experimental tests were used to determine the critical energy release rates in mode I and mode II fracture. The other parameters required to model the CZM elements in LS-DYNA were determined by a calibration process to match experimental data.

The material model used a bilinear traction separation law for both mode 1 and mode 2 fracture. Figure 30 (Livermore Software Technology Corporation) shows the traction separation law.

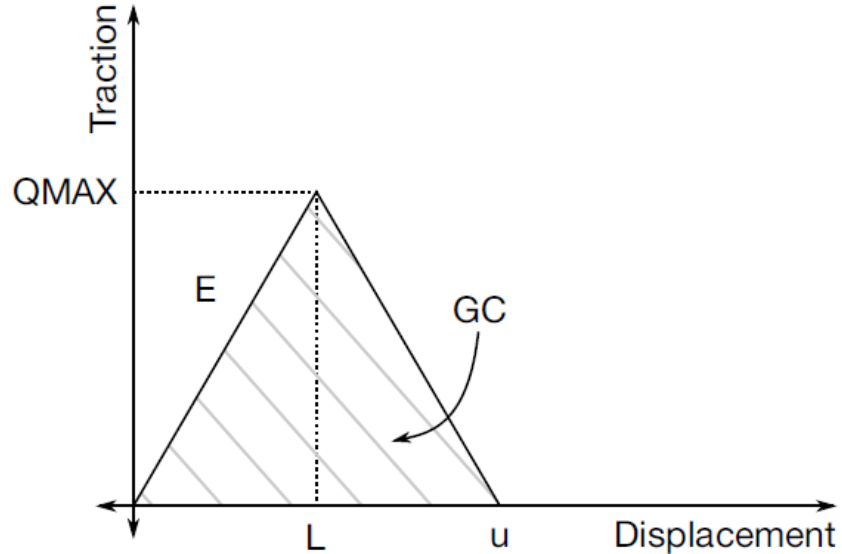


Figure 30. Traction-separation law used in MAT 138

Six parameters completely describe the separation laws for both mode 1 and mode 2 and they are summarized in Table 15.

Table 15. MAT 138 parameter summary

| Parameter | Opening Mode | Description | Units | Method Obtained |
|-----------|--------------|---|---------------|--|
| G_{IC} | 1 | critical energy release rate in mode I fracture | Energy/area | Experimentally |
| EN | 1 | initial stiffness of the cohesive zone normal to the plane of the elements | Stress/length | Calibration through LS-DYNA simulation |
| T | 1 | peak tensile traction | Stress | Calibration through LS-DYNA simulation |
| G_{IIC} | 2 | critical energy release rate in mode II fracture | Energy/area | Experimentally |
| ET | 2 | initial stiffness of the cohesive zone tangent to the plane of the elements | Stress/length | Calibration through LS-DYNA simulation |
| S | 2 | peak tangential (shear) traction | Stress | Calibration through LS-DYNA simulation |

5.2 General experimental procedures

Unless otherwise noted, all preparation, equipment, and procedures are the same as stated in Section 3 of this report.

5.2.1 Sample preparation

The ENF and DCB tests were performed using the T800/F3900 composite material manufactured by Toray Composites, Seattle, WA (T. C. M. America). Test coupons were cut from 16 in x 16 in panels comprised of 24 layers of unidirectional fibers. The panels were manufactured with 2-inch long Teflon® film inserts on two opposite edges in the center layer through the thickness. These inserts provide an initial delamination such that the top and bottom halves of the panels were not bonded along these edges. Figure 31 below shows examples of coupon cuts from the boards. The two horizontal white lines in the figure mark the end of the inserts.

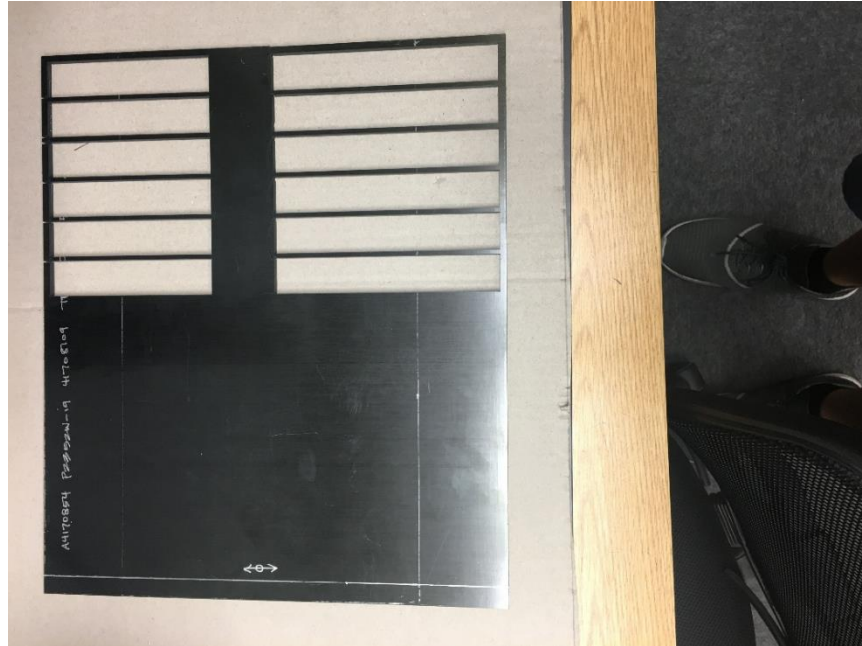


Figure 31. ENF and DCB manufactured boards showing test coupons cut from the original panel

Both DCB and ENF samples were cut with waterjet with the same specifications as given in section 2.1.

DCB tests were conducted with piano hinges obtained from Material Testing Technology⁶. Figure 32 shows an example of the piano hinges used for these tests.



Figure 32. Piano hinges for DCB test

⁶ <http://www.mttusa.net/ISOS.15024.10.html>

The piano hinges were bonded to the DCB test coupons using 3M DP420 Scotch Weld⁷ toughened two-part epoxy. This was a different epoxy from that used for bonding the fiberglass tabs in the stacked-ply validation tests. The DP420 epoxy gave higher strength when bonding to the piano hinges as compared to the DP460 epoxy.

All specimens were prepared in the same manner unless otherwise noted. The following list outlines the steps taken to prepare the specimens.

1. For DCB Tests: the regions on a typical specimen where piano hinges were bonded were lightly sanded using 220 grit sandpaper. Sanding the surfaces ensured a complete bond between the specimen and hinges. The piano hinges were sanded with 100 grit sandpaper to scuff and scratch the surface of the bond area.
2. The sanded surfaces were then cleaned using cotton swabs soaked with isopropyl alcohol. The surfaces were allowed to air dry until there was no visible moisture on the bonding surfaces.
3. The 3M epoxy was mixed in accordance to the manufacturer's recommendation. A thin layer of the mixed epoxy was applied to the piano hinge using a wooden applicator.
4. The tabs were placed on the specimen and positioned until the surfaces of the specimen and the tabs were in complete contact and aligned properly in the desired region.
5. The specimens were allowed to cure at room temperature and atmospheric pressure for 24 hours.
6. For All Tests: Next, one face of the thickness of the specimen was painted and speckled. Speckling of the specimen involved first spraying the surface of the specimen with a layer of white paint with a flat finish. Paint was sprayed onto the surface until the specimen can no longer be seen. The paint was allowed to completely dry at room temperature.
7. After the white paint dried, black paint, with a flat finish, was sprayed onto the dry white paint. The black paint was sprayed in a manner that results in random array of black dots being deposited on the white area of the specimen.

⁷https://multimedia.3m.com/mws/media/669980/scotch-weldtm-epoxy-adhesive-dp420-blck-ns-blck-offwhit-lh.pdf&fn=420_090216_R4.pdf

8. After the specimens had been painted, they were allowed to finishing curing for another 24 hours as recommended by the manufacturer.
9. The location of the end of the insert was marked on the speckled surface so as to be clearly seen in the DIC images.
10. For ENF Tests: The calibration markings were added to the top surface of the specimen according to the ASTM standards for this test.

5.2.2 Test machines, fixtures, equipment and software

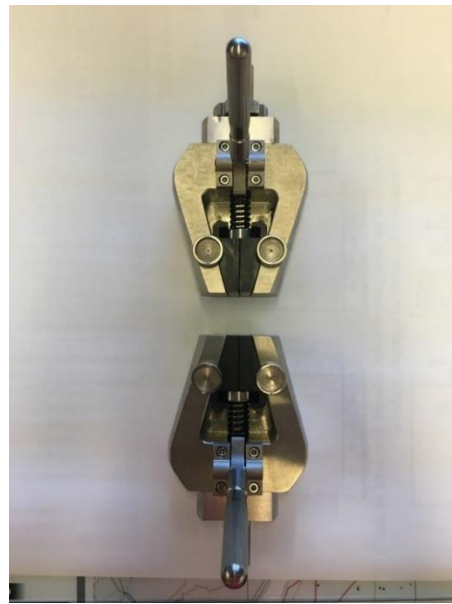
All ENF and DCB tests were performed using an MTS Exceed Model E42⁸ machine with a load cell model number BSS-XS-500KG⁹ (Figure 33(a)). DCB tests were performed using spring-loaded grips as shown in Figure 33(b) and Figure 33(c). ENF tests were performed using a 3-point bend fixture as shown in Figure 33(d).

⁸ https://www.mts.com/cs/groups/public/documents/library/mts_2011071.pdf

⁹ <https://shop.transcell.com/wp-content/uploads/2016/06/BSS.pdf>



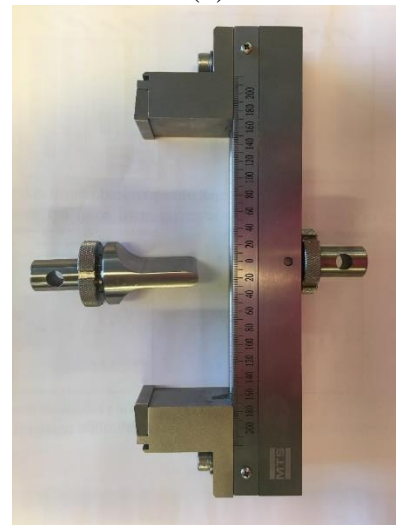
(a)



(b)



(c)



(d)

Figure 33. Test machines and fixtures (a) MTS load frame (b) Spring loaded grips front view (c) Spring loaded grips side view (d) 3-point bend fixture

Digital Image Correlation (DIC) Equipment: Two Point Grey Grasshopper 3 cameras were used to capture images of the specimen throughout the duration of the experiment. Attached to one of the cameras was a Tokina 100 mm lens¹⁰ while the other camera was used with the Schneider 35 mm lens as shown in Figure 34. The Tokina lens attached to the Point Grey Grasshopper 3

¹⁰ <http://tokinalens.com/download/product/5ab25b6cf1d39.pdf>

camera is shown in Figure 35. The Tokina lens has a higher resolution and was used to capture images for DIC processing. This camera was focused on the area of the initial crack tip. The Schneider lens provided images of the entire specimen to track and record the overall progress of the test. DIC processing was carried out with VIC 2D (Correlated Solutions), a software program that requires images from only one camera for analysis. The two cameras were therefore independent of each other.



Figure 34. Typical camera setup for ENF and DCB tests, Tokina 100 mm lens (top) and Schneider 35 mm lens (bottom)



Figure 35. Tokina 100 mm lens on Point Grey Grasshopper 3 camera

5.2.3 Typical test procedure

ASTM D5528-13 (ASTM, 2013) was used as a guideline to create the experimental setup. The experimental test yielded the value of G_{IC} , the critical energy release rate in mode I fracture (units of energy/area). The test setup is shown in Figure 36 (ASTM, 2013).

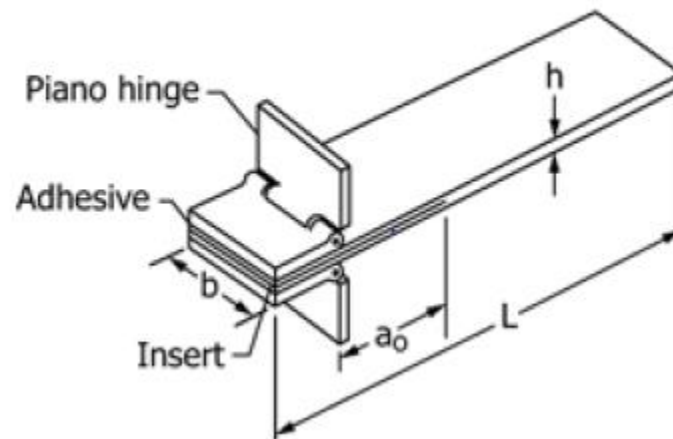


Figure 36. DCB test setup

Calculations followed the ASTM procedure to determine the G_{IC} values for both the non-precracked (NPC) and precracked (PC) conditions. The NPC condition meant the insert acted as the source of initial delamination with no further cracking induced in the specimen. Testing in the NPC condition to a desired crack propagation as per the ASTM, yielded the PC condition, i.e. the PC condition was that in which some cracking had been induced in the specimen beyond the initial insert.

Figure 37 shows an example of the DCB test being conducted after some delamination has occurred.



Figure 37. DCB test

A loading rate of 1.2 mm/min was used for all tests. The NPC tests were loaded until a controlled crack growth of 5 mm was reached. The PC tests were loaded until complete separation of the top and bottom halves of the specimen.

As per the ASTM standard, the initiation value of G_{IC} was calculated 12 times. Three different definitions for an initiation value of G_{IC} were used including the point of deviation from linearity in the load-displacement curve (NL), the point at which delamination was visually observed on the edge (VIS), and the point at which the load had reached a maximum value (MAX) (ASTM, 2013). For each definition of the initiation value of G_{IC} , four different methods of calculation were used including modified beam theory (MBT), rotation corrected modified beam theory (RCMBT), compliance calibration (CC), and modified compliance calibration (MCC).

The calculation for the strain-energy release rate using MBT is given as:

$$G_I = \frac{3P\delta}{2ba} \quad 2$$

P is the load, δ is the load point displacement, b is the specimen width, and a is the delamination length. The calculation for the strain-energy release rate using RCMBT is given as:

$$G_I = \frac{3P\delta}{2b(a+|\Delta|)} \quad 3$$

The variables are the same as in equation 2 and Δ is determined experimentally through a relationship of the compliance and crack length. The calculation for the strain-energy release rate using CC is given as:

$$G_I = \frac{nP\delta}{2ba} \quad 4$$

The variables are the same as in equation 2 and n is the slope of the compliance calibration line of best fit. The calculation for the strain-energy release rate using MCC is given as:

$$G_I = \frac{3P^2C^{2/3}}{2A_1bh} \quad 5$$

The variables are the same as in equation 2 in addition to C being the compliance and A_1 being the slope of the line of best fit between the relationship of the normalized specimen thickness against the cubic root of compliance. Full procedures for all of the methods of calculations and further details of the test procedure can be found in ASTM D5528-13 (ASTM, 2013).

ENF Test

ASTM D7905/D7905M-14 (ASTM, 2014) was used as a guideline to create the experimental setup. The experimental test yielded the value of G_{IIC} , the critical energy release rate in mode II fracture (units of energy/area). The test setup is shown in Figure 38.

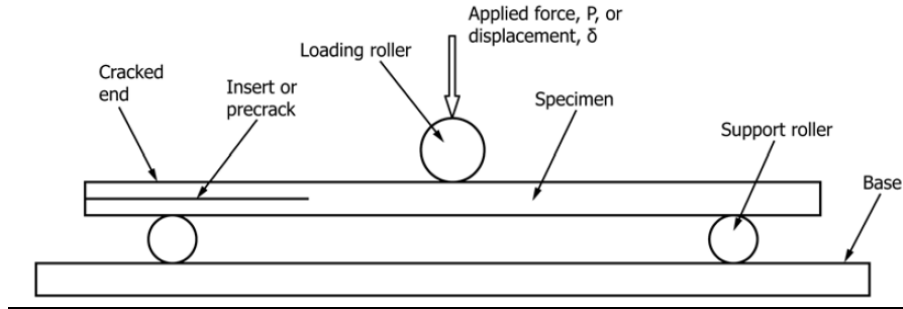


Figure 38. ENF 3-point test setup

The ASTM procedure was followed to calculate the G_{IIC} values for both the NPC and PC conditions. For each condition, two calibration cycles were performed, followed by a fracture cycle. The calibration and fracture cycles were conducted on the same test specimen. The compliance of the specimen for each cycle was computed as the linear portion of the relationship between the load and displacement. The span between the support rollers was left constant across all cycles to ensure that the change in compliance was only a function of the crack length. The three cycles combined were used in the compliance calibration process to find a linear least squares regression on the relationship between the compliance of each cycle and the crack length of each cycle. Finally, the fracture test was used to calculate the G_{IIC} value as

$$G_{IIC} = \frac{3mP_{Max}^2 a_0^2}{2B} \quad 6$$

The variable m is the CC coefficient, P_{max} is the maximum force from the fracture test, a_0 is the crack length in the fracture test, and B is the specimen width.

Figure 39 shows an example of the ENF being conducted.

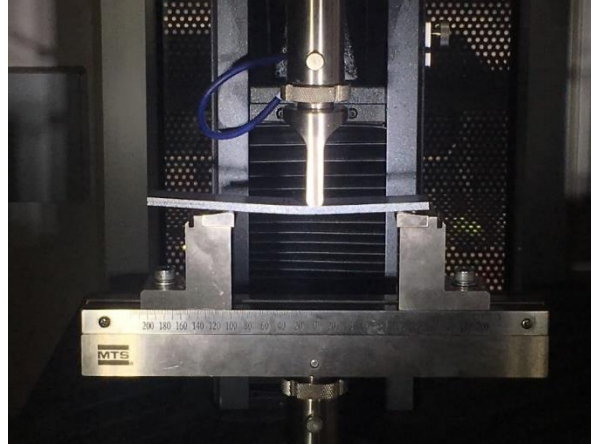


Figure 39. ENF test

Further details of the test procedure can be found in ASTM D7905/D7905M-14 (ASTM, 2014).

5.2.4 Post-processing of test data

ASTM standards were followed. At each data collection time, the force and displacement at the load point were extracted from the MTS machine. For the DCB tests, it was also necessary to track and record two other parameters during the test - the crack tip opening displacement and the crack propagation length. These parameters were obtained using DIC software, VIC-2D 2009 (Correlated Solutions). Displacement data was obtained using DIC software and used to verify the displacement output of the MTS machine. Figure 40 shows DIC y-displacement data plotted on a DCB test coupon during the test.

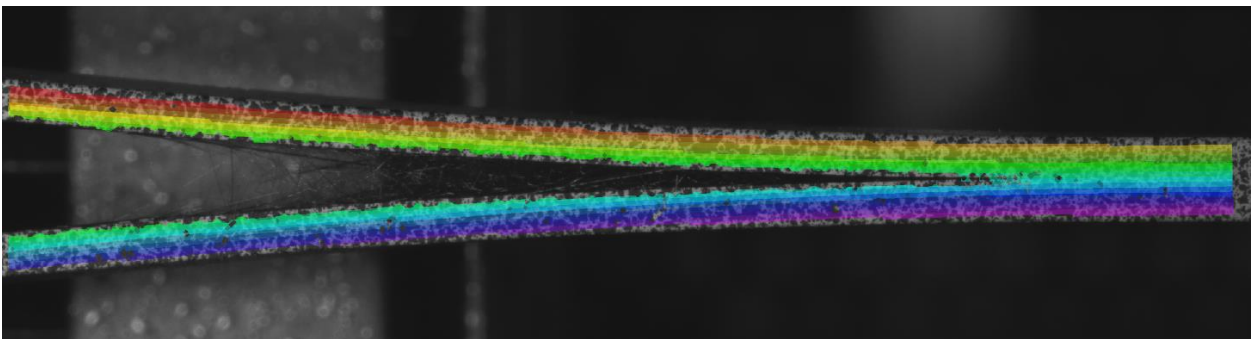


Figure 40. Y-displacement DIC data for DCB test

The VIC-2D 2009 software has a crack opening data (COD) tool that was used to monitor the length of the crack in the cohesive layer between the top and bottom halves of the test coupon. The COD tool employed on the ENF test coupon is shown in Figure 41.

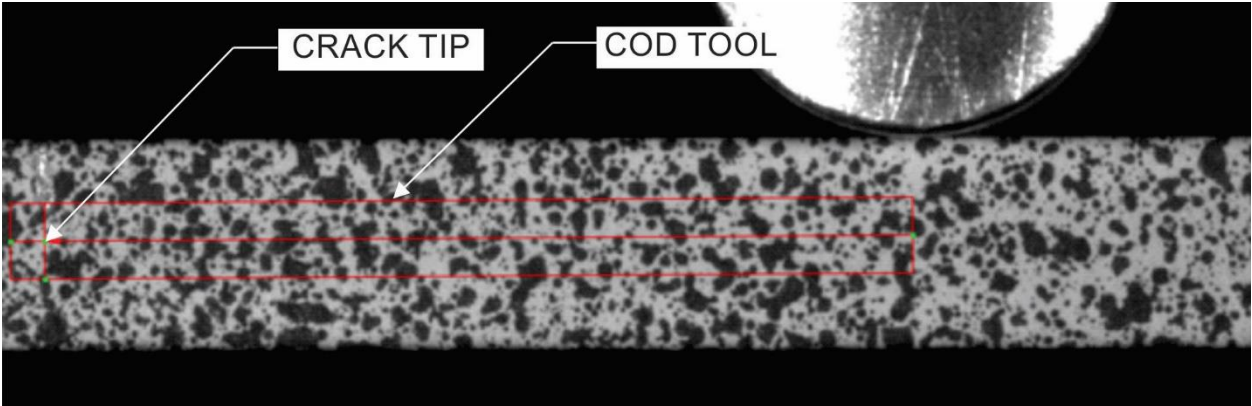


Figure 41. COD tool on ENF specimen

While the COD tool had multiple capabilities, it primarily was used in the DCB tests to determine the crack tip opening displacement and the crack propagation length at any point in time of the test. The COD tool is shown in Figure 42 on the DCB specimen after some delamination has occurred. Note that the tool could only be shown on the reference, or first, image of the test.

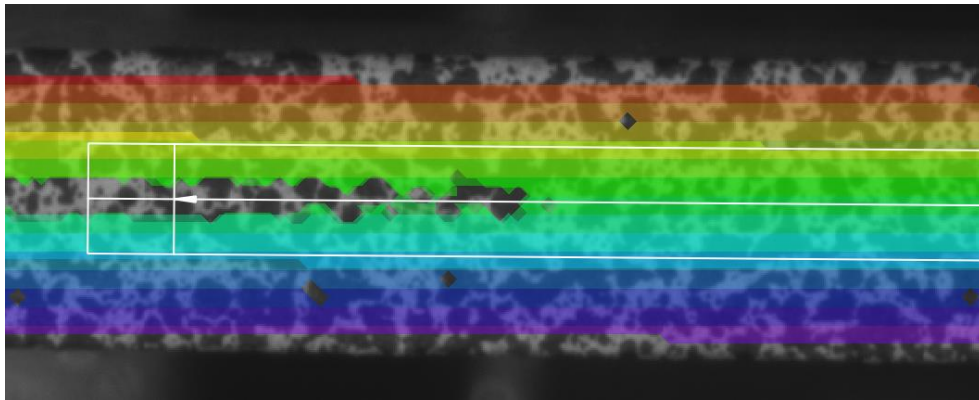


Figure 42. COD tool on DCB specimen

The data collected with this tool and the data from the MTS machine allowed for the calculation of the strain-energy release rates.

5.3 Experimental results

5.3.1 ENF Test

Specimen Geometry: ASTM D7905 (ASTM, 2014) standard is applicable for this test. The specimen geometry and layout are shown in Figure 43.

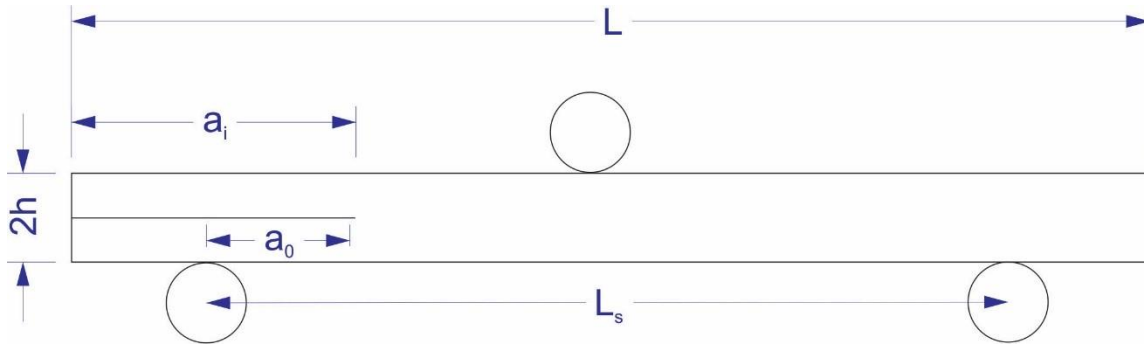


Figure 43. Typical specimen geometry and layout

The average specimen dimensions of the test replicates are shown in Table 16.

Table 16. ENF Test Specimen Dimensions

| Replicate ID | a_i (in) | a_0 (mm) | h (in) | b (in) | L (in) |
|------------------------------|------------|------------|----------|----------|----------|
| ENF-2 | 2.349 | 20,30,40 | 0.097 | 1.008 | 6.560 |
| ENF-3 | 2.357 | 20,30,40 | 0.093 | 1.004 | 6.575 |
| ENF-4 | 2.352 | 20,30,40 | 0.093 | 1.003 | 6.555 |
| ENF-5 | 2.358 | 20,30,40 | 0.094 | 1.005 | 6.555 |
| ENF-6 | 2.362 | 20,30,40 | 0.093 | 1.003 | 6.530 |
| Average | 2.356 | - | 0.094 | 1.005 | 6.555 |
| Standard Deviation | 0.005 | - | 0.001 | 0.002 | 0.016 |
| Coefficient of Variation (%) | 0.215 | - | 1.586 | 0.205 | 0.247 |

Specimen Photographs: The specimen photographs before the tests are shown in Figure 44. After testing images are shown in Figure 45.



(a)



(b)

Figure 44. Example image of ENF specimen before testing (a) Top surface showing specimen width (b) Side of specimen showing thickness



(a)



(b)

Figure 45. Example image of ENF specimen after testing (a) Top surface showing specimen width (b) Side of specimen showing thickness

Test Results: The summary of the results from the Non-precracked tests is shown in Table 17. The variable *acalc* in this table refers to the post-test crack length as calculated using unload data along with the compliance calibration coefficients *m* and *A*. The variable *ameas* refers to the post-test crack length measured by visual observation and a digital caliper. The summary of the results from the pre-cracked tests is shown in Table 18.

Table 17. Test Summary for ENF Non-precracked Tests

| NPC | | | | | | |
|------------------------------|-------------------------|----------|----------------------------------|-----------------------------------|-------------------|-------------------|
| Name | m ($N^{-1}mm^{-2}$) | A [mm/N] | G_{IIc} [$N\text{-mm}/mm^2$] | G_{IIc} [$lb\text{-in}/in^2$] | <i>acalc</i> [mm] | <i>ameas</i> [mm] |
| TFENF-2 | 9.98E-09 | 1.32E-03 | 2.28 | 13.02 | 50.98 | 49.23 |
| TFENF-3 | 1.02E-08 | 1.28E-03 | 2.40 | 13.72 | 49.98 | 47.71 |
| TFENF-4 | 8.95E-09 | 1.32E-03 | 2.35 | 13.43 | 52.79 | 53.15 |
| TFENF-5 | 9.72E-09 | 1.28E-03 | 2.35 | 13.44 | 50.90 | 48.74 |
| TFENF-6 | 9.47E-09 | 1.28E-03 | 2.26 | 12.87 | 51.32 | 48.59 |
| Average | 9.67E-09 | 1.30E-03 | 2.33 | 13.30 | 51.20 | 49.48 |
| Standard Deviation | 4.95E-10 | 2.21E-05 | 0.06 | 0.35 | 1.02 | 2.12 |
| Coefficient of Variation (%) | 5.12 | 1.71 | 2.60 | 2.60 | 1.99 | 4.29 |

Table 18. Test Summary for ENF Precracked Tests

| PC | | | | | |
|------------------------------|-------------------------|------------|----------------------------------|-----------------------------------|-----------------|
| Name | m ($N^{-1}mm^{-2}$) | A [mm/N] | G_{IIC} [$N\text{-}mm/mm^2$] | G_{IIC} [$lb\text{-}in/in^2$] | a_{calc} [mm] |
| TFENF-2 | 1.17E-08 | 1.12E-03 | 1.75 | 9.99 | -45.77 |
| TFENF-3 | 1.06E-08 | 1.10E-03 | 1.84 | 10.51 | -46.98 |
| TFENF-4 | 1.04E-08 | 1.07E-03 | 1.70 | 9.69 | -46.86 |
| TFENF-5 | 9.04E-09 | 1.05E-03 | 1.92 | 10.94 | -48.73 |
| TFENF-6 | 1.05E-08 | 1.05E-03 | 2.00 | 11.39 | -46.41 |
| Average | 1.04E-08 | 1.08E-03 | 1.84 | 10.50 | -46.95 |
| Standard Deviation | 9.47E-10 | 3.22E-05 | 0.12 | 0.69 | 1.10 |
| Coefficient of Variation (%) | 9.06 | 2.99 | 6.56 | 6.56 | -2.35 |

The experimental results for the measured load and displacement that occurred at the load point are shown in Figure 46.

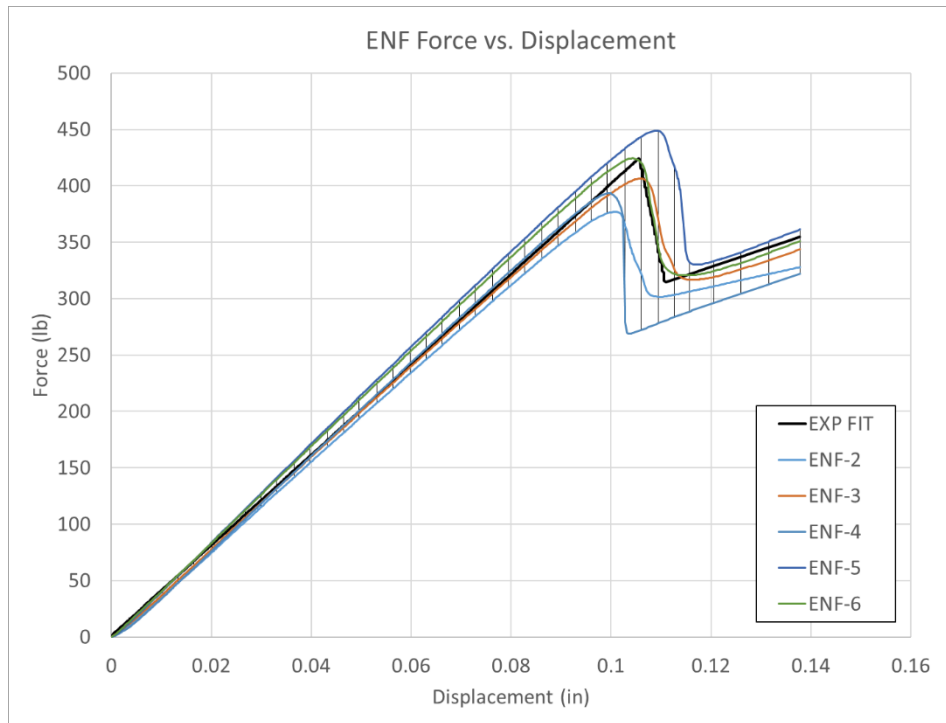


Figure 46. ENF precrack experimental force vs. displacement

Five experimental curves are shown for test specimens with the precrack procedure. The experimental data across each replicate was fitted using polynomial regression to form an

experimental model curve. This is labeled at “EXP FIT” in Figure 46. The whisker plot depicts the range of the experimental data. The specifications of the regression are given in Table 19.

Table 19. ENF Experimental Regression Specifications

| Section | Fit Type | R ² |
|-----------|----------|----------------|
| Pre-peak | Linear | 0.983 |
| Post-peak | Linear | 0.522 |

5.3.2 DCB Test

Specimen Geometry: ASTM D5528 (ASTM, 2013) standard was applicable for this test. The specimen geometry and layout are shown in Figure 47.

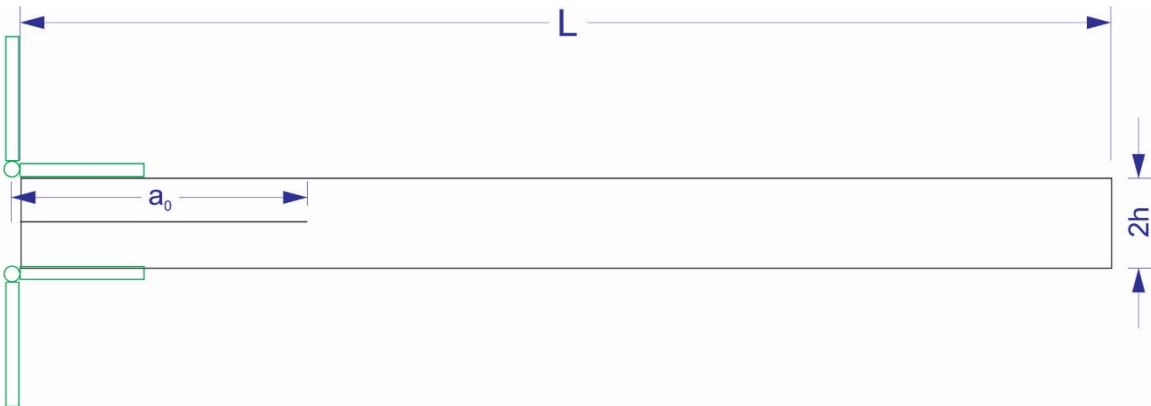


Figure 47. Typical specimen geometry and layout

Table 20 shows the average specimen dimensions of the test replicates.

Table 20. DCB Test Specimen Dimensions

| Replicate ID | a ₀ (in) NPC | a ₀ (in) PC | h (in) | b (in) | L (in) |
|------------------------------|----------------------------|------------------------|----------|----------|----------|
| DCB-3 | 2.291 | 2.625 | 0.094 | 1.007 | 4.999 |
| DCB-4 | 2.277 | 2.652 | 0.094 | 1.003 | 5.002 |
| DCB-5 | 2.311 | 2.624 | 0.093 | 1.004 | 5.002 |
| DCB-6 | 2.314 | 2.866 | 0.093 | 1.003 | 4.994 |
| Average | 2.298 | 2.692 | 0.093 | 1.004 | 4.999 |
| Standard Deviation | 1.76E-02 | 1.17E-01 | 4.59E-04 | 2.24E-03 | 3.93E-03 |
| Coefficient of Variation (%) | 0.77 | 4.35 | 0.49 | 0.22 | 0.08 |

Specimen Photographs: The specimen photographs before the tests are shown in Figure 48. After testing images are shown in Figure 49.



(a)



(b)

Figure 48. Example image of DCB specimen prior to testing (a) Top surface showing specimen width (b) Side of specimen showing thickness

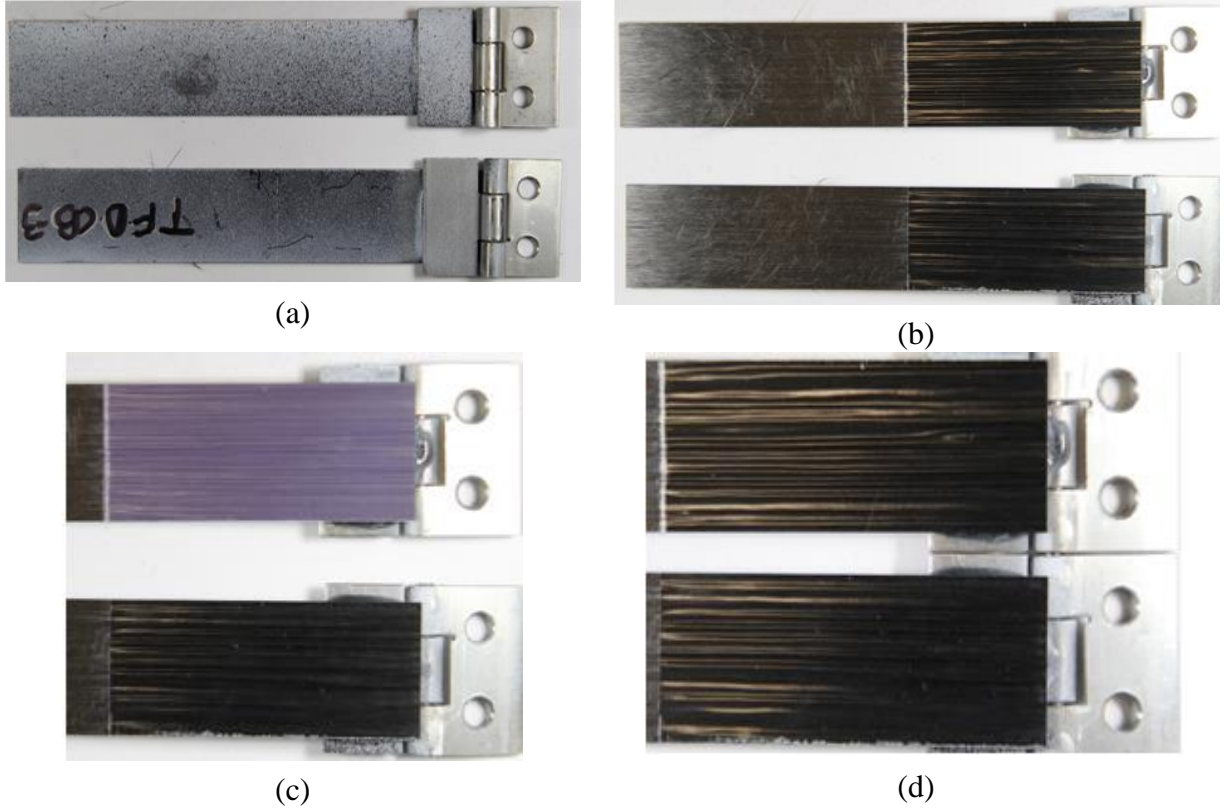


Figure 49. Example image of DCB specimen after testing (a) Exterior top and bottom surfaces (b) Interior surfaces (c) Film (d) Initial crack area

Test Results: The experimental results for the measured load and displacement that occurred at the load point are shown in Figure 50.

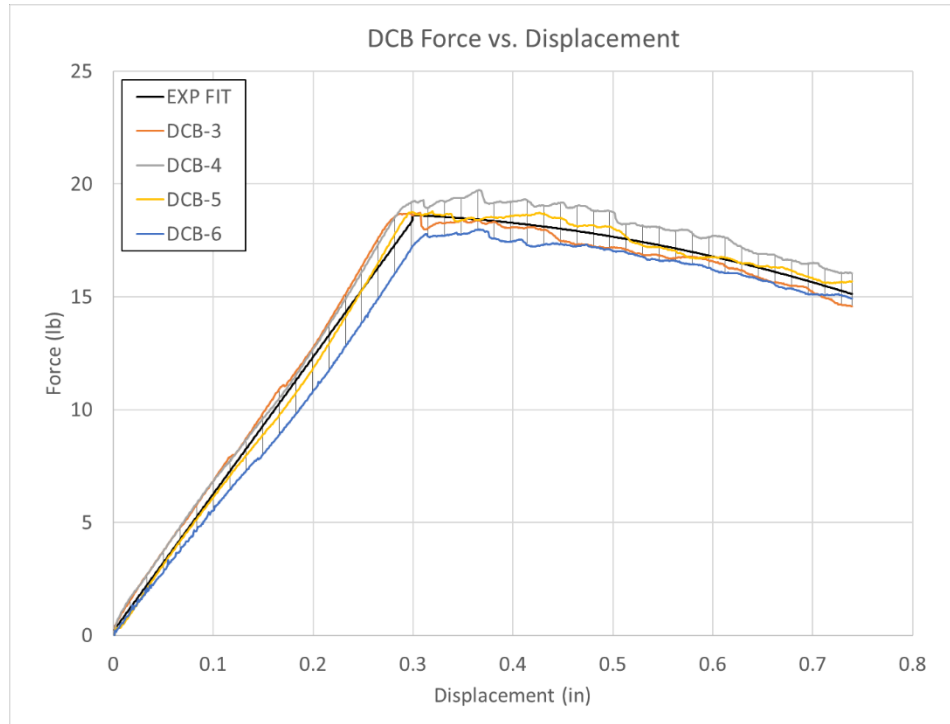


Figure 50. DCB precrack experimental force vs. displacement

Four experimental curves are shown for test specimens with the precrack procedure. The experimental data across each replicate was fitted using polynomial regression to form an experimental model curve. This is labeled at “EXP FIT” in Figure 50. The whisker plot depicts the range of the experimental data. The specifications of the regression are given in Table 21.

Table 21. DCB experimental regression specifications

| Section | Fit Type | R ² |
|-----------|-----------|----------------|
| Pre-peak | Linear | 0.981 |
| Post-peak | Quadratic | 0.756 |

The summary of the results from the non-precracked tests is shown in Table 22.

Table 22. Test summary for DCB non-precracked tests

| NPC | | | | |
|------------------------------|--|------------------------------|-----------|------------|
| Name | MAX G_{IC} [lb-in/in²] | | | |
| | MBT | MBT w/ Rot Correction | CC | MCC |
| TFDCB-3 | 4.70 | 3.31 | 3.64 | 3.31 |
| TFDCB-4 | 4.83 | 3.38 | 3.50 | 2.30 |
| TFDCB-5 | 4.15 | 2.71 | 2.99 | 3.25 |
| TFDCB-6 | 5.24 | 3.06 | 4.99 | 4.99 |
| Average | 4.73 | 3.11 | 3.78 | 3.46 |
| Standard Deviation | 0.45 | 0.30 | 0.85 | 1.12 |
| Coefficient of Variation (%) | 9.51 | 9.78 | 22.57 | 32.35 |

The summary of the results from the precracked tests are separated into three tables each for the different measures for the G_{IC} value. Table 23 shows the results for the non-linear G_{IC} measure for the precracked tests. This was the measure of G_{IC} when the force vs. displacement relationship of the test becomes non-linear.

Table 23. Test summary for DCB precracked tests – non-linear

| PC | | | | |
|------------------------------|---|------------------------------|-----------|------------|
| Name | NL G_{IC} [lb-in/in²] | | | |
| | MBT | MBT w/ Rot Correction | CC | MCC |
| TFDCB-3 | 2.66 | 2.07 | 2.24 | 2.07 |
| TFDCB-4 | 2.96 | 2.24 | 2.35 | 2.25 |
| TFDCB-5 | 3.10 | 2.25 | 2.40 | 2.27 |
| TFDCB-6 | 2.73 | 2.17 | 2.26 | 2.17 |
| Average | 2.86 | 2.18 | 2.31 | 2.19 |
| Standard Deviation | 0.20 | 0.08 | 0.08 | 0.09 |
| Coefficient of Variation (%) | 7.11 | 3.88 | 3.34 | 4.17 |

Table 24 shows the results for the visible G_{IC} measure for the precracked tests. This is the measure of G_{IC} when the crack propagation from the initial crack becomes visible.

Table 24. Test summary for DCB precracked tests – visible

| PC | | | | |
|-------------|--|------------------------------|-----------|------------|
| Name | VIS G_{IC} [lb-in/in²] | | | |
| | MBT | MBT w/ Rot Correction | CC | MCC |
| TFDCB-3 | 2.83 | 2.20 | 2.38 | 2.20 |
| TFDCB-4 | 3.09 | 2.34 | 2.46 | 2.35 |

| PC | | | | |
|------------------------------|--|------------------------------|-----------|------------|
| Name | VIS G_{Ic} [lb-in/in²] | | | |
| | MBT | MBT w/ Rot Correction | CC | MCC |
| TFDCB-5 | 3.11 | 2.26 | 2.41 | 2.29 |
| TFDCB-6 | 2.77 | 2.20 | 2.29 | 2.21 |
| Average | 2.95 | 2.25 | 2.39 | 2.26 |
| Standard Deviation | 0.18 | 0.07 | 0.07 | 0.07 |
| Coefficient of Variation (%) | 6.00 | 2.96 | 2.93 | 2.95 |

Table 25 shows the results for the maximum G_{Ic} measure for the precracked tests. This is the measure of G_{Ic} when the peak force is reached.

Table 25. Test summary for DCB precracked tests – maximum

| PC | | | | |
|------------------------------|--|------------------------------|-----------|------------|
| Name | MAX G_{Ic} [lb-in/in²] | | | |
| | MBT | MBT w/ Rot Correction | CC | MCC |
| TFDCB-3 | 3.04 | 2.38 | 2.56 | 2.42 |
| TFDCB-4 | 3.63 | 2.81 | 2.88 | 2.86 |
| TFDCB-5 | 3.22 | 2.37 | 2.50 | 2.40 |
| TFDCB-6 | 3.16 | 2.55 | 2.61 | 2.57 |
| Average | 3.26 | 2.53 | 2.65 | 2.56 |
| Standard Deviation | 0.25 | 0.21 | 0.17 | 0.21 |
| Coefficient of Variation (%) | 7.81 | 8.13 | 6.40 | 8.22 |

The crack resistance curves for the duration of the tests are shown in Figure 51. This plots the strain-energy release rate against the crack length for the PC tests.

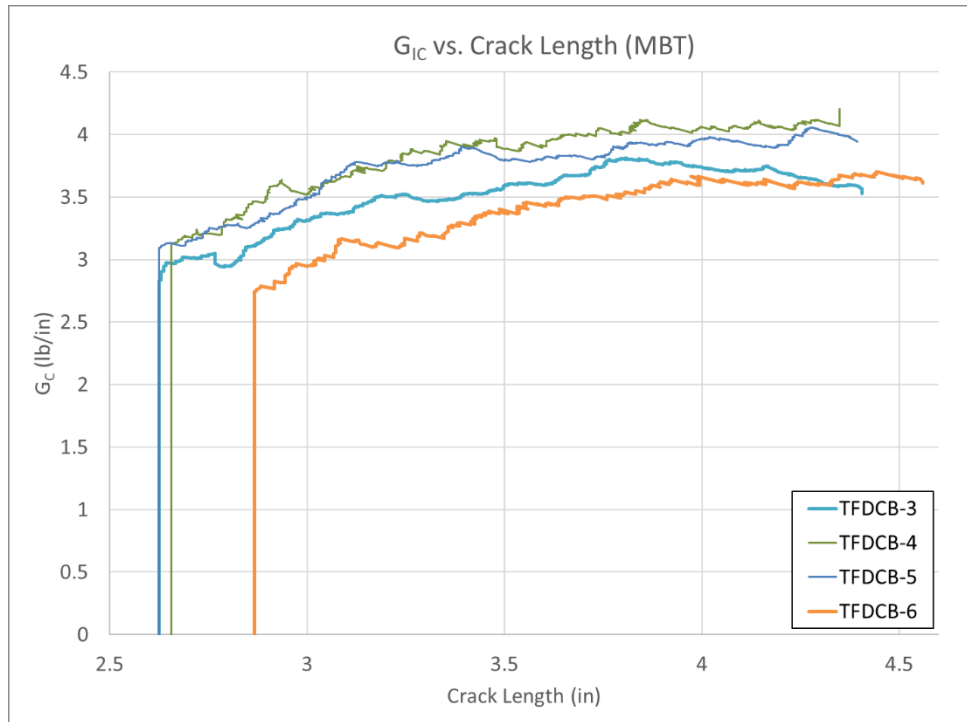


Figure 51. DCB tests crack resistance curve

The opening displacement at the location of the original crack tip is also calculated using DIC. Figure 52 shows the strain-energy release rate plotted against the crack tip opening displacement for the PC tests.

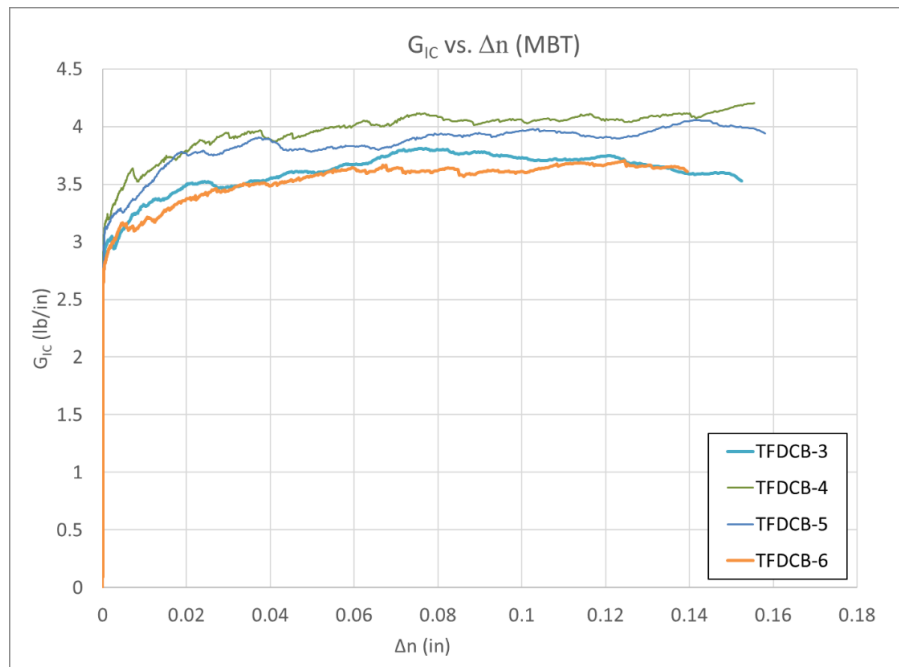


Figure 52. GIC versus crack tip opening displacement

5.4 Simulation details

Models were created in LS-DYNA for both the ENF and DCB tests. The purpose of modeling these tests was to use simulations alongside experimental data to calibrate the remaining parameters of MAT138, used for modeling cohesive zone elements. Values of G_{IC} and G_{IIC} were determined experimentally, while values for EN, ET, T, and S were not directly determined experimentally, thus calibration by simulation was required.

In both the ENF and DCB tests, a stroke displacement and a measured force were reported by the MTS machine. Simulations of each test were created to yield the same output, force, and displacement, as the experimental test. For each test, the values of EN, ET, T, and S were varied in a series of simulations to determine the parameter values that produced the best match of the experimental force vs. displacement relationships.

The geometry and boundary conditions of the models were chosen to best represent the conditions present in the experimental tests. The geometry and boundary conditions of the experimental ENF test are shown in

Figure 53 when viewing the front face of the test coupon.



Figure 53. ENF experimental geometry and BCs

For the simulation, only the portion of the test coupon between the left and right rollers was simulated. The overhangs are not included in the simulation because they are outside of the boundary conditions and have much shorter lengths than the main span, thus they have little effect on the results of the study. The geometry and boundary conditions of the simulated ENF test are shown in Figure 54.

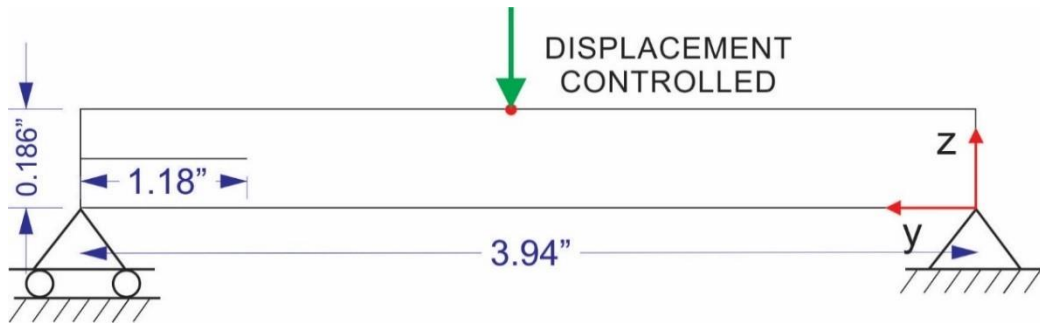


Figure 54. ENF simulation geometry and BCs

The geometry and boundary conditions of the experimental DCB test are shown in Figure 55.

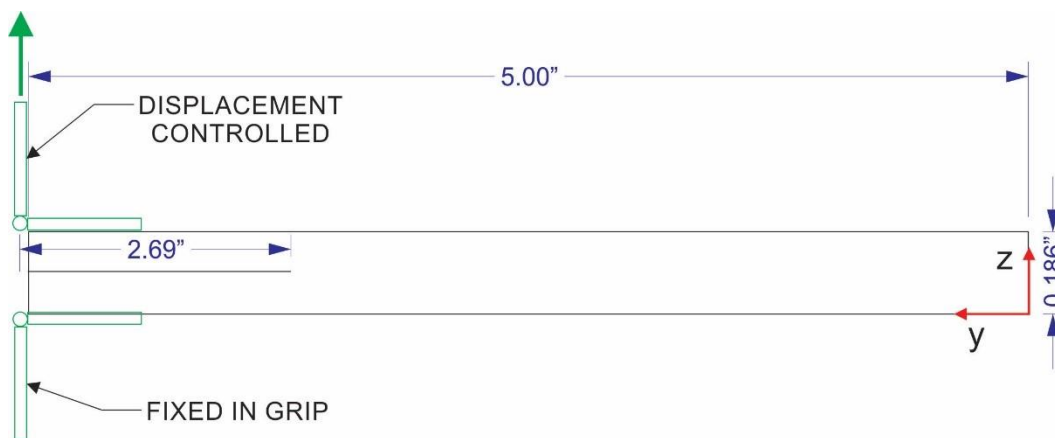


Figure 55. DCB experimental geometry and BCs

The full geometry of the DCB test was modeled in the LS-DYNA simulation. The geometry and boundary conditions are shown in Figure 56.

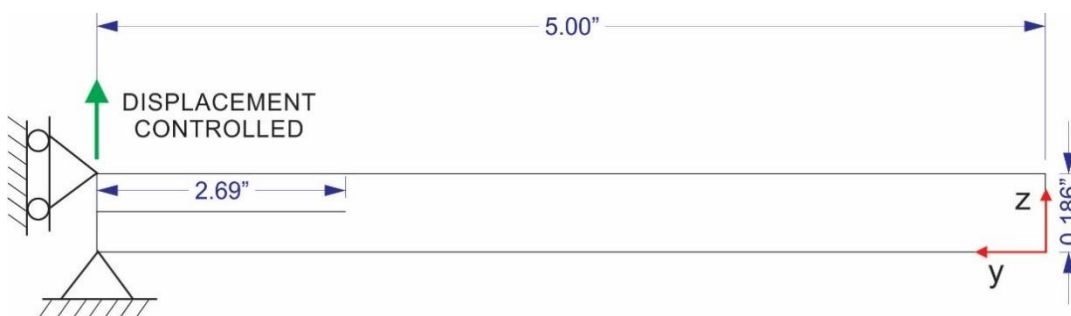


Figure 56. DCB simulation geometry and BCs

Multiple models were made with varying degrees of complexity and mesh sizes. These are listed in Table 26.

Table 26. ENF and DCB meshes

| Mesh Number | # of Cohesive zone Layers | # of Elements between cohesive layers | Size of Elements in XY plane | Solid element size ratio (X:Y:Z) |
|-------------|---------------------------|---------------------------------------|------------------------------|----------------------------------|
| 1 | 1 | 2 | 0.06 | (3:3:2) |
| 2 | 1 | 4 | 0.03 | (3:3:2) |
| 3 | 7 | 1 | 0.03 | (3:3:2) |
| 4 | 23 | 1 | 0.06 | (8:8:1) |

As expected, modeling with fewer cohesive zone layers improved the computational throughput and allowed for rough calibration of the DCB and ENF parameters. However, it was found that the number of cohesive zone layers did have a significant effect on the results of the simulation. Thus, the final model included all 23 cohesive zone layers that existed in the experimental coupons. The model with 23 cohesive zone layers was superior because it best represented the experimental conditions. The experimental test coupon had 24 layers of unidirectional fibers and thus had 23 interlaminar layers. Since the number of cohesive zone layers in the model was observed to significantly affect the compliance of the specimen, it was necessary to include all the layers.

Mesh 3 was used to perform a sensitivity study on the effect of altering each of the six ENF and DCB parameters needed for the traction separation laws. Though this model did not match the experimental data as well because only seven cohesive layers were modeled, it allowed the observation of the effects of tuning each parameter.

An example of DCB Mesh 1 is shown in Figure 57.

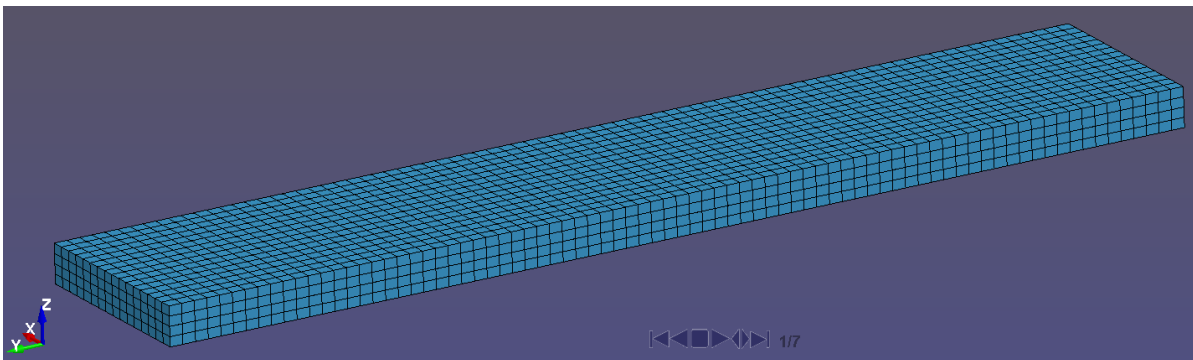


Figure 57. DCB Mesh 1-1 cohesive zone layer

An example of DCB Mesh 4 is shown in Figure 58. Other parameter specifications related to the simulations are shown in Table 27.

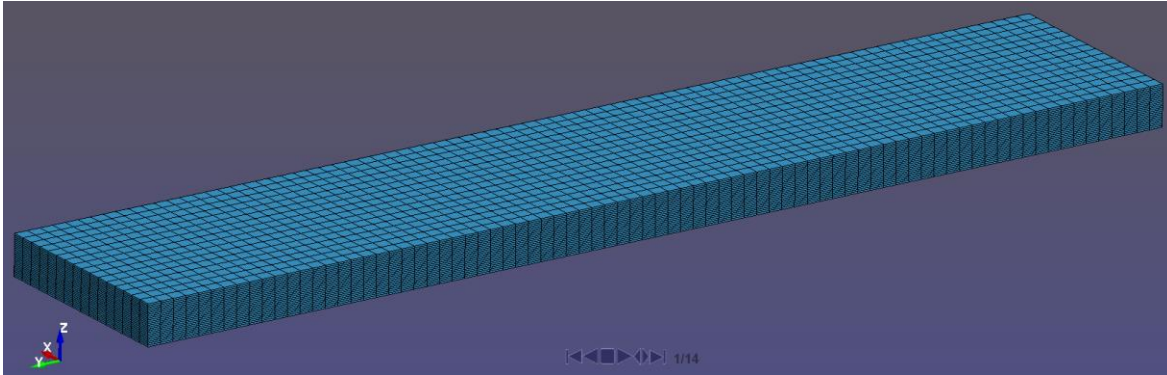


Figure 58. DCB Mesh 4 - 23 cohesive zone layers

Table 27. ENF and DCB simulation specifications

| Parameter | ENF | DCB |
|-------------------------------|---|---|
| Integration scheme | Elform = 2, fully integrated | Elform = 2, fully integrated |
| Hourglassing control | Incorporated, IHQ=6, QH=0.1 | Incorporated, IHQ=2, QH=0.1 |
| Mass scaling | Incorporated, TSSFAC = 0.9, DT2MS = -- 2.444(10) ⁻⁸ | Incorporated, TSSFAC = 0.9, DT2MS = -2.444(10) ⁻⁸ |
| Displacement-controlled input | 3 in/s | 5 in/s |
| Termination time | 0.05 s | 0.12 s |
| Platform | Linux, ASU Agave Cluster | Linux, ASU Agave Cluster |
| Material model of composite | MAT22 | MAT22 and MAT213 |
| MAT213 version | N/A | V1.3 α -1 |

MAT213 was used to model the composite material for the DCB test, not the ENF test, because of limitations in the current version of MAT213. An error in finding the value of the plastic multiplier occurs early in the ENF simulation with 23 cohesive zone layers using MAT213. Thus, only MAT22 was used to obtain simulation results for the ENF test. In simulations with only one cohesive zone layer, the plastic multiplier error did not occur. In these models, MAT213 showed that there was very little plasticity in the test coupon during the simulation, thus MAT22 was a valid choice of material model as it is a linear elastic model. Since MAT213 was unable to be used for the ENF simulation, the DCB simulation was completed using both MAT22 and MAT213 in different trials, to see how the change of material model affected the results. The MAT213 plastic multiplier error will be amended in the near future.

Sensitivity studies were conducted to determine the effect of changing each calibration parameter. A range of values was used across multiple simulations for each parameter while holding all other parameters constant. Using the force vs. displacement responses of the sensitivity study, values of the parameters were chosen that would produce the desired slope and peak force to match the experimental test values. The parameter values producing the best fit of the experimental slope and peak force were determined only by visual observation. However, the results of the sensitivity study will allow a regression analysis to be completed to find the optimal values; this procedure is part of the future work of this research.

5.5 Simulation results

5.5.1 ENF test

Sensitivity studies were carried out for the stiffness and peak traction mode II parameters. Figure 59 displays the results of the sensitivity study.

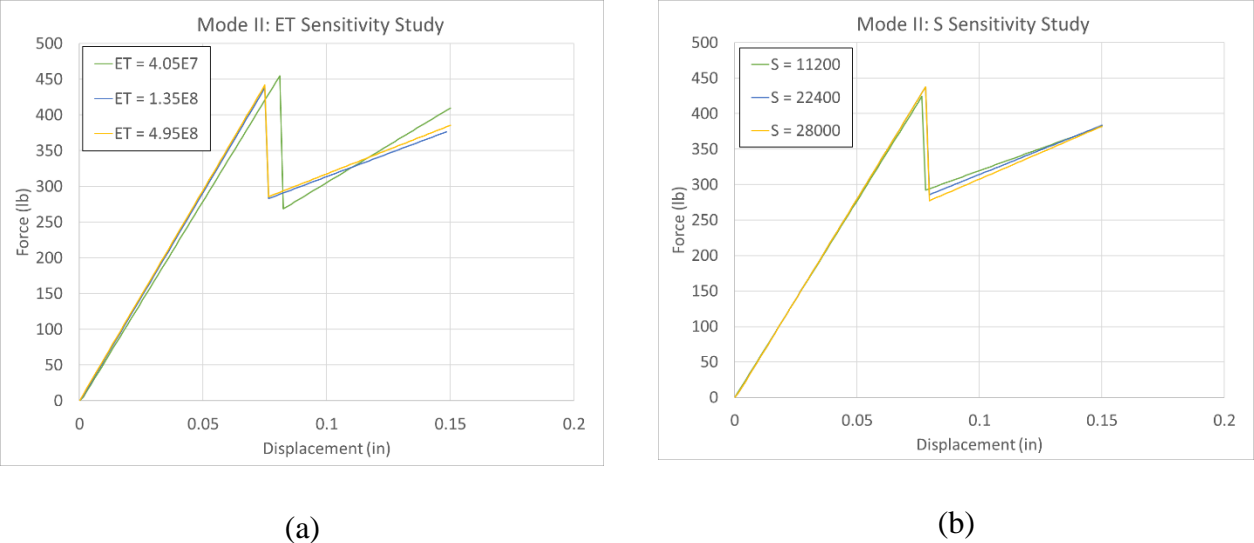


Figure 59. Mode II sensitivity study (a) ET (b) S

Figure 59(a) shows that a higher ET value led to a higher slope on the force displacement plot. Figure 59(b) shows that the peak force was increased with a larger S value. In addition, the larger values decreased the drop in force after the initial delamination.

Figure 60 shows the plot of force vs. displacement using the final parameter values. Due to limitations with the current implementation of MAT213, analysis errors inhibited modeling with

MAT213. MAT 22 was used for the solid elements in this model to complement the MAT 138 cohesive zone models.

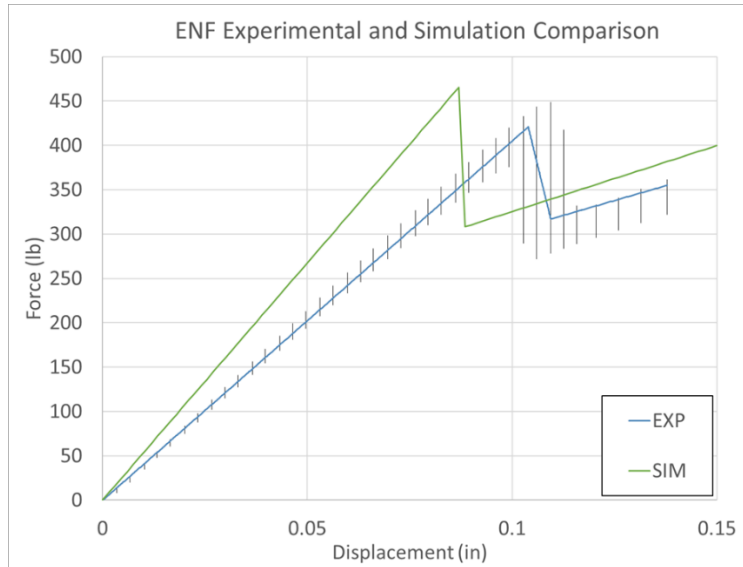


Figure 60. Force vs. displacement simulation and experimental comparison

This figure shows that the slope of the force displacement is higher for the simulation than the experiment. This is partly due to the use of MAT22. In general, models run with MAT213 yielded a lower slope. The simulation data was noisy and jagged, thus it was fit using polynomial regression. Table 28 lists the specifications of the regression.

Table 28. Simulation regression specifications

| Section | Fit Type | R ² |
|-----------|----------|----------------|
| Pre-peak | Linear | 0.997 |
| Post-peak | Linear | 0.226 |

The final MAT 138 values for mode II are shown in Table 29.

Table 29. Final Mode II MAT 138 parameters

| Parameter | Value |
|-----------|------------------------------|
| ET | 4.50(10) ⁷ psi/in |
| S | 28000 psi |
| GIIC | 10.50 lb-in/in ² |

Figure 61 depicts the traction separation curve produced by these final parameter values.

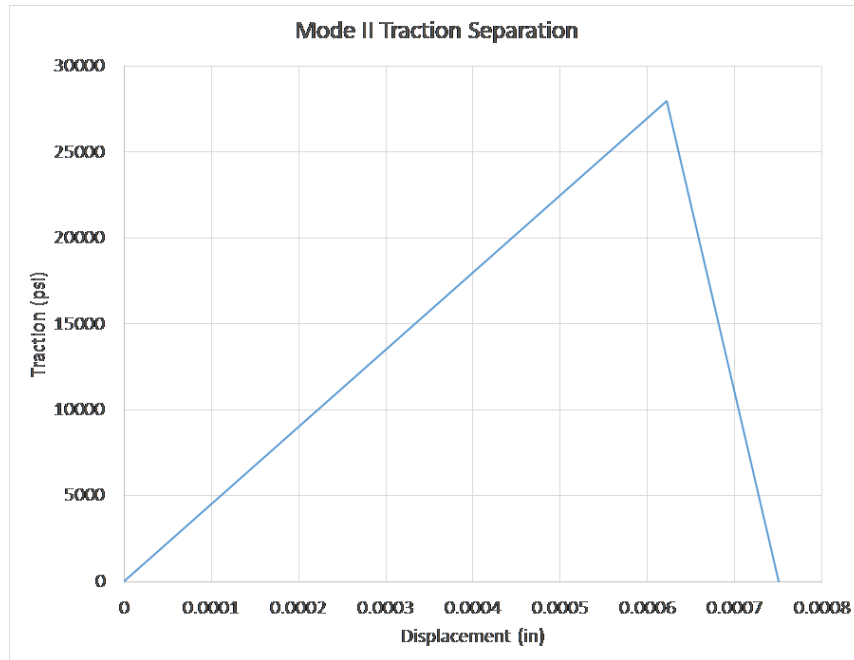


Figure 61. Mode II final traction separation curve

5.5.2 DCB test

Sensitivity studies were also carried out for the stiffness and peak traction mode I parameters. Figure 62 shows the results of the sensitivity study.

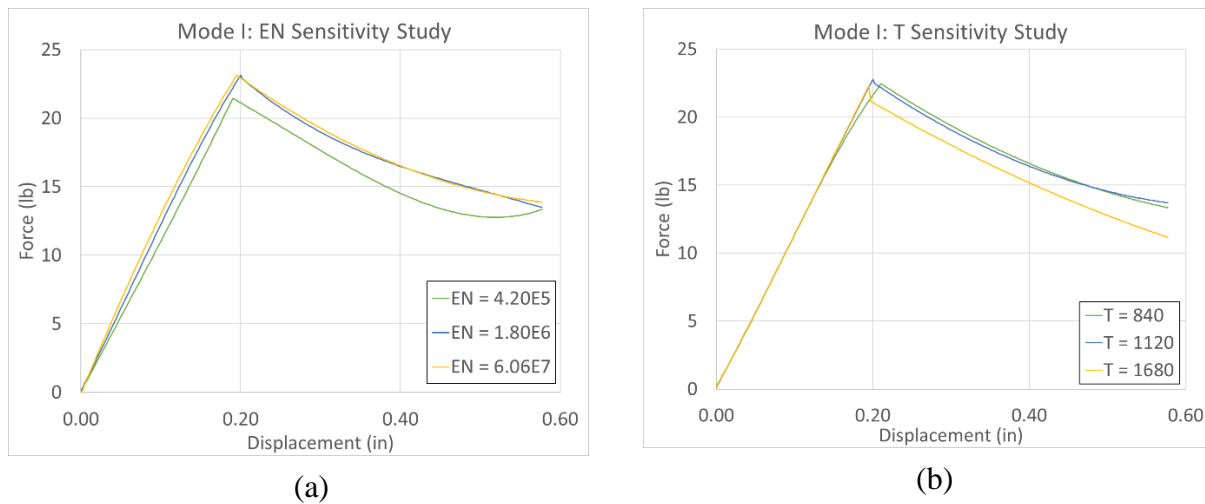


Figure 62. Mode II sensitivity study (a) ET (b) S

Figure 62 shows that a higher EN value led to a higher slope on the force displacement plot. The figure also shows that the peak force increased slightly with a larger T value.

Optimal values for each cohesive zone parameter determined from the sensitivity study used a trial-and-error process. Figure 63 shows the plot of force vs. displacement using the final MAT138 values and using MAT213 to model the solid elements.

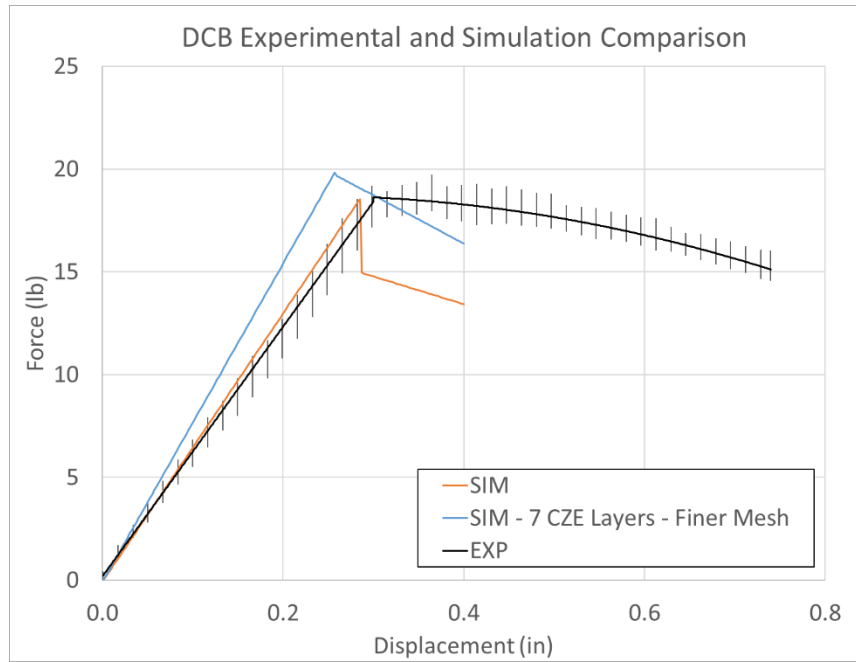


Figure 63. Force vs. displacement simulation and experimental comparison

In Figure 63, the curve labeled “SIM” was the result of the final model with 23 cohesive zone layers. The pre-peak response is within the experimental data range. However, there is a drop in the force after the linear peak force value that is not present in the experimental data. This drop in force was discovered to be a function of element size. The model with 23 cohesive zone layers was used with a coarse mesh to decrease simulation run time. A preliminary model with seven cohesive zone layers but a finer mesh produced results that did not feature this drop. The results of this model are labeled “SIM – 7 CZE Layers – Finer Mesh” in Figure 63. Thus, the element size was the cause of the discrepancy in the change in force at the beginning of crack propagation. Future work on the DCB model includes finding a balance between computational time and model performance. The simulation curve was noisy and jagged and thus was fit using polynomial regression. Table 30. Simulation regression specifications shows the specifications of the regression.

Table 30. Simulation regression specifications

| Section | Fit Type | R ² |
|-----------|----------|----------------|
| Pre-peak | Linear | 0.997 |
| Post-peak | Linear | 0.033 |

The final MAT 138 values for mode I are shown in Table 31. Final Mode I MAT 138 parameters.

Table 31. Final Mode I MAT 138 parameters

| Parameter | Value |
|-----------|------------------------------|
| EN | 6.00(10) ⁵ psi/in |
| T | 1400 psi |
| GIC | 2.65 psi-in |

Figure 64 shows the traction separation curve produced by these final parameters values.

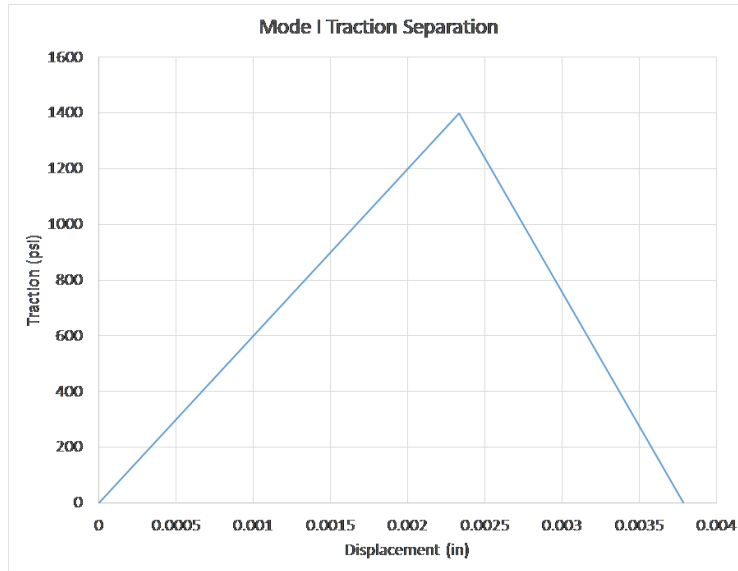


Figure 64. Mode I final traction separation curve

Using the parameter values found through experimentation and simulation calibration, the final MAT138 input deck, used for the cohesive zone layers in the stacked-ply simulations, is shown in Table 32. The values use base units of pounds and inches.

Table 32. MAT138 input deck

| | | | | | | | | |
|----------|-----|-----------------------|-------|---------|-----------------------|-----------------------|------|-------|
| Card 1 | 1 | 2 | 3 | 4 | 5 | 6 | 7 | 8 |
| Variable | MID | RO | ROFLG | INTFAIL | EN | ET | GIC | GIIC |
| Value | | 8.5(10) ⁻⁸ | | 1 | 6.00(10) ⁵ | 4.50(10) ⁷ | 2.65 | 10.50 |
| Card 2 | 1 | 2 | 3 | 4 | 5 | 6 | 7 | 8 |
| Variable | XMU | T | S | UND | UTD | GAMMA | | |
| Value | 1.0 | 1400 | 28000 | | | | | |

6 LS-DYNA simulation of QS-RT stacked-ply validation tests using MAT213

6.1 LS-DYNA simulation overview

This section summarizes the stacked-ply simulations conducted as a portion of the validation testing for the MAT213 material model [MAT213 V1.3-alpha Rev # 123494].

Four types of stacked-ply simulations were performed to mirror the experimental tests - tension, compression, tension with stress concentration, and compression with stress concentration. These simulations serve to validate MAT213's deformation and damage sub-models.

Simulations of the stacked-ply validation tests were conducted using MAT213 to compare with the experimental tests. The modeling techniques and validation metrics used varied according to the test and are explained in the following sections.

In this section, the experimental results are presented as model experimental curves. The model curves were obtained by averaging the results of the test replicates for the respective stacked-ply tests. The stresses, strains, and displacements were averaged over the time duration of the experiments. The experimental data is also presented as a whisker curve, where the extents of the whisker depict the experimental data range.

6.2 General modeling techniques

The goal while modeling the stacked-ply tests was to recreate the conditions of the experimental tests as accurately as possible while maintaining computational efficiency. Because of a lack of symmetry in the test coupons due to the ply layup, a full model of each test was created. All eight layers of the test coupons were modeled for the entire gage section of each test. An example of the XZ plane view of the model, showing all eight plies, is shown for a coarse mesh in Figure 65.

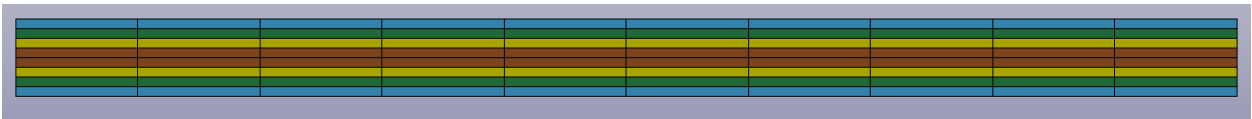


Figure 65. Elevation XZ plane view of the FE model

Convergence analysis conducted for each simulation used three meshes with decreasing element size and aspect ratio. Other parameters shared by all the models are listed in Table 33.

Table 33. Model parameter specification

| Parameter | Specification |
|---------------------------------------|---|
| Integration scheme | Elform = 2, fully integrated |
| Hourglassing control | Incorporated, IHQ=2, QH=0.1 |
| Mass scaling | Incorporated, TSSFAC = 0.7, DT2MS = $-7.1429(10)^{-8}$ |
| Displacement-controlled input | Varying, made equal to the displacement obtained from DIC extensometer |
| Termination time | Varying |
| Platform | Linux, ASU Agave Cluster |
| Material model for composite material | MAT213 |
| Material model for cohesive zone | MAT138 |
| MAT213 version | V1.3 α -1 |
| Damage model of MAT213 | Only uncoupled 2-direction compression and uncoupled 12-plane shear are included. |
| Failure model of MAT213 | Not incorporated |

The extension of the specimen in the y direction was measured in the experimental test using a digital extensometer within Vic 3D software. This displacement vs. time plot was averaged over all of the experimental tests and then smoothed. The time values were scaled by a factor of 1/100,000 to create the final displacement vs. time plot for the displacement-controlled nodes in the simulation. The time scaling was necessary to allow a reasonable computational time within LS-DYNA. During post-processing, the time values were re-scaled by a factor of 100,000 to allow for comparison with the experimental results. For example, the average experimental test duration for the tension tests was 320 seconds, thus the simulation time was 0.00320 seconds. This time-scaling procedure was used for each of the test types. To validate the use of time scaling, it was necessary to examine the energy effects of each simulation. An example of the energy induced in the simulation of the tension test is shown in Figure 66.

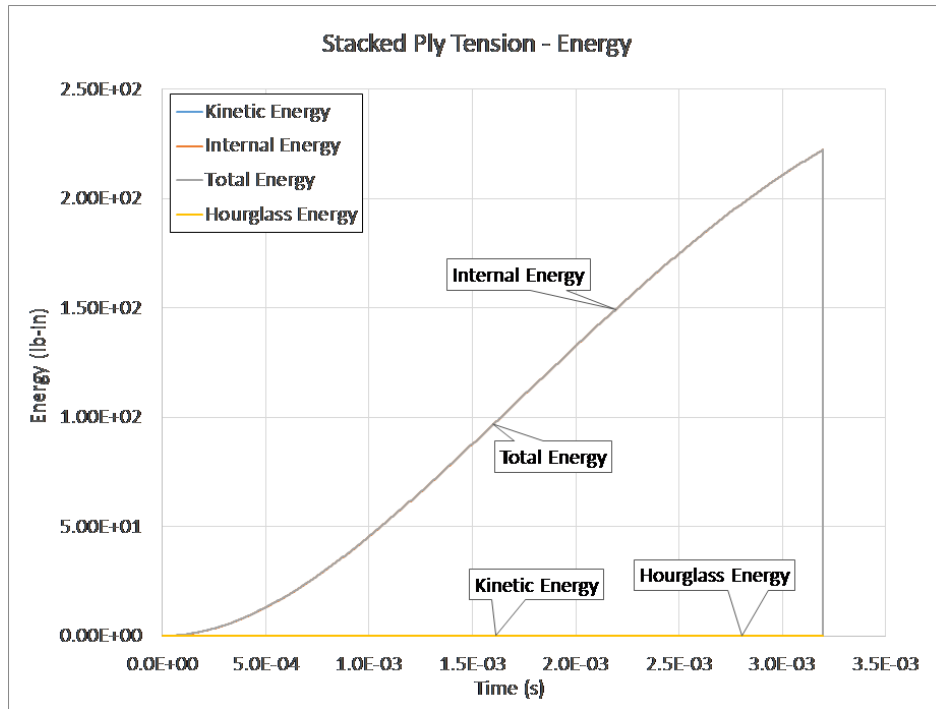


Figure 66. Energy plot for tension simulation

For each simulation, energy plots were observed to verify that the kinetic energy remained a small portion of the total energy, as is the case in Figure 66. The same energy checks were used in this study as employed by Deivanayagam et al. (Deivanayagam, Vaidya, & Rajan, 2014) in a study on dry fabric modeling.

For each validation test, three meshes were created with decreasing element size. Simulations were run with the coarse, medium, and fine meshes to show convergence of the results with decreasing element size. Only results from the fine meshes are shown.

Data extracted from the simulations was often jagged and choppy. In order to make meaningful comparisons between the experimental and simulated data, the simulated data was smoothed via polynomial regression fitting. The details of each polynomial fit are given in the following sections.

The interlaminar layers of the test coupons were modeled using material model MAT138. The parameters of the model were the final parameters obtained from the ENF and DCB test delamination studies as shown in Table 31.

Subsequent sections detail the specific modeling techniques of each test.

6.3 LS-DYNA simulation of stacked-ply tension

6.3.1 Simulation modeling

The overall geometry as well as boundary and loading conditions of the experimental test are shown in Figure 67 and Figure 68. Only the gage section of the specimen is shown.

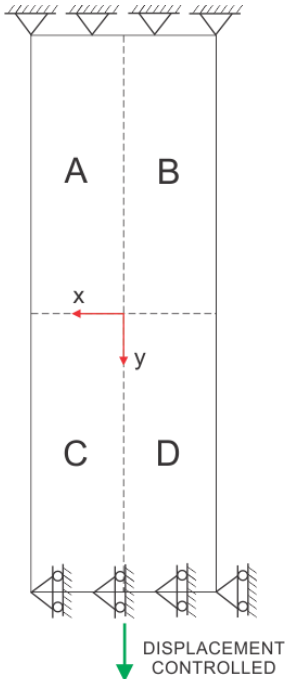


Figure 67. Experimental test conditions, XY plane

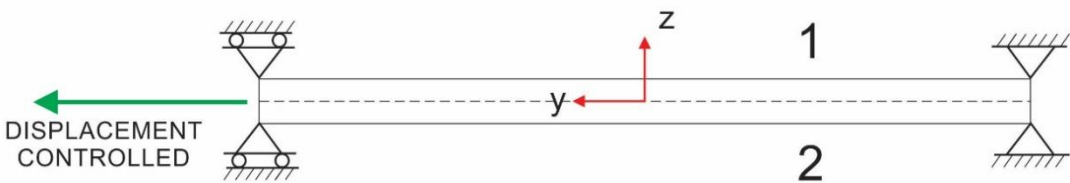


Figure 68. Experimental test conditions, YZ plane

The geometry as well as boundary and loading conditions for the MAT213 simulations are shown in Figure 69 and Figure 70.

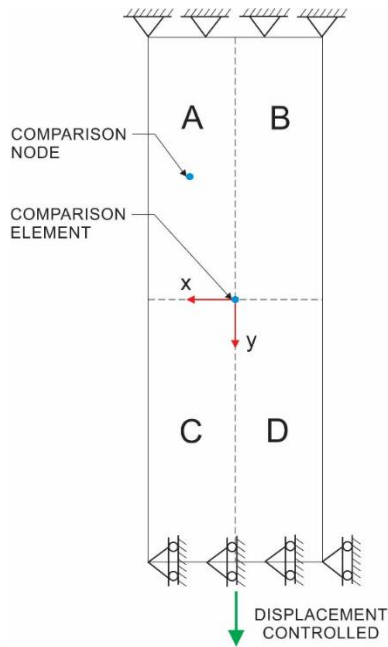


Figure 69. Simulation test conditions, XY plane

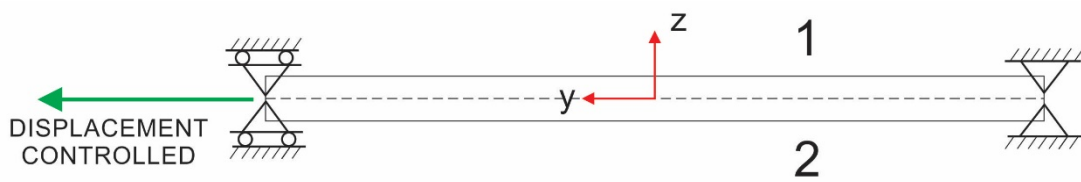
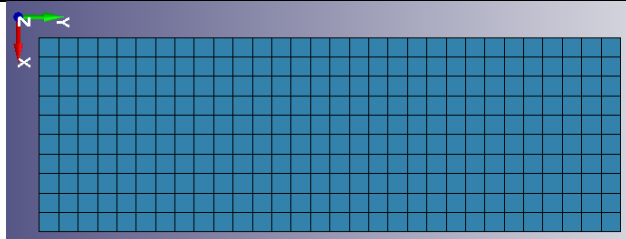
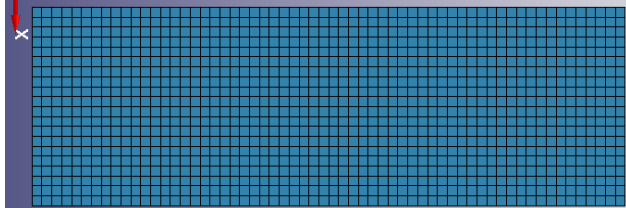
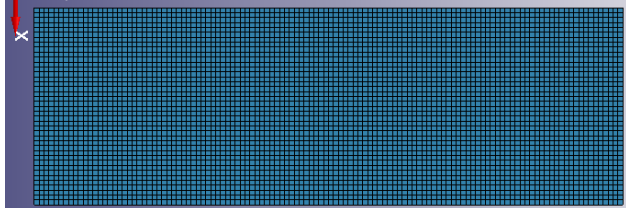


Figure 70. Simulation test conditions, YZ plane

Three finite element (FE) models were created with varying element sizes; these are depicted in Table 34. The plies were modeled using MAT213. The interface between each ply was modeled using cohesive zone elements. The cohesive elements were modeled using MAT138.

Table 34. FE model meshes

| Mesh | # of MAT213 elements | # of cohesive elements | XY Plane view of FE model |
|--------|----------------------|------------------------|---|
| Coarse | 2400 | 2100 |  |
| Medium | 9600 | 8400 |  |
| Fine | 38400 | 33600 |  |

6.3.2 Validation metrics

The simulation tests were validated with three distinct metrics comparing the simulation and experimental values. These metrics are outlined in Table 35.

Table 35. Validation metrics description

| Metric | Description |
|--------|--|
| 1 | Comparison of strains for the 0 ⁰ -ply of an element, which was centrally located in the simulation model (Figure 69). The strains ϵ_{xx} and ϵ_{yy} were plotted against time. |
| 2 | Comparison of displacement for the 0 ⁰ -ply of a node, which was centrally located in Quadrant A of the simulation model (Figure 69). The x and y displacements were plotted against time. |
| 3 | Comparison of the average (longitudinal) stress in the Y direction, σ_{yy} , plotted against the (longitudinal) strain in the Y direction, ϵ_{yy} . |

A comparison of how the data was captured in the experimental and simulation tests for Metric 1 is shown in Table 36.

Table 36. Tension test metric 1

| Data Type | Method of Data Collection |
|--------------|--|
| Experimental | Strains were computed using a DIC strain gage section as shown in Figure 70 |
| Simulation | Strains were taken from an element that was located centrally in the gage section of the 0 ⁰ -ply as shown in Figure 69 |

A comparison of how the data was captured in the experimental and simulation tests for Metric 2 is shown in Table 37.

Table 37. Tension test metric 2

| Data Type | Method of Data Collection |
|--------------|--|
| Experimental | Displacements were calculated using virtual extensometers with DIC. The y displacement was calculated using an extensometer that extends in the Y direction from the fixed end to the point of interest. The x displacement was calculated using an extensometer that extends in the X direction from the specimen centerline to the point of interest. These digital extensometers are shown in Figure 71 |
| Simulation | Displacements were taken from a node that was located centrally in quadrant A of the 0 ⁰ -ply, as shown in Figure 69. |

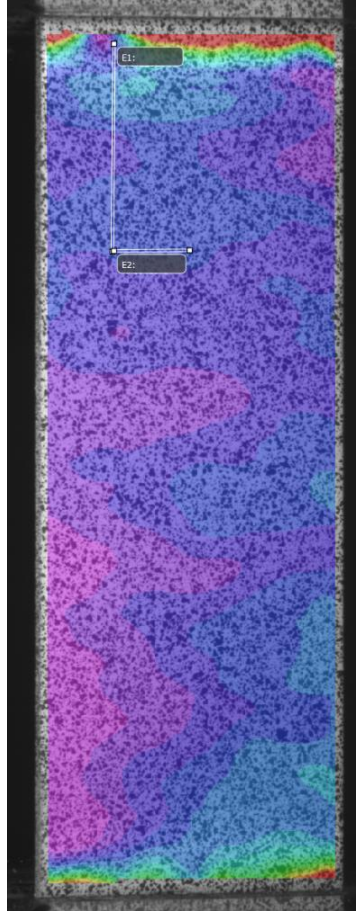


Figure 71. VIC 3D digital extensometers used for metric 2

Metric 3

A comparison of how the data was captured in the experimental and simulation tests for Metric 3 is shown in Table 38.

Table 38. Tension test metric 3

| Data Type | Method of Data Collection |
|------------------|--|
| Experimental | The experimental data for σ_{yy} was obtained using equation (1). The strain value was the same ϵ_{yy} used for metric 1. The force used to obtain the stress was the force recorded from the MTS test machine |
| Simulation | The simulation data for σ_{yy} was obtained by recording and taking the summation of the Y force for every node that was restrained in the Y direction. The forces were summed and divided by the original area of model in the XZ plane. The simulation data for ϵ_{yy} was the same which was used for metric 1. The nodes used to compute the force are shown in Figure 72. |

The nodes used to obtain the reactions the Y direction for the simulation are shown in Figure 72.

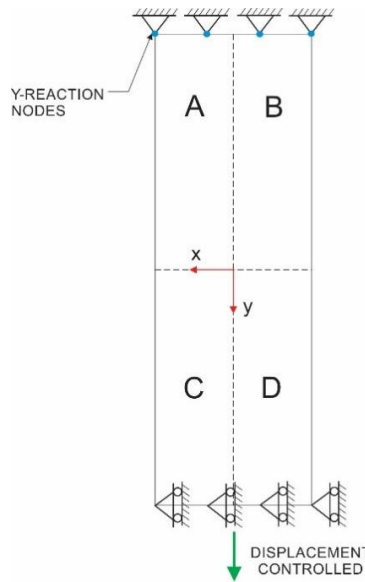


Figure 72. Metric 3 y-reaction nodes

6.3.3 Results

Figure 73 and Figure 74 show the results for Metric 1.

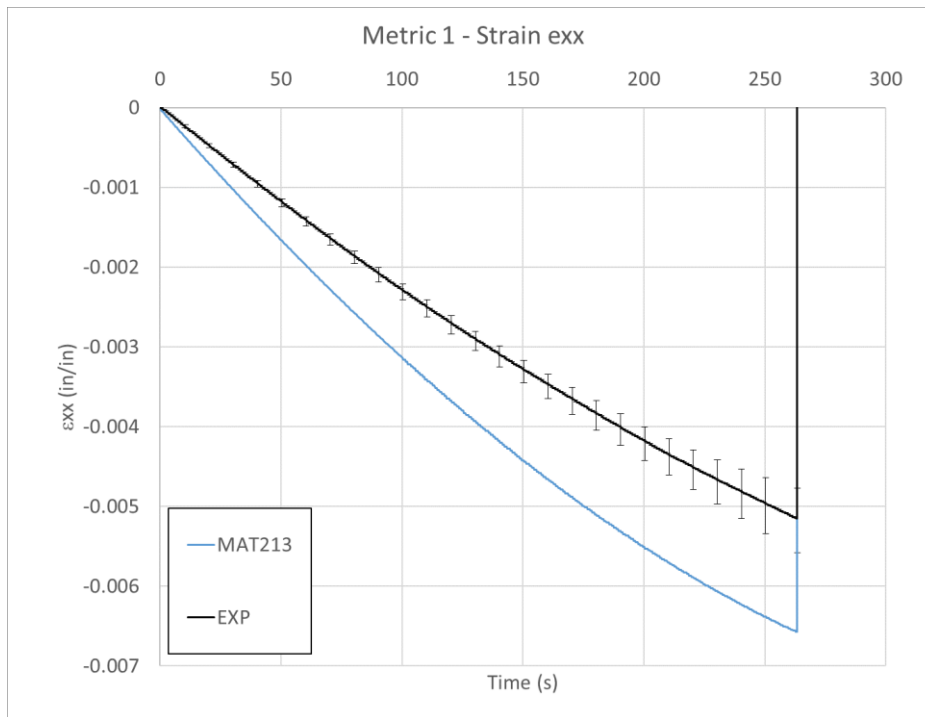


Figure 73. Metric 1 - ϵ_{xx} comparison

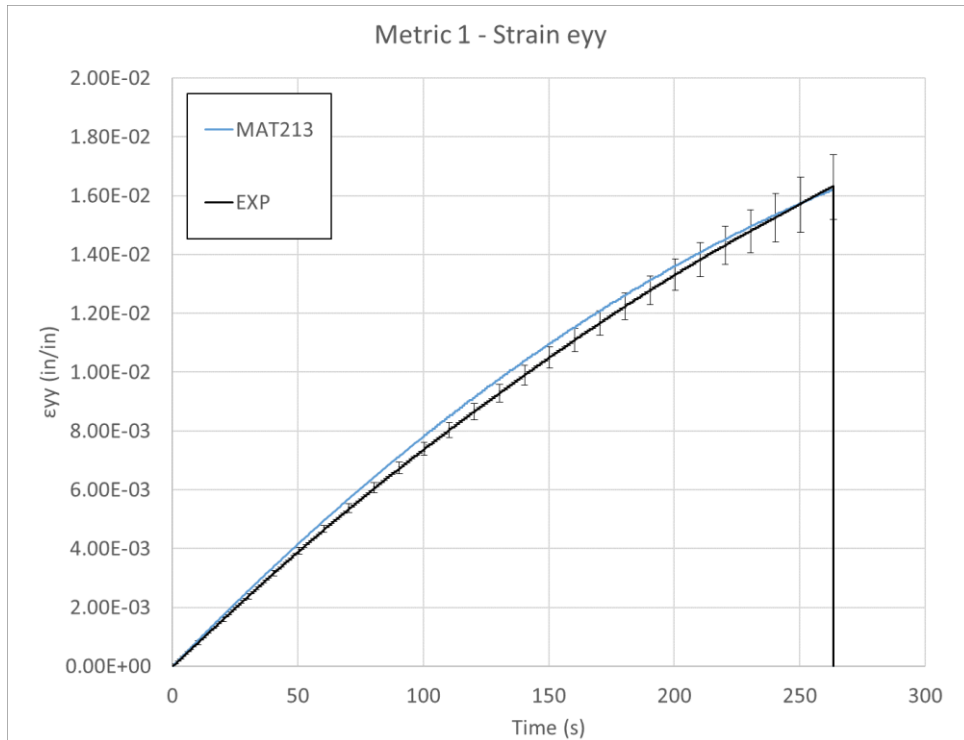


Figure 74. Metric 1 - ϵ_{yy} comparison

Figure 75 and Figure 76 show the results for Metric 2.

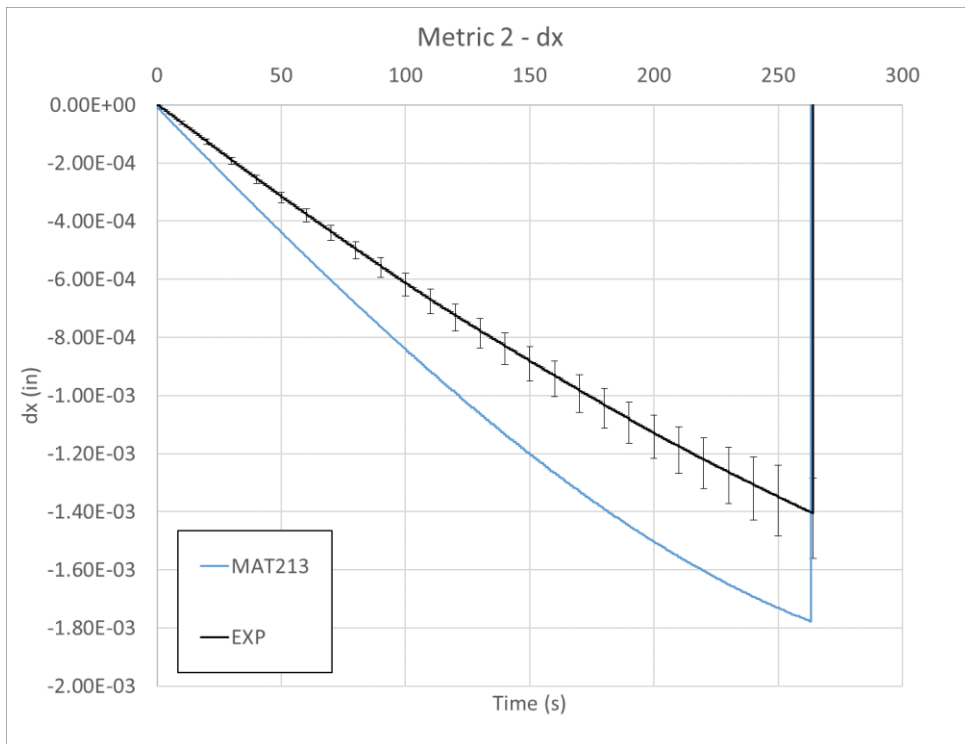


Figure 75. Metric 2 - x-displacement comparison

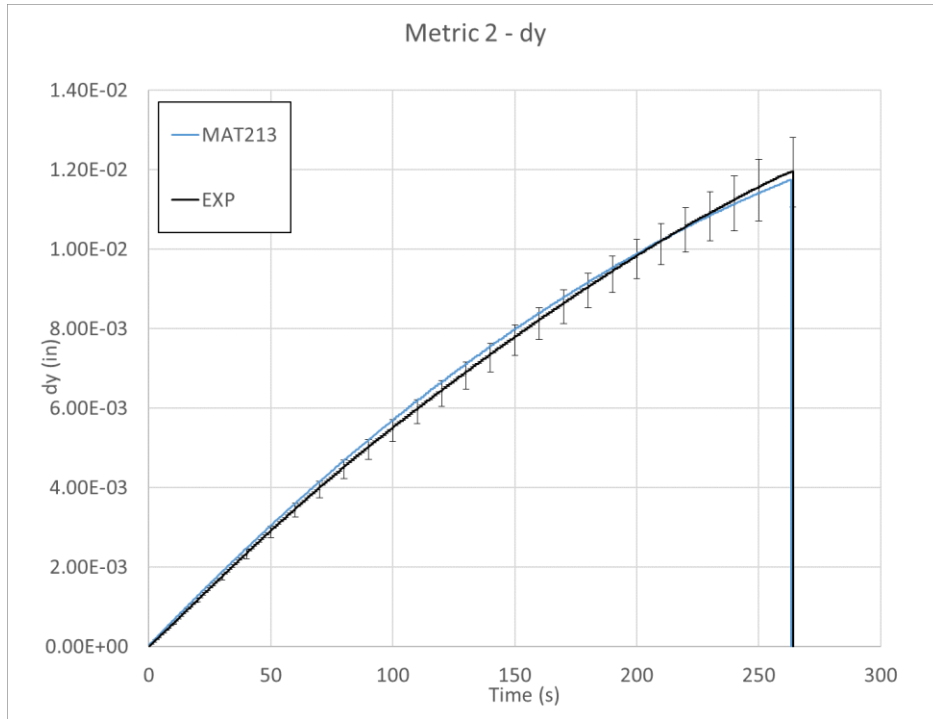


Figure 76. Metric 2 - y-displacement comparison

Figure 77 shows the results for Metric 3.

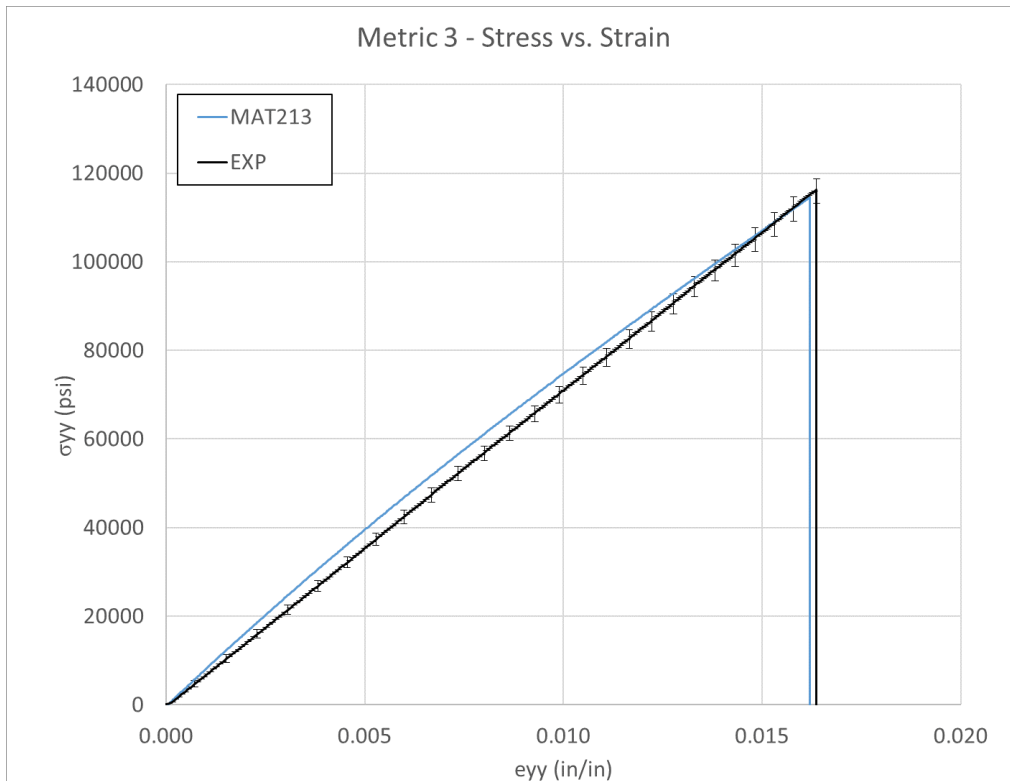
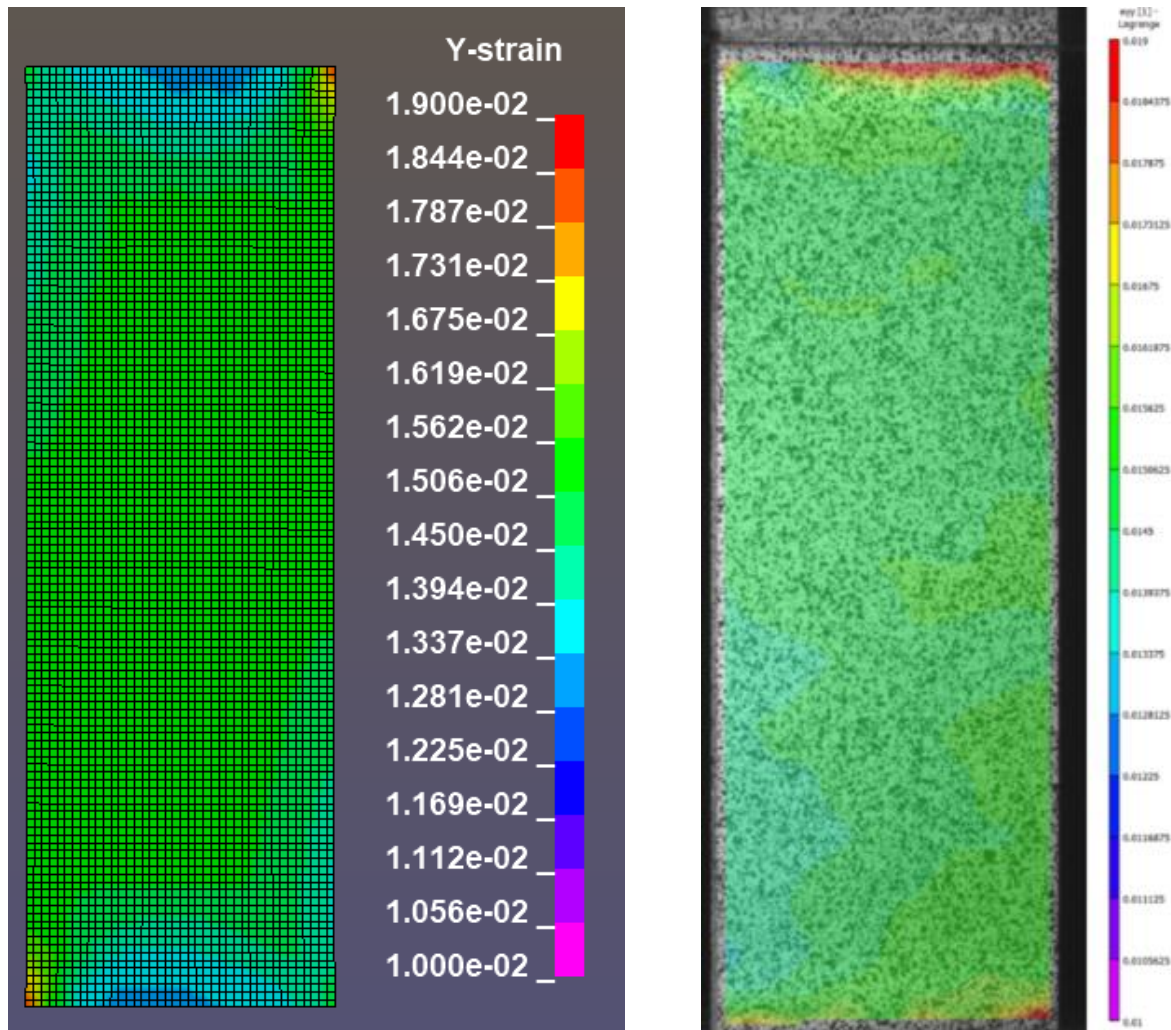


Figure 77. Metric 3 - stress-strain comparison

A fringe plot of the y-strain is pictured in Figure 78. The range and color scheme depicting the strain field is identical for the simulation (a) and the experiment (b). The experimental plot shows a higher strain along the right edge of the test coupon. However, the range of strain magnitude and the average strain value in the gage section match well.



(a) (b)
Figure 78. Y-Strain fringe plot of tension test, at $t = 250$ s (a) Simulation (b) Experiment

6.3.4 Discussion

Several of the simulation curves used for comparison had data that was fitted using polynomial regression. The details of the polynomial regressions are shown in Table 39.

Table 39. Polynomial regression fitting of tension simulation metrics

| Metric | Order of polynomial regression | R-squared of regression | Fig. # |
|-----------------------------------|---------------------------------------|--------------------------------|---------------|
| Metric 1 – Strain ϵ_{xx} | Cubic | 0.9998 | Figure 73 |
| Metric 1- Strain ϵ_{yy} | Cubic | 0.9998 | Figure 74 |
| Metric 2 - dx | Cubic | 0.9995 | Figure 75 |
| Metric 2 – dy | Cubic | 0.9998 | Figure 76 |
| Metric 3 – Stress-Strain | Quadratic | 0.9991 | Figure 77 |

Metric 1 indicated that the MAT213 simulation over-predicted the transverse strain, while giving an excellent prediction of the longitudinal strain. The longitudinal strain was in this case, nearly a magnitude of order larger than the transverse strain, thus MAT213 better predicted the larger strain value.

Metric 2 indicated that the MAT213 simulation over predicted the transverse displacement measure in the experiment, while it has a good prediction of the longitudinal displacement. The MAT213 simulation showed nonlinearity in the transverse displacement response towards the end of the simulation, which was present in some but not all of the experimental tests.

Metric 3 indicated that the MAT213 simulation displayed some nonlinearity in the stress-strain response, while the experimental tests showed only linear relationships. The MAT213 response is slightly stiffer than the experimental results initially, the stiffness is reduced during the test and the final stress value is very similar to that of the experimental tests.

The transverse direction strains and displacements are approximately one magnitude of order lower than those in the longitudinal direction. The error seen in the transverse direction metrics may be due to this low magnitude and the limitations of the DIC software in capturing these small displacements and strains.

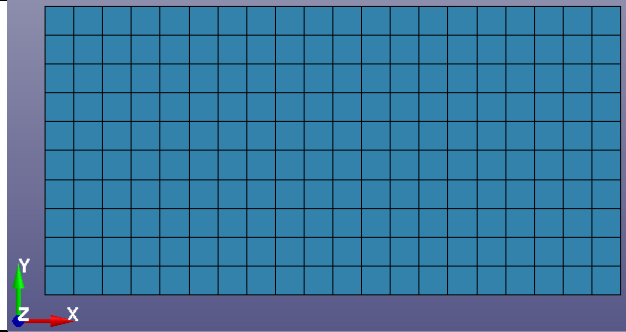
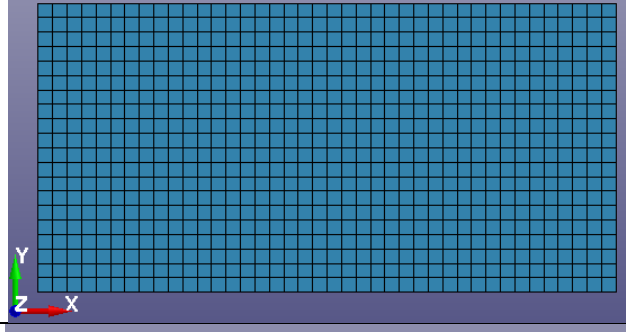
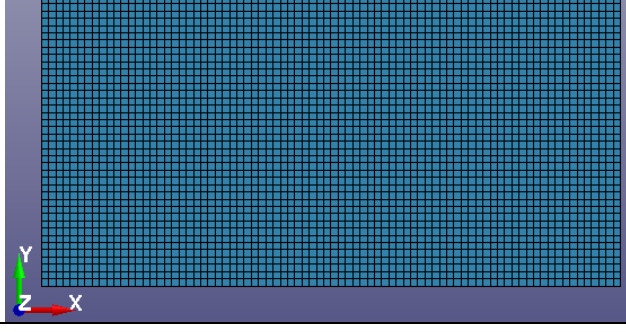
6.4 LS-DYNA simulation of stacked-ply compression

6.4.1 Simulation modeling

Only the gage area of the experimental test was considered for the simulations. Thus, the experimental and simulation modeling and fixity conditions was the same as for the stacked-ply tension tests. The dimensions of gage area were different, but the overall geometry was the same.

Three finite element (FE) models were created with varying element sizes; these are depicted in Table 40.

Table 40. FE model meshes

| Mesh | # of MAT213 elements | # of cohesive elements | XY Plane view of FE model |
|--------|----------------------|------------------------|--|
| Coarse | 1600 | 1400 |  The image shows a coarse finite element mesh in the XY plane. The mesh is a rectangular grid of blue elements. A coordinate system is shown at the bottom left with the Y-axis pointing up, the X-axis pointing right, and the Z-axis pointing out of the page. The mesh is composed of approximately 16 columns and 10 rows of elements. |
| Medium | 6400 | 5600 |  The image shows a medium finite element mesh in the XY plane. The mesh is a rectangular grid of blue elements. A coordinate system is shown at the bottom left with the Y-axis pointing up, the X-axis pointing right, and the Z-axis pointing out of the page. The mesh is composed of approximately 32 columns and 20 rows of elements. |
| Fine | 25600 | 22400 |  The image shows a fine finite element mesh in the XY plane. The mesh is a rectangular grid of blue elements. A coordinate system is shown at the bottom left with the Y-axis pointing up, the X-axis pointing right, and the Z-axis pointing out of the page. The mesh is composed of approximately 64 columns and 40 rows of elements. |

6.4.2 Validation metrics

The validation metrics and data collection methods were the same as for the stacked-ply tension tests except for a minor change in the evaluation of metric 2. Since the compression specimen has a shorter gage section and failed earlier than the tension specimen failed, the displacements to induce failure were small. Thus, the node chosen to compare displacement was in the center of the gage section in the y-direction. This gives a higher displacement than the position of the node in the tension comparison. The higher displacement resulted in lower error from experimental data collection. The location of the comparison node for metric 2 and the comparison element for metric 1 are shown in Figure 79.

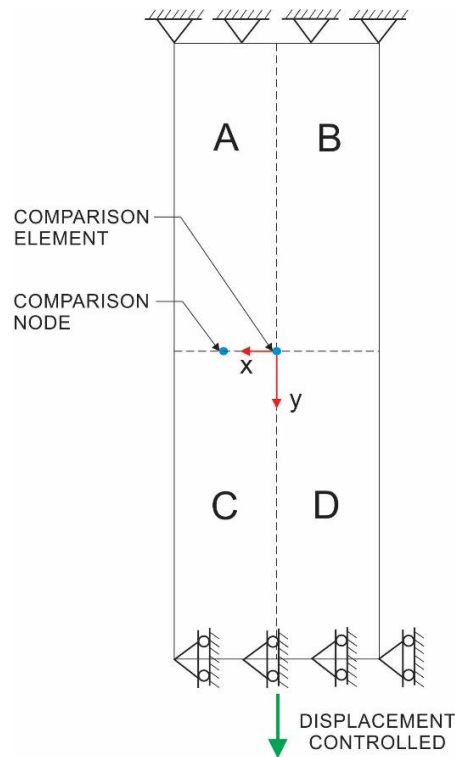


Figure 79. Compression comparison node and element

6.4.3 Results

Figure 80 and Figure 81 show the results for Metric 1. Figure 82 and Figure 83 show the results for Metric 2. Figure 84 shows the results for Metric 3.

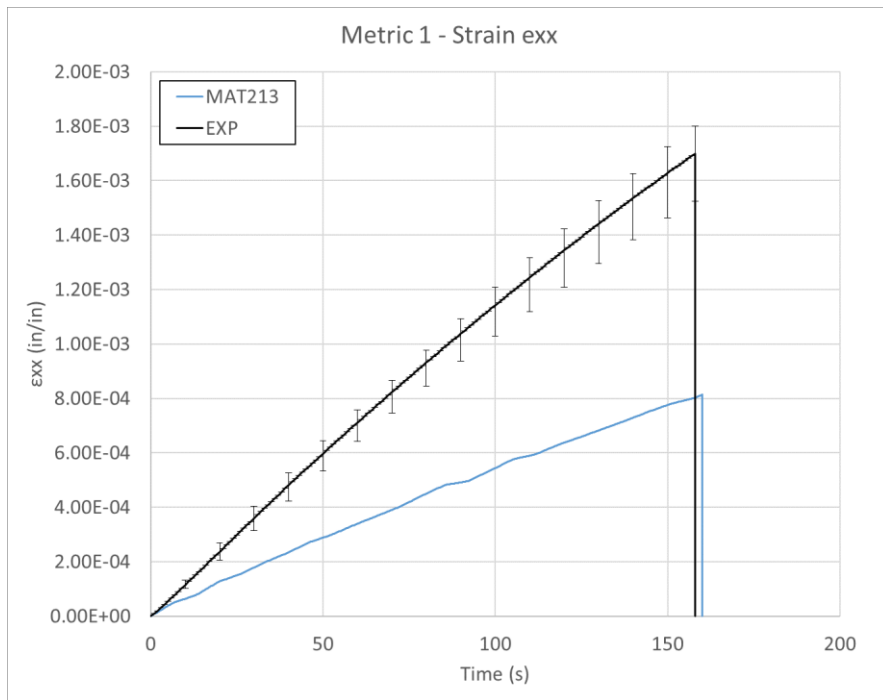


Figure 80. Metric 1 - ϵ_{xx} comparison

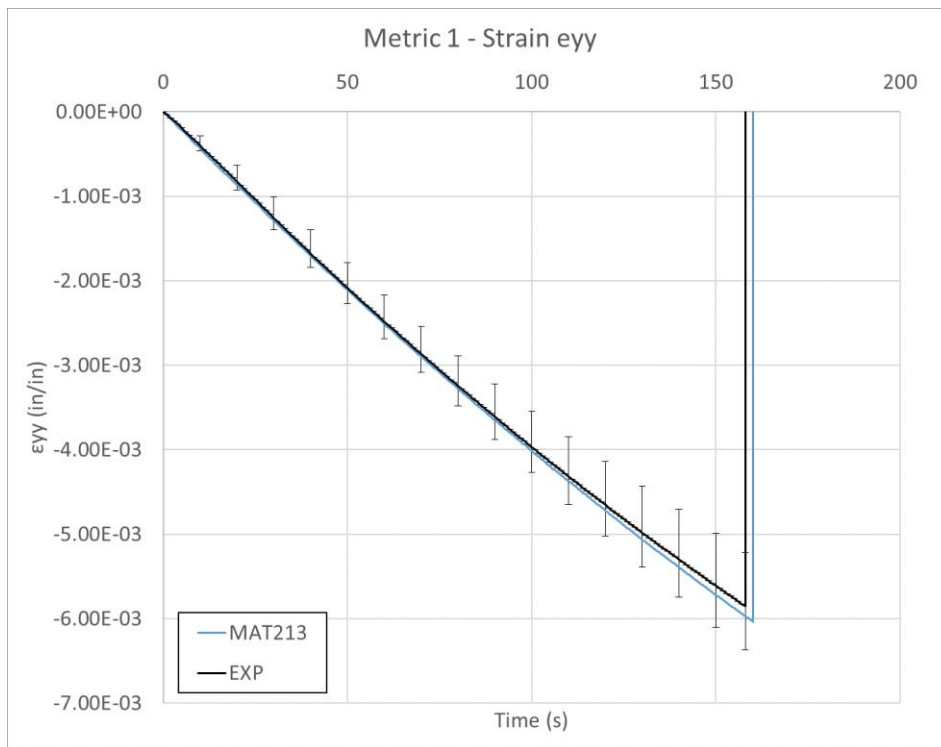


Figure 81. Metric 1 - ϵ_{yy} comparison

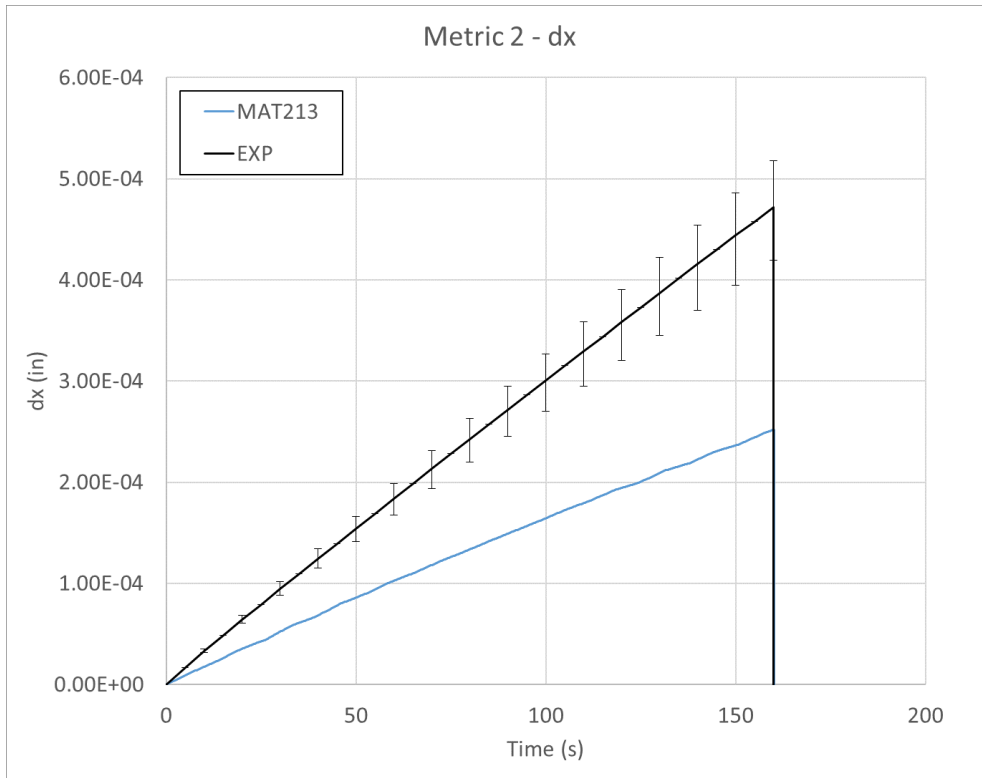


Figure 82. Metric 2 - x-displacement comparison

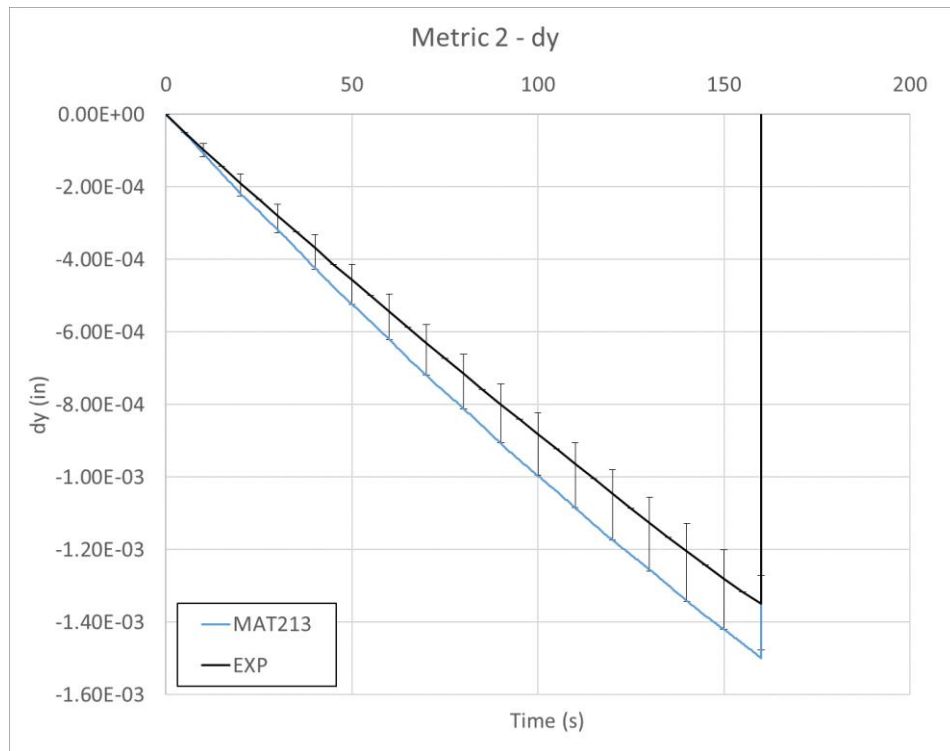


Figure 83. Metric 2 - y-displacement comparison

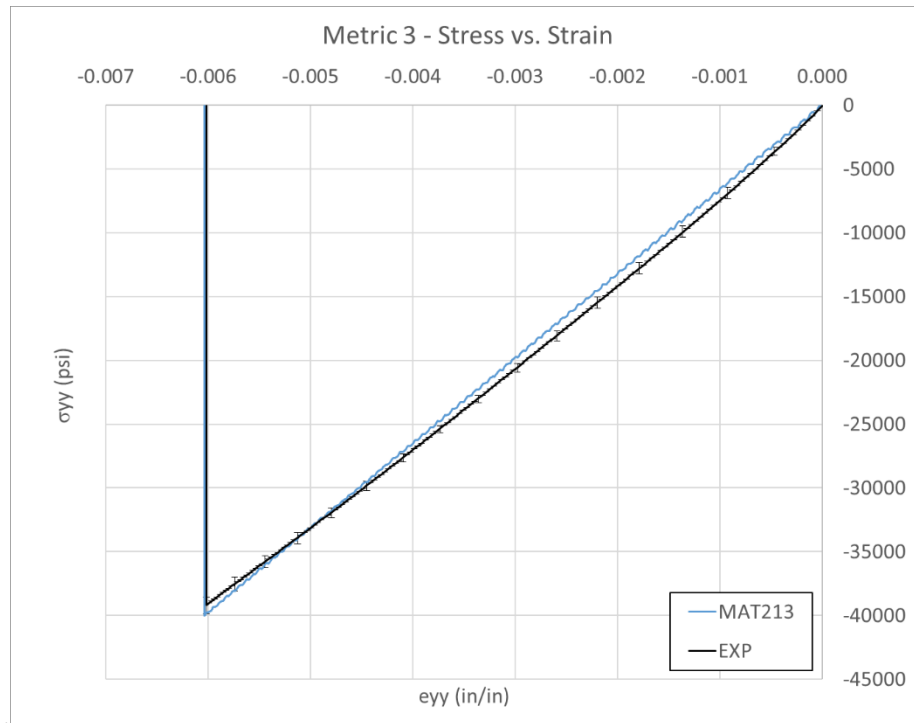
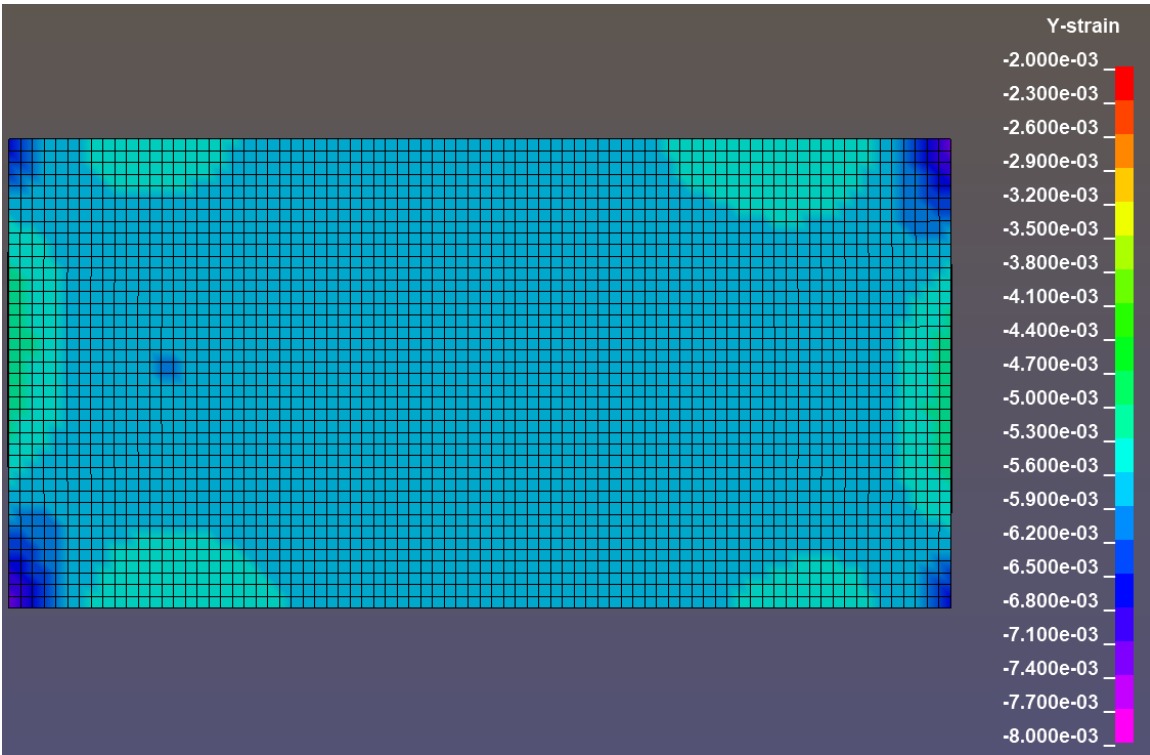
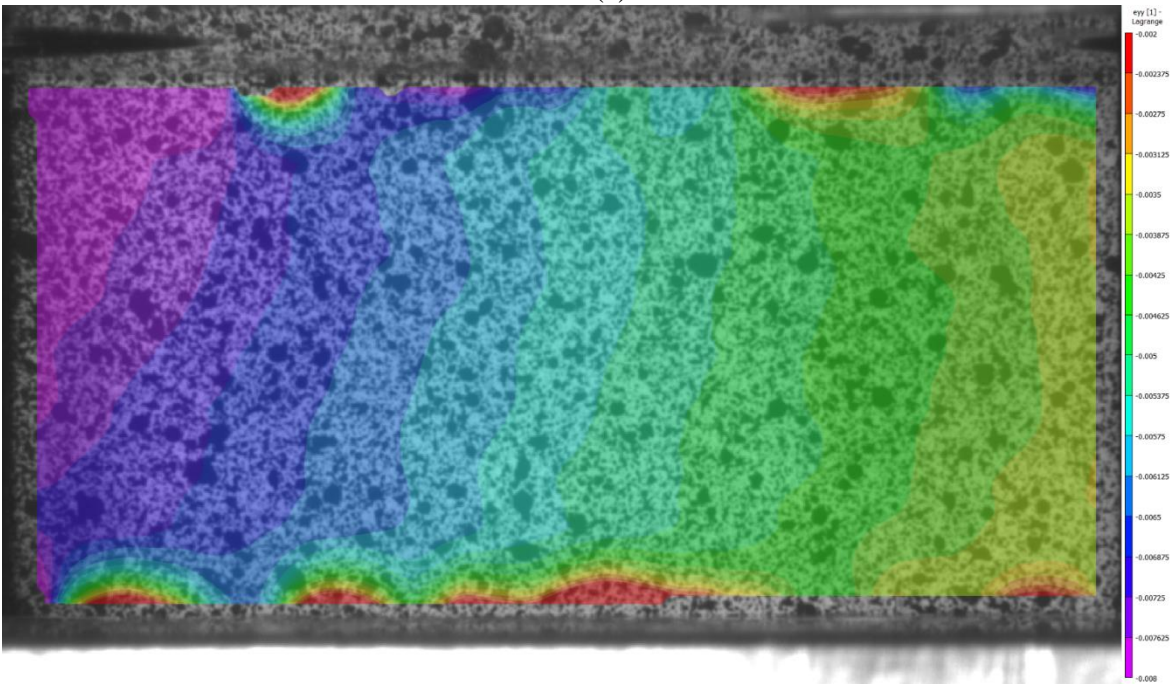


Figure 84. Metric 3 - stress-strain comparison

A fringe plot of the y-strain is pictured in Figure 85. The range and color scheme depicting the strain field is identical for the simulation (a) and the experiment (b). The experimental plot shows a gradation from high magnitude to low strain from the right to left edge. However, the experimental value at the center of the coupon is the same as that in the majority of the section of the simulation.



(a)



(b)

Figure 85. Y-Strain fringe plot of compression test, at $t = 150$ s (a) Simulation (b) Experiment

Observation of the gradation shown in the strain field shows that some factor of the experiments caused an asymmetry in the loading condition. Given the desired loading condition and experimental geometry, the strain field should be symmetric about the vertical axis. A possible cause of asymmetry in the loading is eccentricity caused by the load frame or by the CLC fixture.

6.4.4 Discussion

Metric 1 indicated that the MAT213 simulation under-predicted the transverse strain by approximately one half of the experimental results, while the longitudinal strain was well predicted, in the range of the experimental results.

Metric 2 indicated that the MAT213 simulation had a similar performance in predicting the transverse and longitudinal displacement as measured in the experimental tests. The transverse displacement is under-predicted by the simulation, nearly by one-half, while the longitudinal displacement is within the experimental results.

Metric 3 indicated that the MAT213 simulation well predicted the stiffness shown in the experimental results very well. The stress-strain curve extends beyond that of the experimental curves, but the stiffness is within the range of the experimental results for the duration of the experimental tests.

The error seen in the transverse direction metrics for the compression tests could be related to the asymmetry seen in the strain fields.

6.5 LS-DYNA simulation of stacked-ply tension – stress concentration test

6.5.1 Simulation modeling

The overall geometry as well as boundary and loading conditions for the experimental setup are shown in Figure 86 and Figure 87.

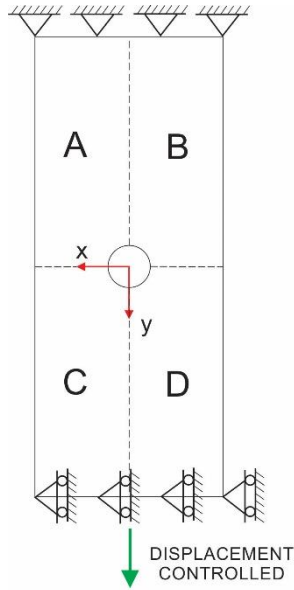


Figure 86. Experimental test conditions, XY plane

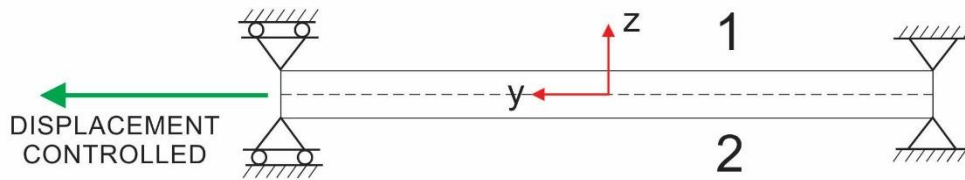


Figure 87. Experimental test conditions, YZ plane

The geometry as well as boundary and loading conditions for the MAT213 simulations are shown in Figure 88 and Figure 89.

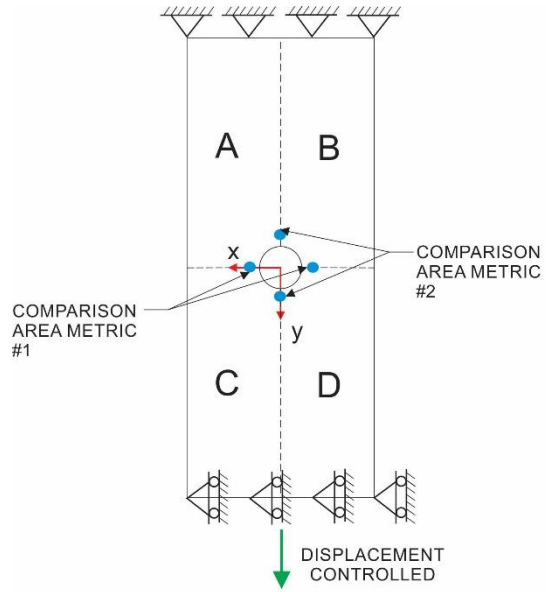


Figure 88. Simulation test conditions, XY plane

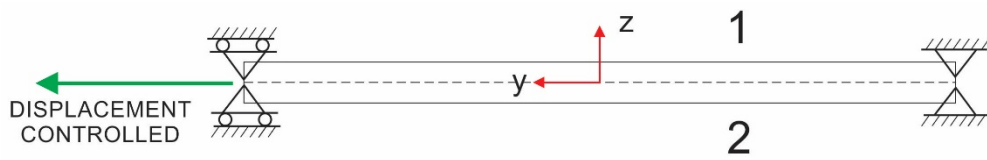
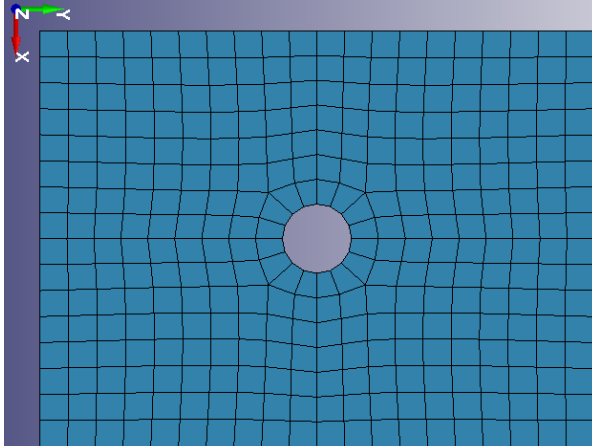
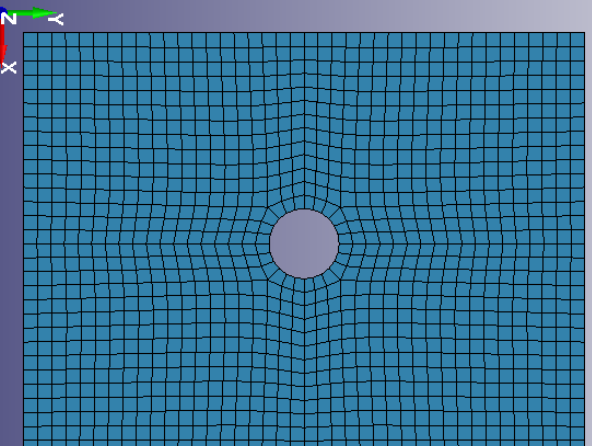
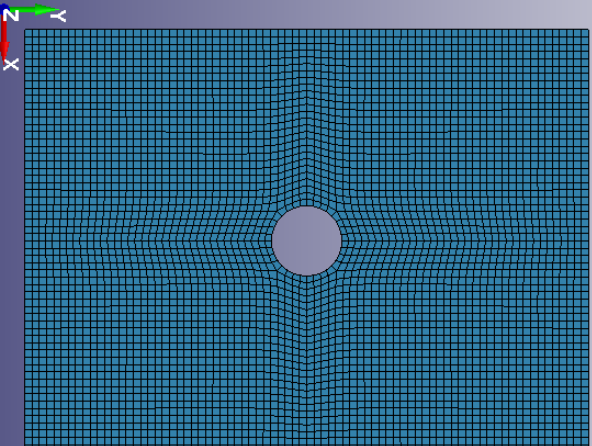


Figure 89. Simulation test conditions, YZ plane

Three Finite Element (FE) models were created with varying element sizes, these are depicted in Table 41.

Table 41. FE model meshes

| Mesh | # of MAT213 elements | # of cohesive elements | XY Plane view of FE model |
|--------|----------------------|------------------------|--|
| Coarse | 2560 | 2240 |  |
| Medium | 9504 | 8316 |  |
| Fine | 35936 | 31444 |  |

6.5.2 Validation metrics

The simulation tests were validated with three distinct metrics comparing the simulation and experimental values. Figure 90, Figure 91, and Figure 92 show the coarse, medium, and fine meshes and the nodes and elements used to compare strain and displacement values with the experiments. Only the left half of the simulation models are shown for simplicity, but information was taken from both sides of the model.

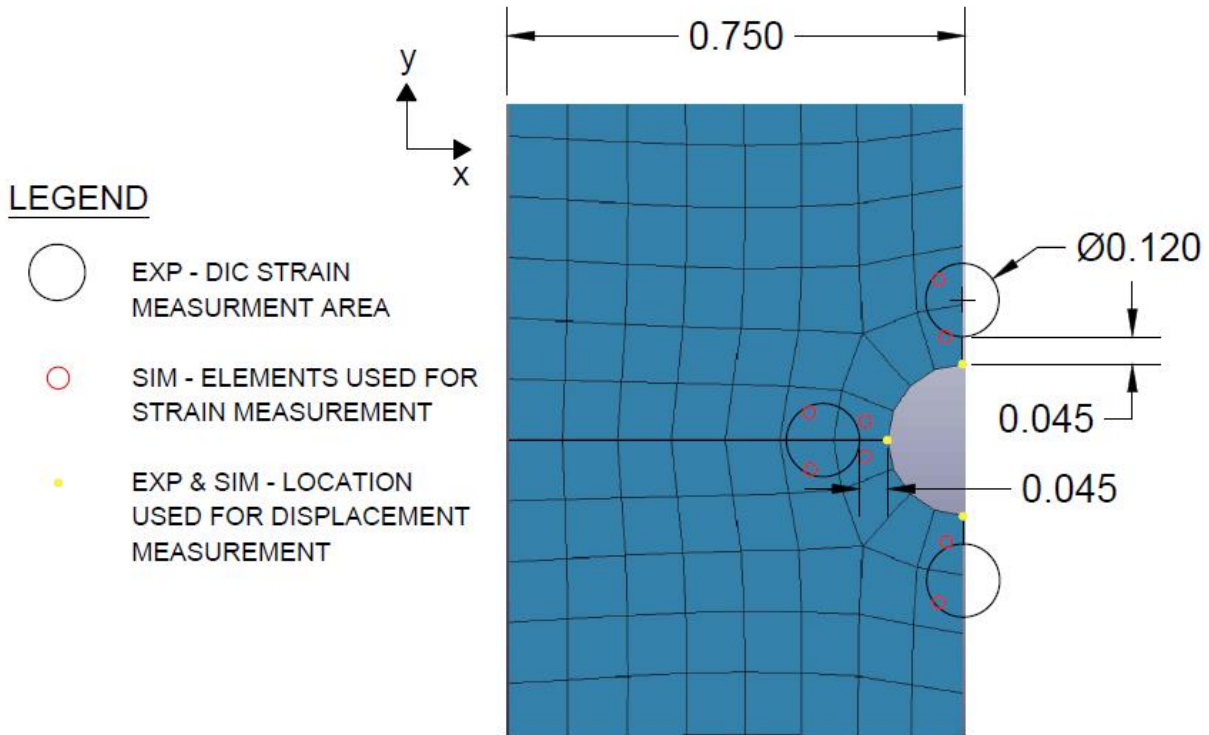


Figure 90. Coarse mesh validation measurement locations

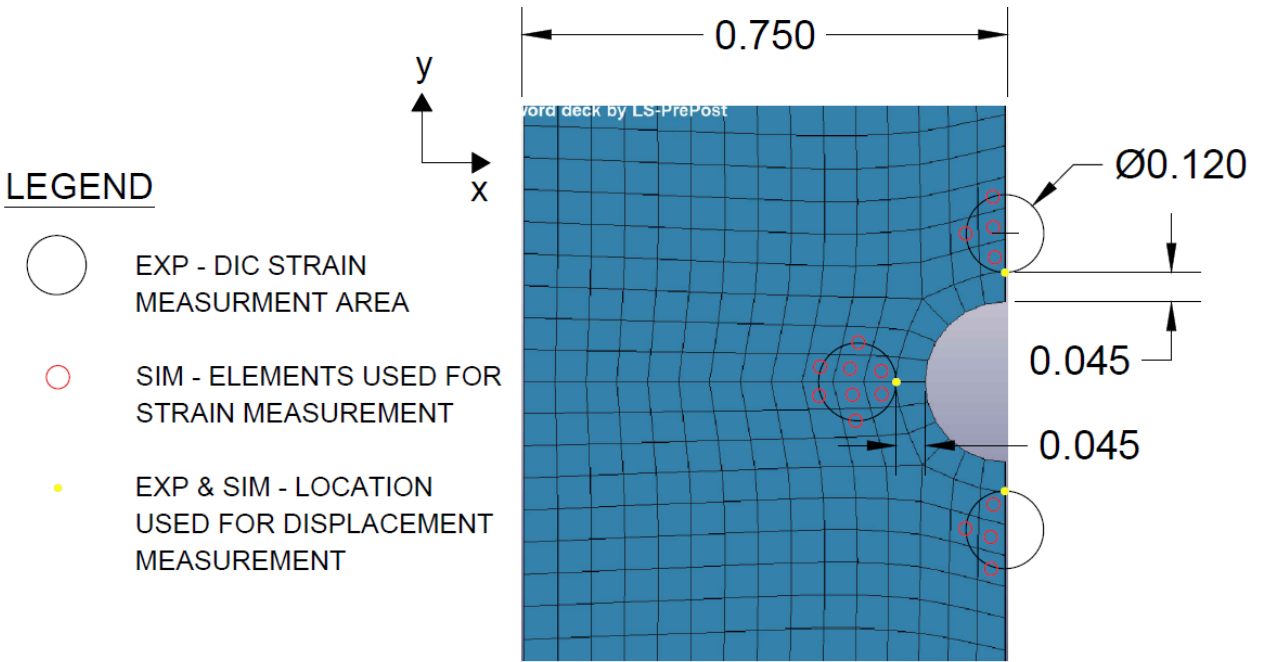


Figure 91. Medium mesh validation measurement locations

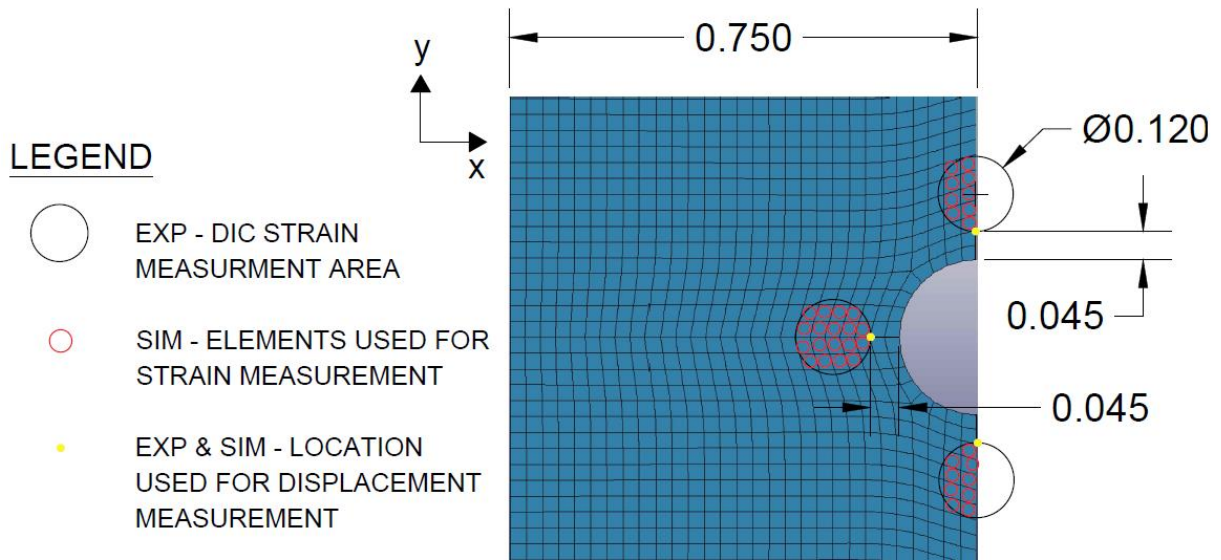


Figure 92. Fine mesh validation measurement locations

Figure 93 shows an example of the measurement areas taken from DIC for the experimental tests. Strain was measured in four areas, indicated by the four circles adjacent to the hole. The figure also shows two digital extensometers, which measured the displacement around the hole, vertically and horizontally.

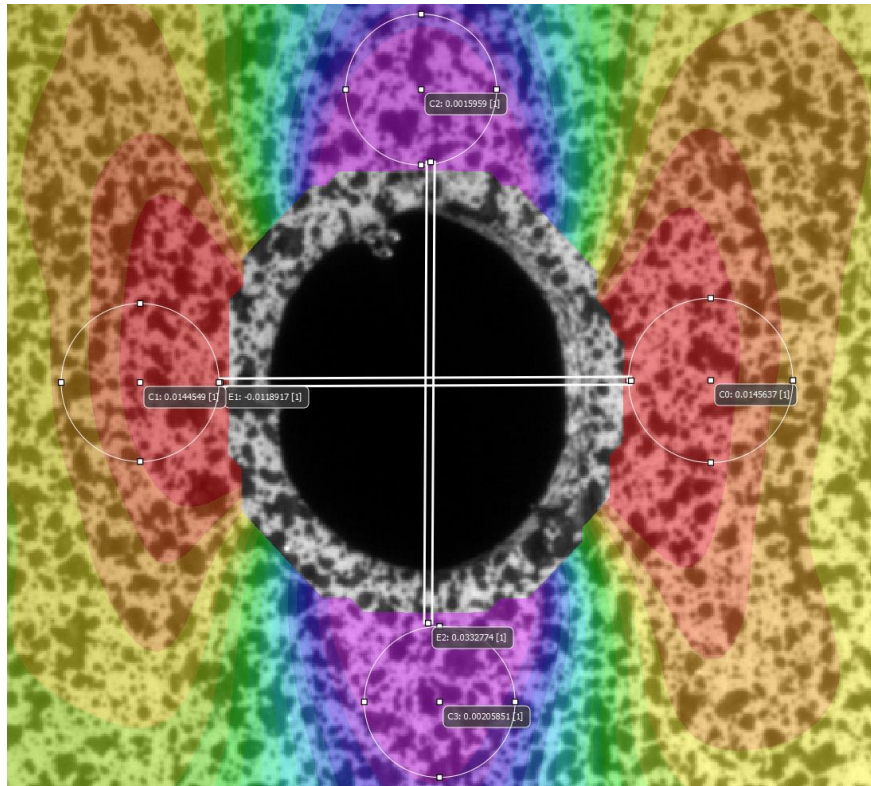


Figure 93. DIC measurement areas

The three metrics used for comparison are outlined in Table 42.

Table 42. Validation metrics description

| Metric | Description |
|--------|--|
| 1 | Comparison of strains for the 0 ⁰ -ply for the area adjacent to the hole in the x direction, right and left of the hole (shown in Figure 90, Figure 91, and Figure 92). The strains ϵ_{xx} , ϵ_{yy} , ϵ_{xy} were plotted against time |
| 2 | Comparison of strains for the 0 ⁰ -ply for the area adjacent to the hole in the y direction, both top and bottom (shown in Figure 90, Figure 91, Figure 92). The strains ϵ_{xx} , ϵ_{yy} , ϵ_{xy} were plotted against time |
| 3 | Comparison of displacements around the hole in both the x and y directions |

Metric 1

A comparison of how the data was captured in the experimental and simulation tests for Metric 1 is shown in Table 43.

Table 43. Tension hole test metric 1

| Data Type | Method of Data Collection |
|------------------|--|
| Experimental | Strains were computed using DIC as an area average of a small circular area directly adjacent to the hole in the x direction on both sides. The data from each side was averaged. These sections are shown in Figure 93. |
| Simulation | Strains taken from the elements with red circles next to the hole in the x direction are shown in Figure 90, Figure 91, and Figure 92. Strains for each element were averaged. |

Metric 2

A comparison of how the data was captured in the experimental and simulation tests for Metric 2 is shown in Table 44.

Table 44. Tension hole test metric 2

| Data Type | Method of Data Collection |
|------------------|---|
| Experimental | Strains were computed using DIC as an area average of a small circular area directly adjacent to the hole in the y direction on both sides. The data from the top and bottom of the hole were compared separately. These sections are shown Figure 93.. |
| Simulation | Strains taken from the elements with red circles next to the hole in the y direction on both sides are shown in Figure 90, Figure 91, and Figure 92. Strains for each element were averaged together. The elements at the top and bottom of the hole were compared separately |

Metric 3

A comparison of how the data was captured in the experimental and simulation tests for Metric 3 is shown in Table 45.

Table 45. Tension hole test metric 3

| Data Type | Method of Data Collection |
|------------------|--|
| Experimental | Digital extensometers were used to track the relative displacement between the top and bottom of the hole and the left and right of the hole as shown in Figure 93.. |
| Simulation | The x and y displacement was recorded for the nodes corresponding to those shown with yellow dots is shown in Figure 90, Figure 91, and Figure 92. For the vertical extension, the relative displacement is recorded as the difference between the two nodes aligned in the y direction. For the horizontal extension, the relative displacement is recorded as the difference between the two nodes aligned in the x direction. |

6.5.3 Results

Figure 94, Figure 95, and Figure 96 show the results for Metric 1.

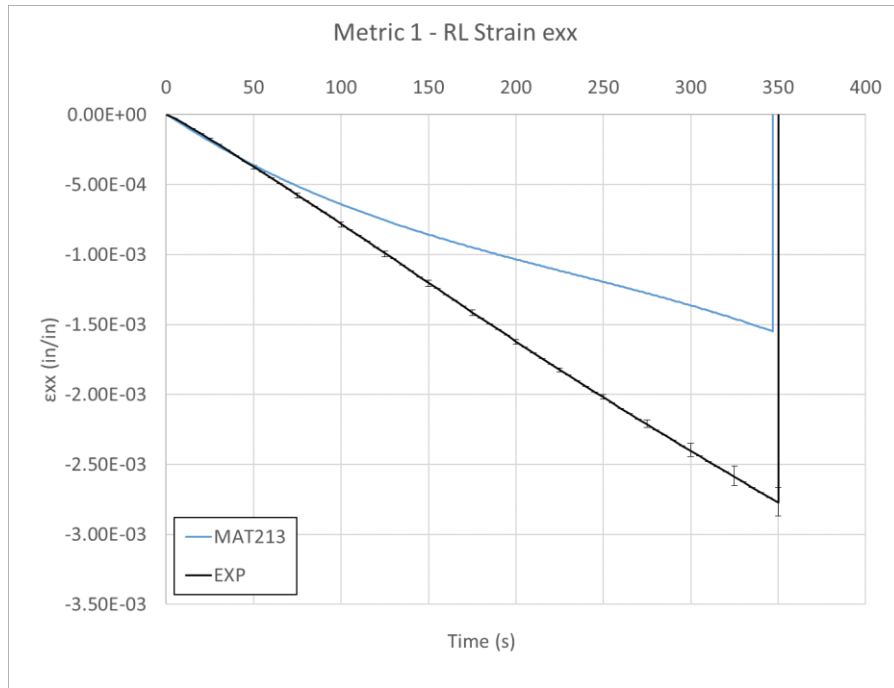


Figure 94. Metric 1 - ϵ_{xx} comparison

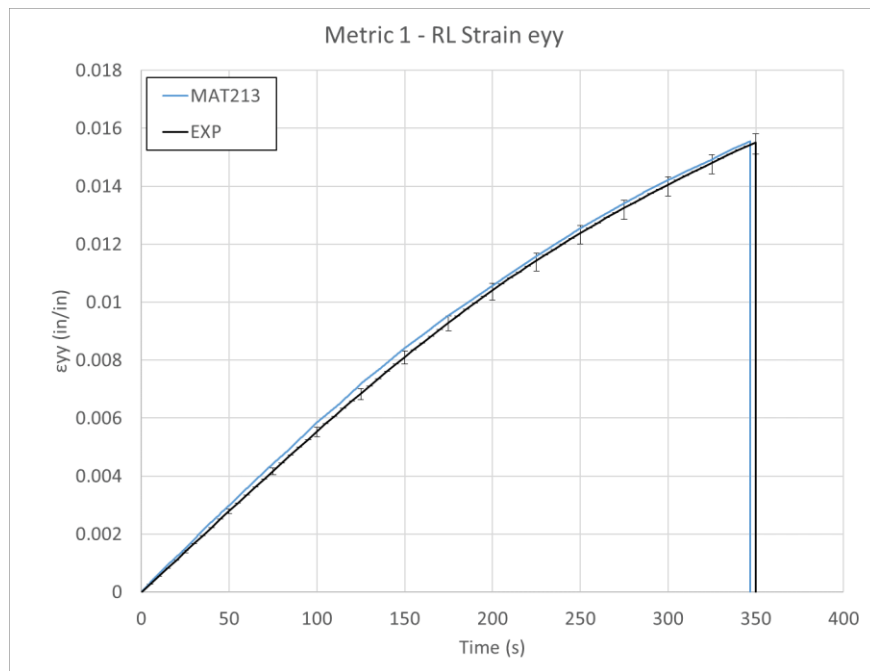


Figure 95. Metric 1 - ϵ_{yy} comparison

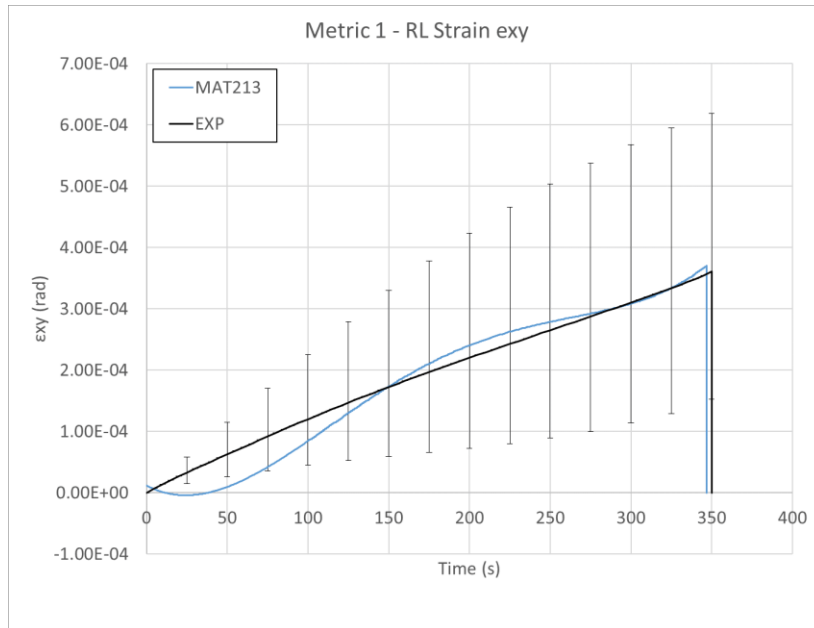


Figure 96. Metric 1 - ϵ_{xy} comparison

Figure 97, Figure 98, and Figure 99 show the results for Metric 2 for the area above the hole.

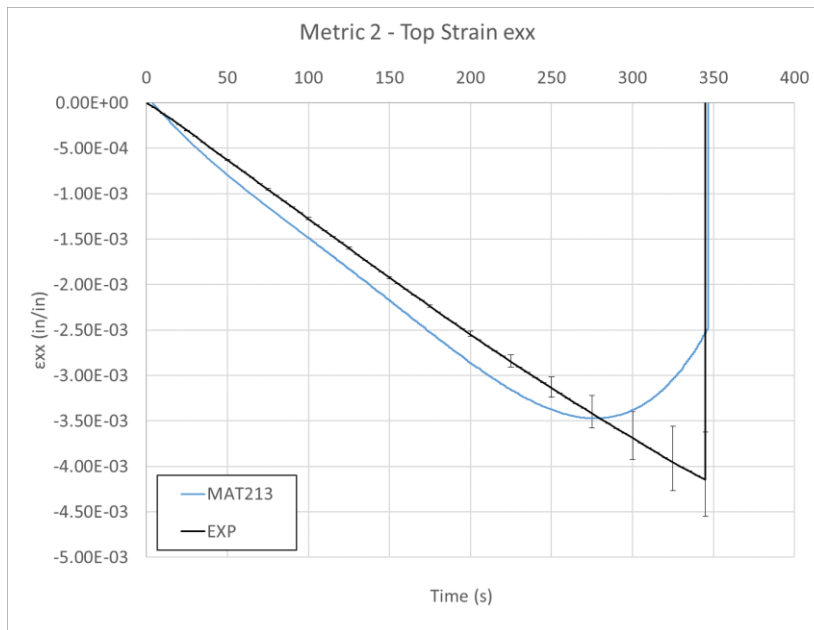


Figure 97. Metric 2 - above hole ϵ_{xx} comparison

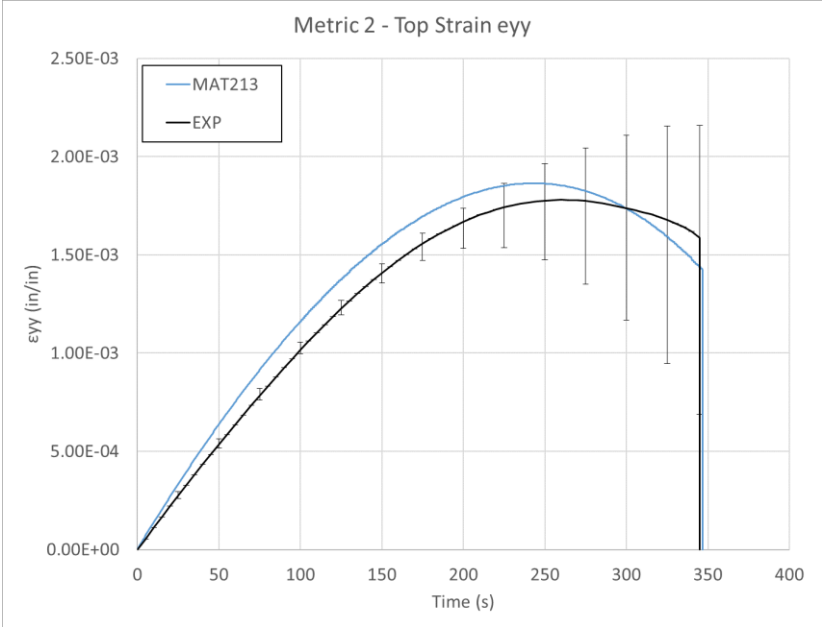


Figure 98. Metric 2 - above hole ϵ_{xx} comparison

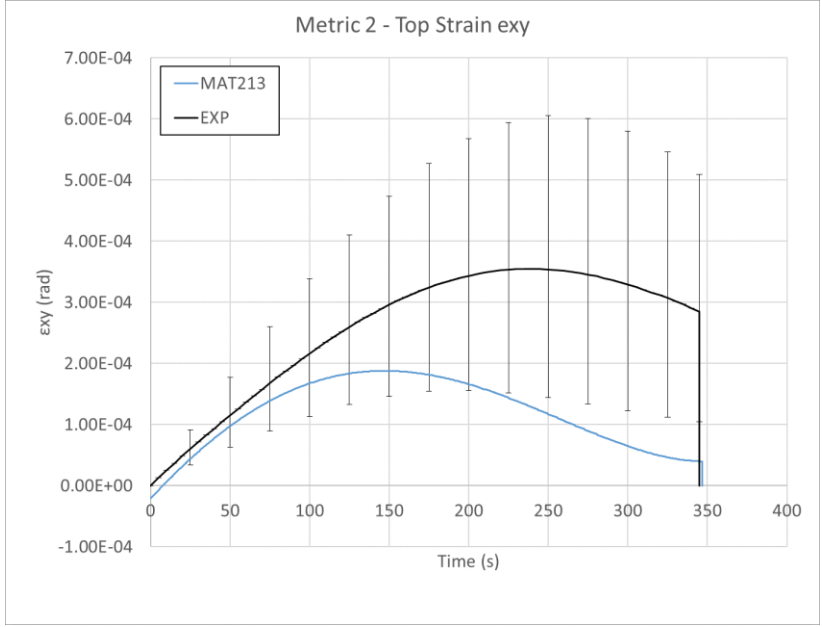


Figure 99. Metric 2 - above hole ϵ_{xy} comparison

Figure 100, Figure 101, and Figure 102 show the results for Metric 2 for the area below the hole.

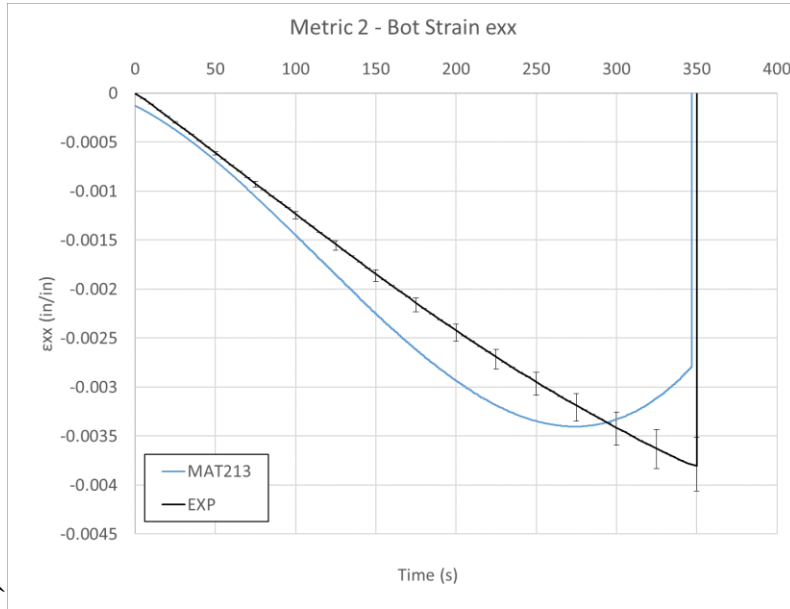


Figure 100. Metric 2 - below hole ϵ_{xx} comparison

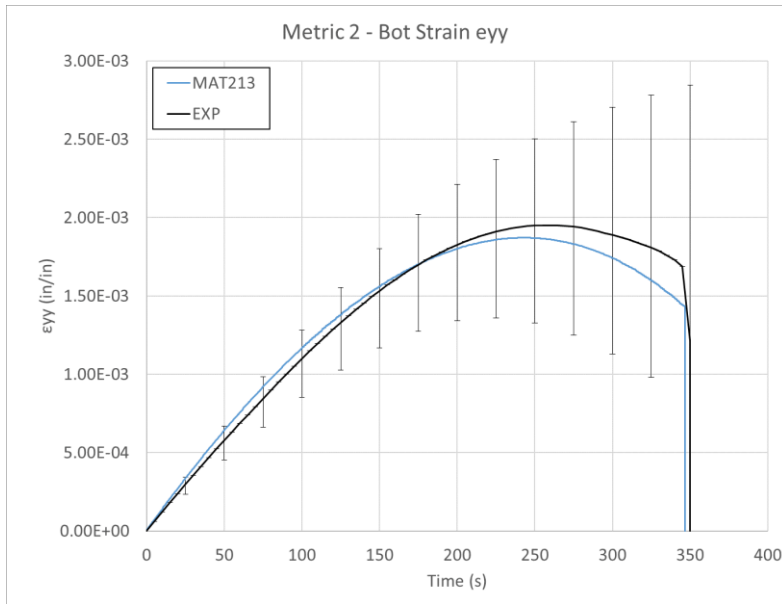


Figure 101. Metric 2 - below hole ϵ_{yy} comparison

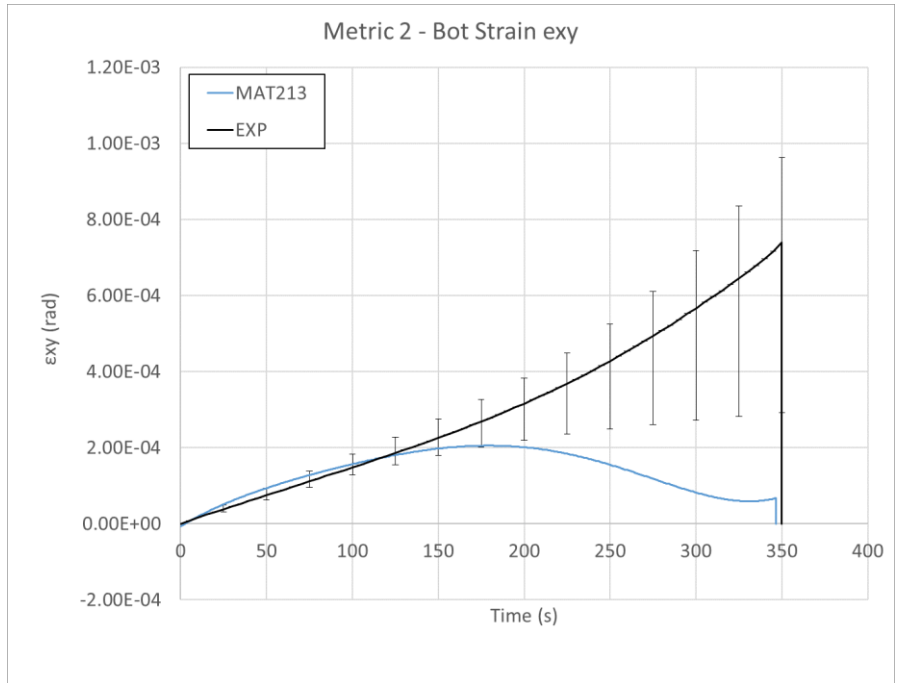


Figure 102. Metric 2 - below hole ϵ_{xy} comparison

Figure 103 and Figure 104 show the results for Metric 3.

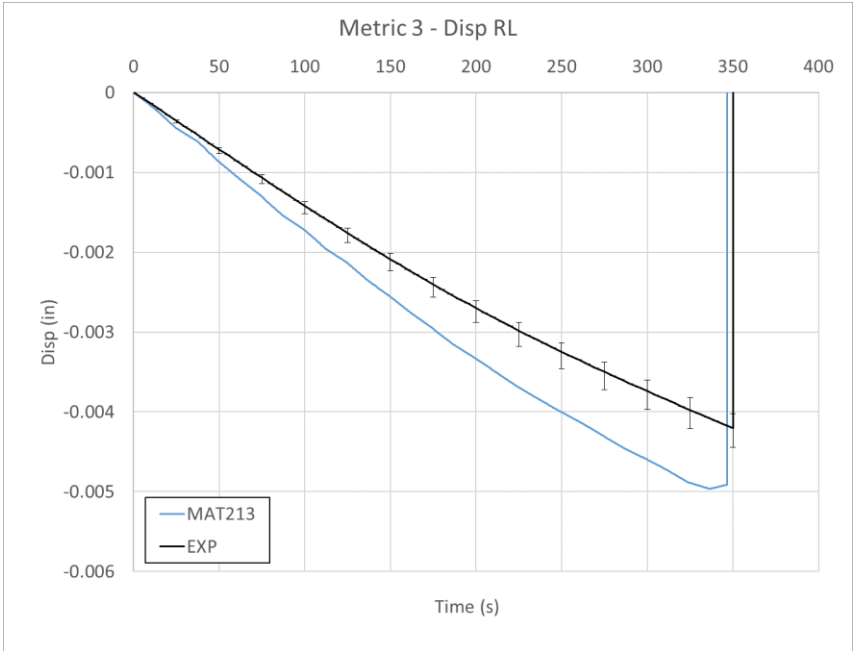


Figure 103. Metric 3 - x-direction displacement

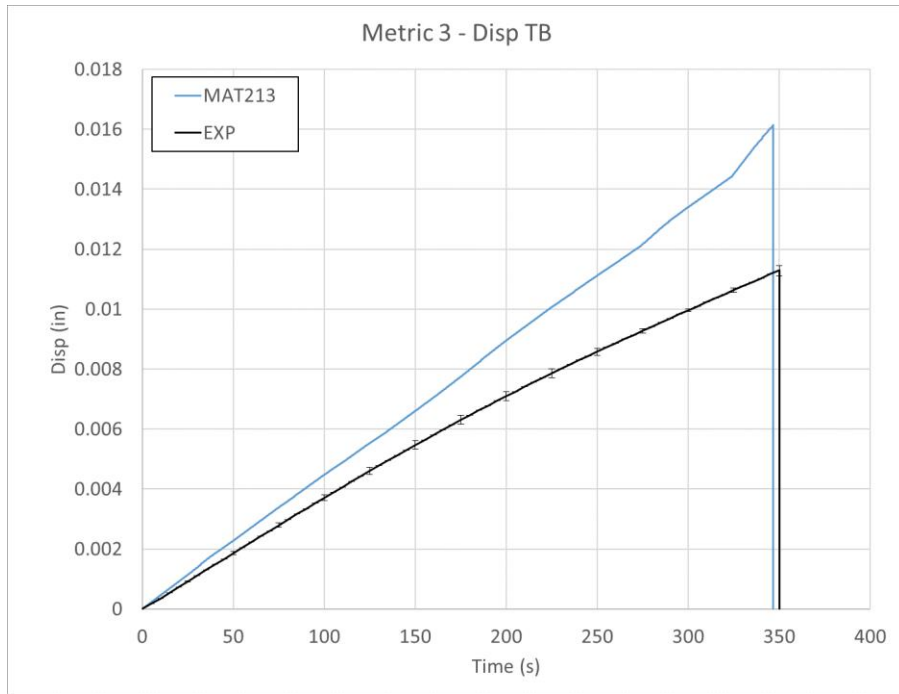


Figure 104. Metric 3 - y-direction displacement

A fringe plot of the y-strain is pictured in Figure 105. The range and color scheme depicting the strain field is identical for the simulation (a) and the experiment (b). The experimental plot shows some asymmetry on the right and left halves of the coupon. However, the magnitudes and shape of the strain concentrations all around the hole match closely between the experimental and simulation plots.

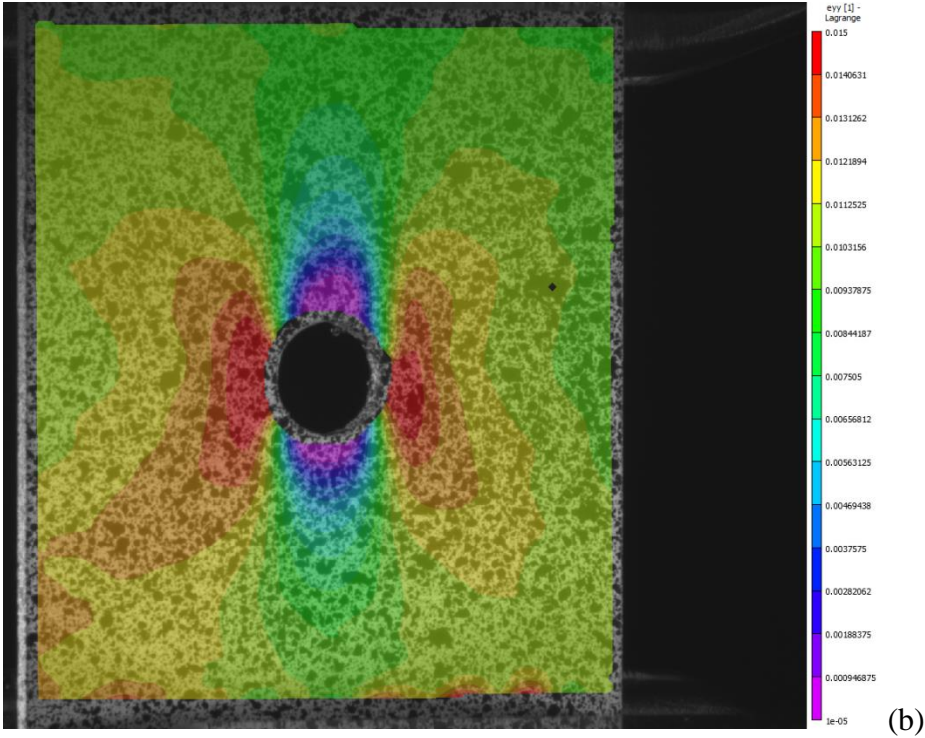
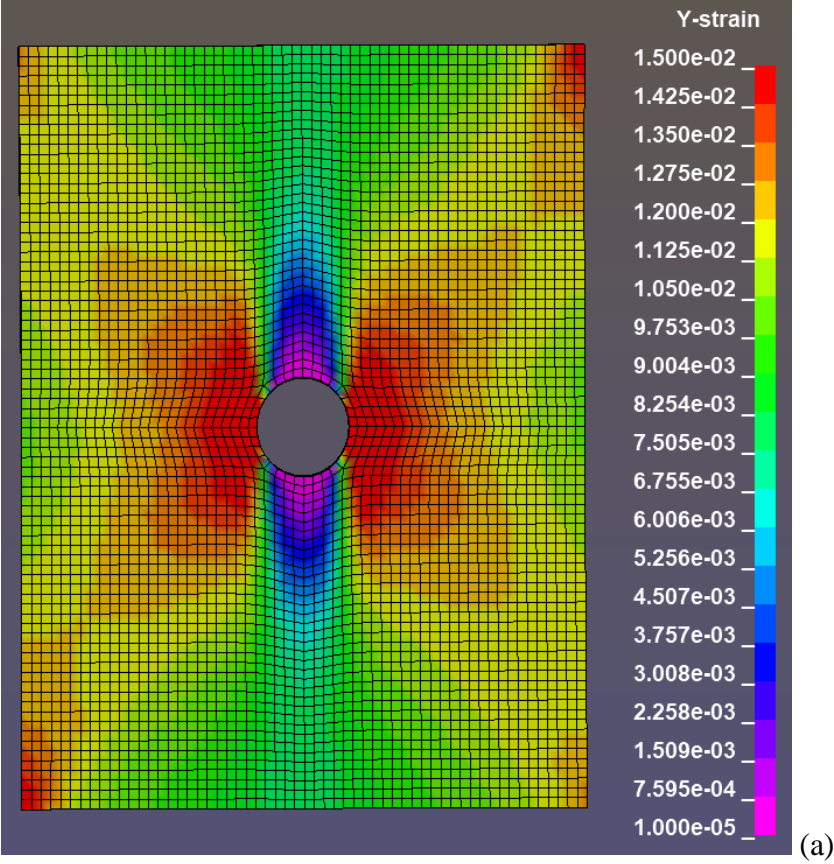


Figure 105. Y-Strain fringe plot of tension-hole test, at $t = 325$ s (a) Simulation (b) Experiment

6.5.4 Discussion

Several of the simulation curves used for comparison had data that was fitted using polynomial regression. The details of the polynomial regressions are shown in Table 46.

Table 46. Polynomial regression fitting of tension with hole simulation metrics

| Metric | Order of polynomial regression | R-squared of regression | Fig. # |
|---------------------------|---------------------------------------|--------------------------------|---------------|
| Metric 1 – RL Strain exx | Cubic | 0.9974 | Figure 94 |
| Metric 1 – RL Strain eyy | None | n/a | Figure 95 |
| Metric 1 – RL Strain exy | Quartic | 0.9959 | Figure 96 |
| Metric 2 – Top Strain exx | Quartic | 0.9943 | Figure 97 |
| Metric 2 – Top Strain eyy | Cubic | 0.9928 | Figure 98 |
| Metric 2 – Top Strain exy | Quartic | 0.7979 | Figure 99 |
| Metric 2 – Bot Strain exx | Cubic | 0.9940 | Figure 100 |
| Metric 2 – Bot Strain eyy | Cubic | 0.9947 | Figure 101 |
| Metric 2 – Bot Strain exy | Quintic | 0.7521 | Figure 102 |
| Metric 3 – Disp RL | None | n/a | Figure 103 |
| Metric 3 – Disp TB | None | n/a | Figure 104 |

Metric 1 indicated that the MAT213 simulation under-predicted the transverse strain to the right and left of the hole by nearly one half. The longitudinal strain at this location was well predicted within the experimental values. The experimental values of the shear strain at this location had a very large range within which was the simulation curve.

Metric 2 showed a close comparison for transverse, longitudinal and shear strain both above and below the hole. The shear strain below the hole visually featured the most deviation between the experimental and simulation curves. The initial shear strain at this location was well predicted by the simulation until a time of approximately 150 seconds, at which time the experimental values increased exponentially, but the simulation values decreased.

Metric 3 indicated that the MAT213 simulation over-predicted the displacement around the hole in both the x and y direction. By the end of the simulation, the x-direction displacement was over-predicted by approximately 25% and the y-displacement was over-predicted by approximately 30%.

The overestimation of the displacements around the hole could be due to errors in the simulated delamination around the hole. In both the experimental and simulation test coupons, delamination was observed around the hole at the end of the test, however the amount of delamination was difficult to compare. The simulation could have delaminated more than the experiment and led to the overestimation of displacement around the hole. This difference could be amended as the cohesive zone parameters continue to be tuned.

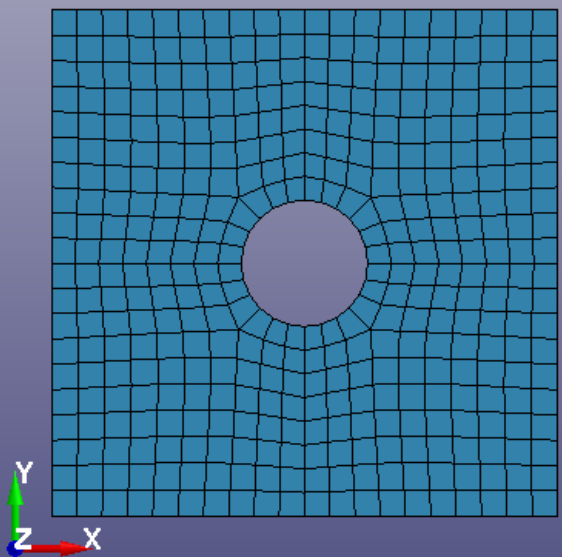
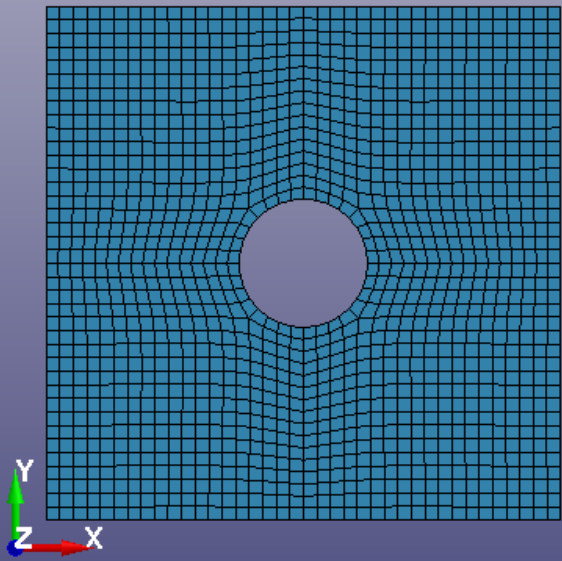
6.6 LS-DYNA simulation of stacked-ply compression – stress concentration test

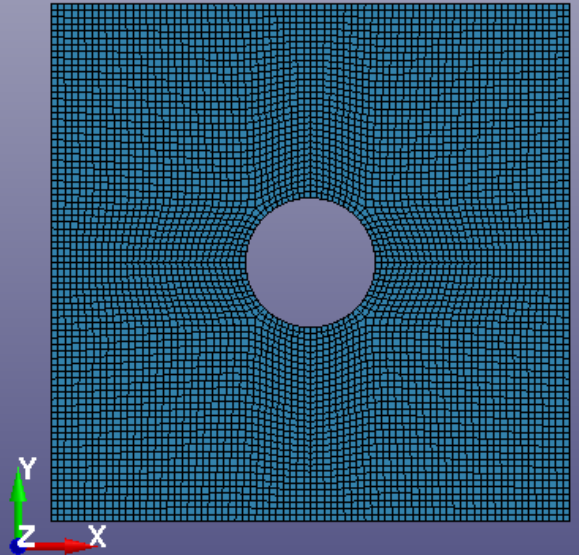
6.6.1 Simulation modeling

Only the gage area of the experimental test was considered for the simulations. Thus, the experimental and simulation modeling and fixity conditions was the same as for the stacked-ply tension hole tests. The dimensions of gage area were different, but the overall geometry was the same.

Three Finite Element (FE) models were created with varying element sizes, these are depicted in Table 47.

Table 47. FE model meshes

| Mesh | # of MAT213 elements | # of cohesive elements | XY Plane view of FE model |
|--------|----------------------|------------------------|--|
| Coarse | 3104 | 2716 |  |
| Medium | 11296 | 9884 |  |

| Mesh | # of MAT213 elements | # of cohesive elements | XY Plane view of FE model |
|------|----------------------|------------------------|--|
| Fine | 44768 | 39172 |  |

6.6.2 Validation metrics

The simulation tests were validated with three distinct metrics comparing the simulation and experimental values. Figure 106, Figure 107, and Figure 108 show the coarse, medium, and fine meshes and the nodes and elements used to compare strain and displacement values with the experiments. Only the left half of the simulation models are shown for simplicity, but information was taken from both sides of the model. These figures are similar to those for the tension with hole tests, except the dimensions of the strain gage sections are slightly smaller. This was due to the smaller overall gage section of the compression with hole tests.

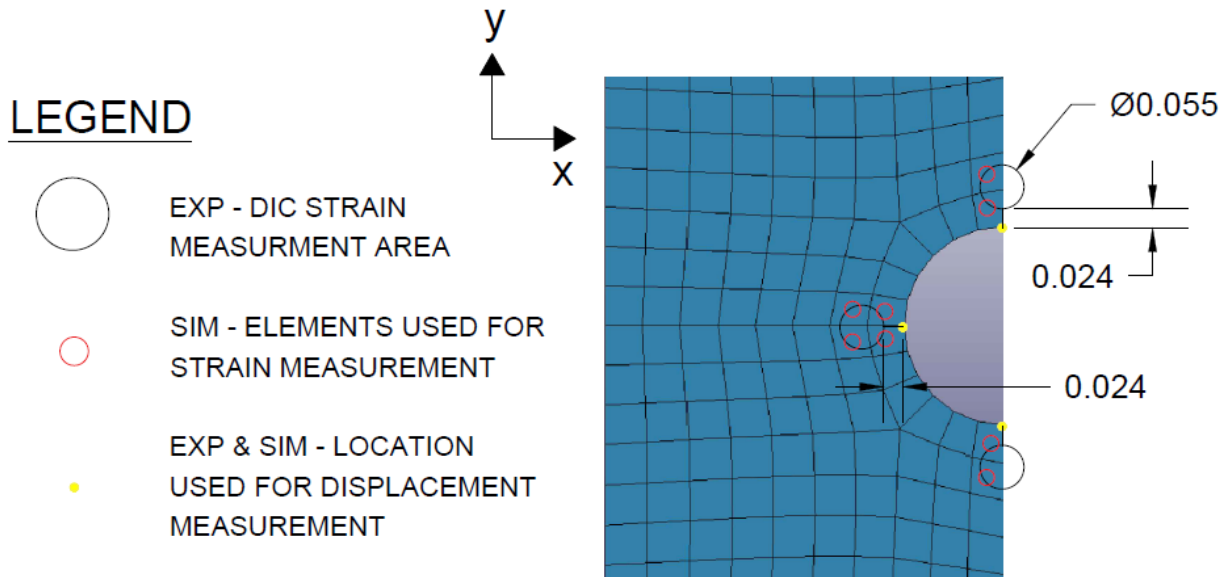


Figure 106. Coarse mesh validation measurement locations

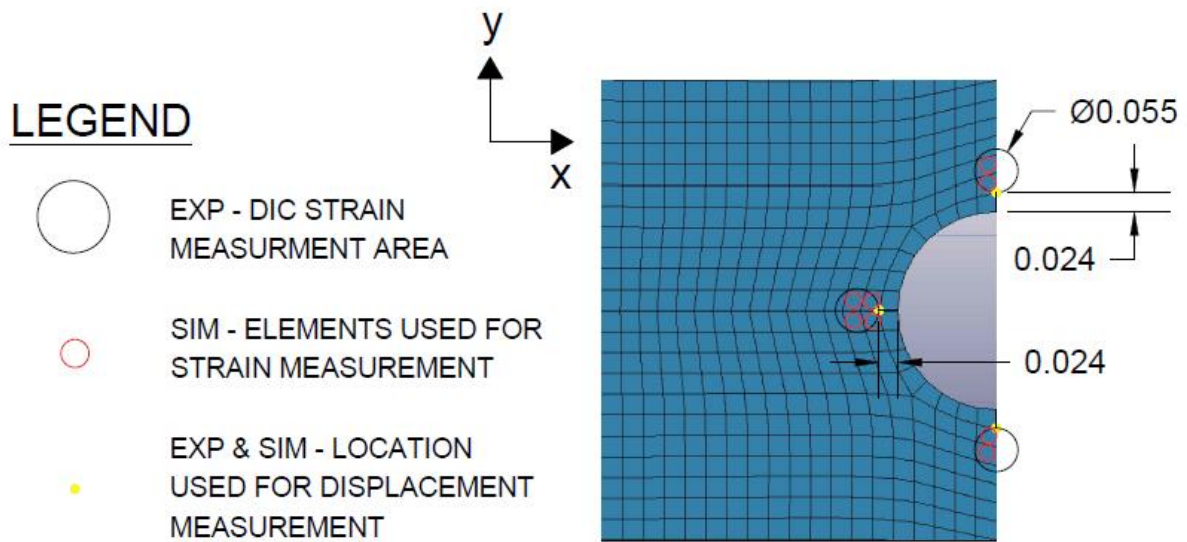


Figure 107. Medium mesh validation measurement locations

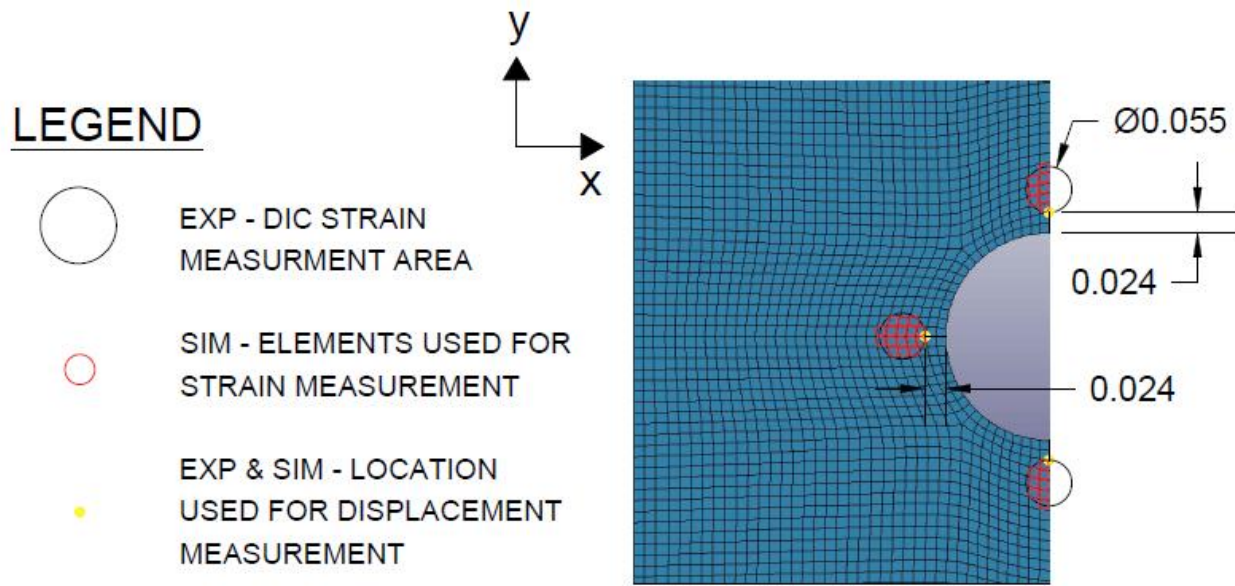


Figure 108. Fine mesh validation measurement locations

The validation metrics and data collection methods were the same as for the stacked-ply tension with hole tests.

6.6.3 Results

MAT213 specifications that were used for the results shown are detailed in Table 48.

Table 48. MAT213 Specifications

| Parameter | Specification |
|---------------|--|
| Damage Model | Incorporated, only uncoupled 2-direction compression and uncoupled 12-plane shear are included |
| Failure Model | Not incorporated |

Figure 109, Figure 110, and Figure 111 show the results for Metric 1.

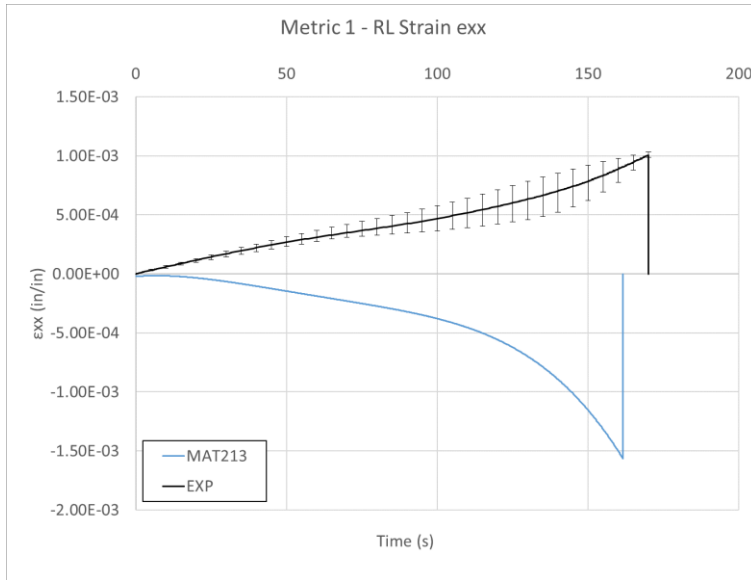


Figure 109. Metric 1 - ϵ_{xx} comparison

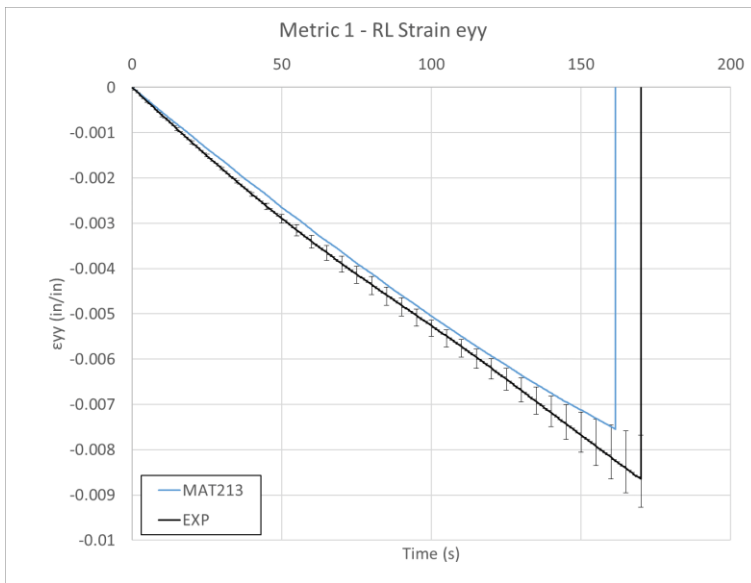


Figure 110. Metric 1 - ϵ_{yy} comparison

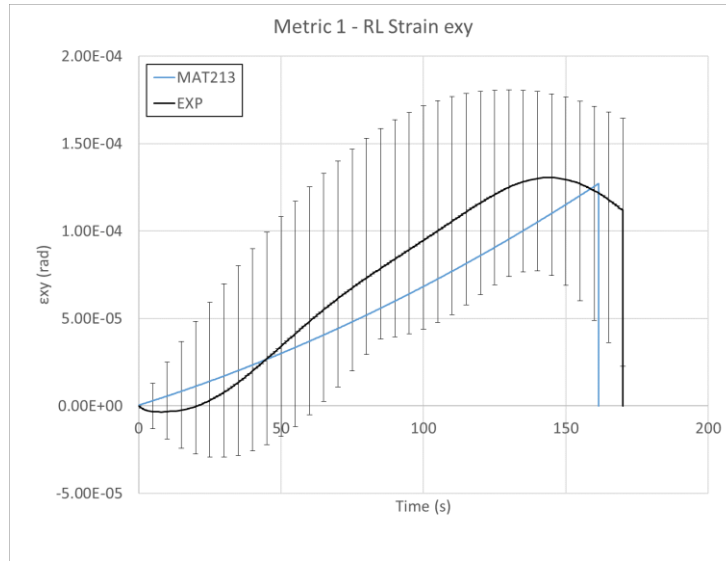


Figure 111. Metric 1 - ϵ_{xy} comparison

Figure 112, Figure 113, and Figure 114 show the results for Metric 2 for the area above the hole.

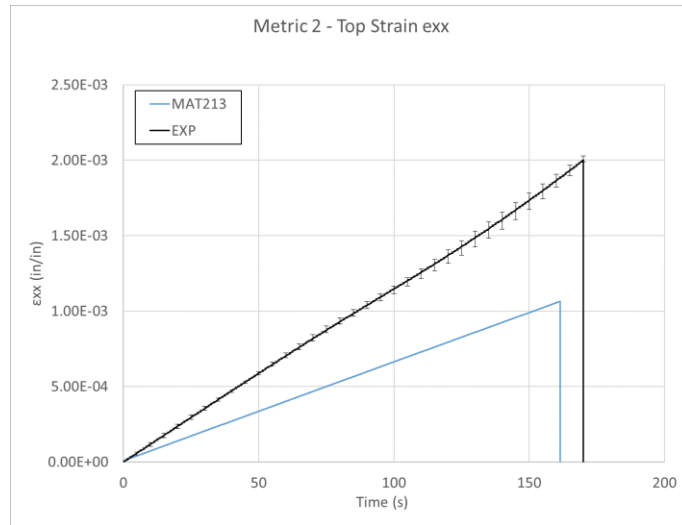


Figure 112. Metric 2 - above hole ϵ_{xx} comparison

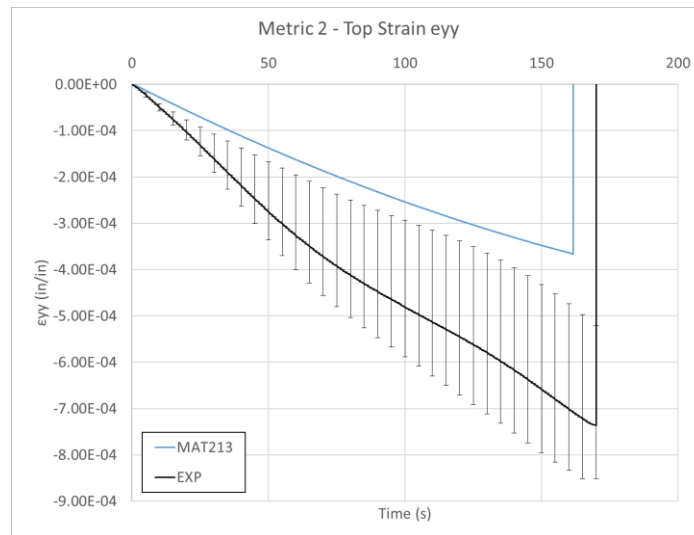


Figure 113. Metric 2 - above hole ϵ_{yy} comparison

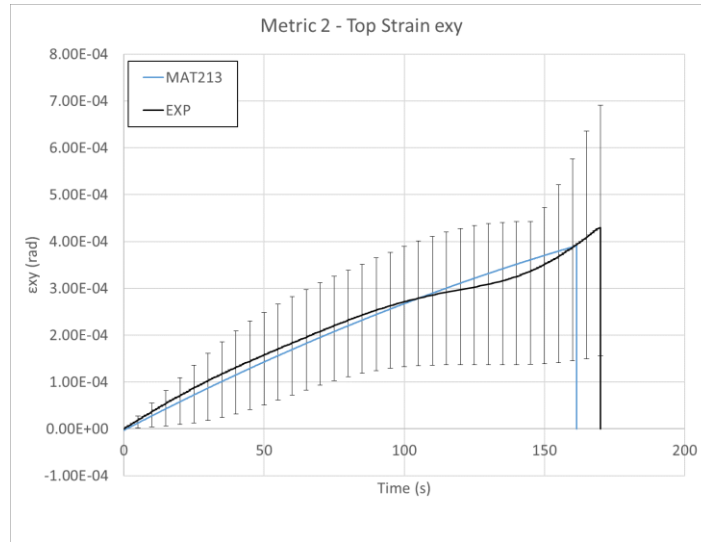


Figure 114. Metric 2 - above hole ϵ_{xy} comparison

Figure 115, Figure 116, and Figure 117 show the results for Metric 2 for the area below the hole.

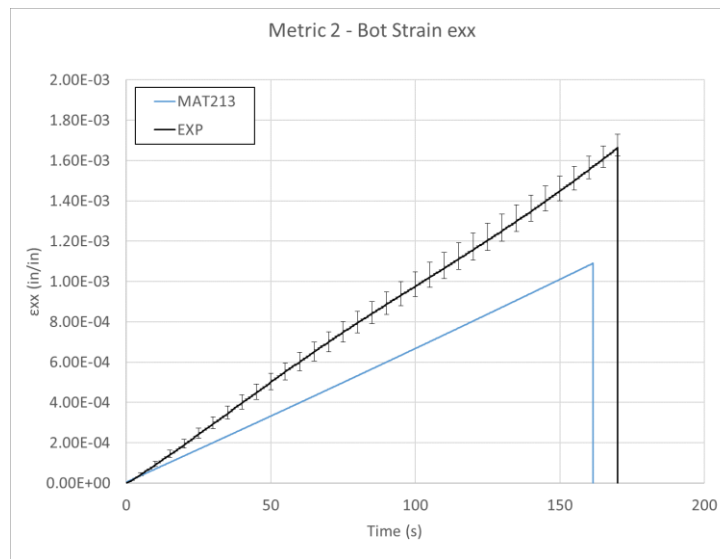


Figure 115. Metric 2 - below hole ϵ_{xx} comparison

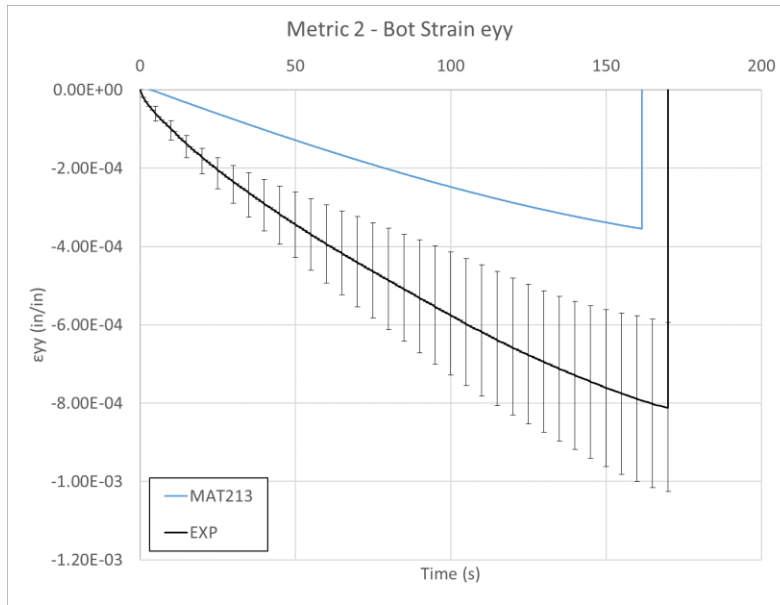


Figure 116. Metric 2 - below hole ϵ_{yy} comparison

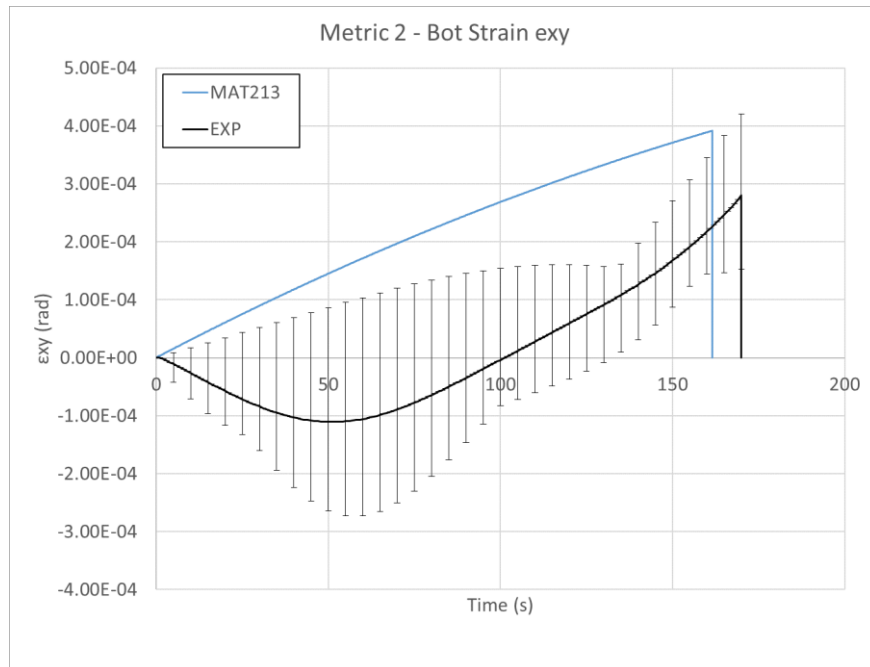


Figure 117. Metric 2 - below hole ϵ_{xy} comparison

Figure 118 and Figure 119 show the results for Metric 3.

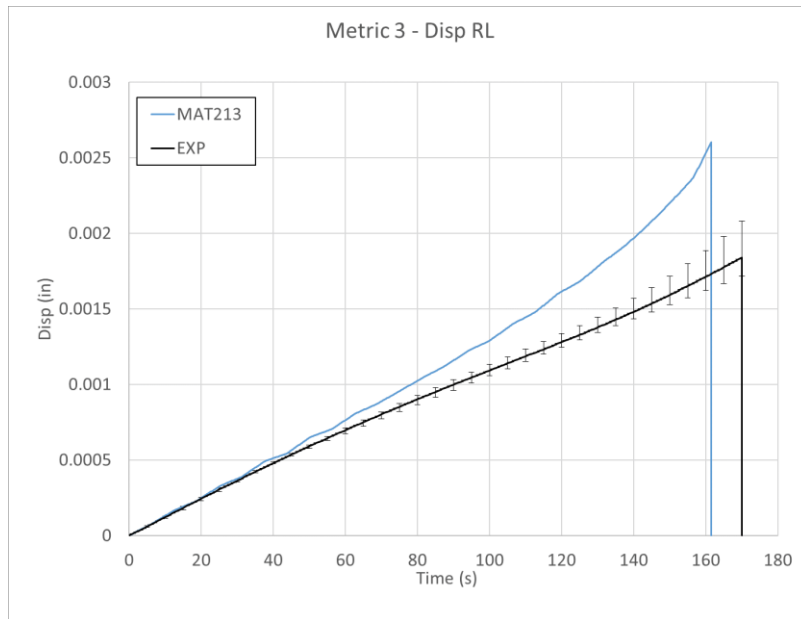


Figure 118. Metric 3 - x-direction displacement

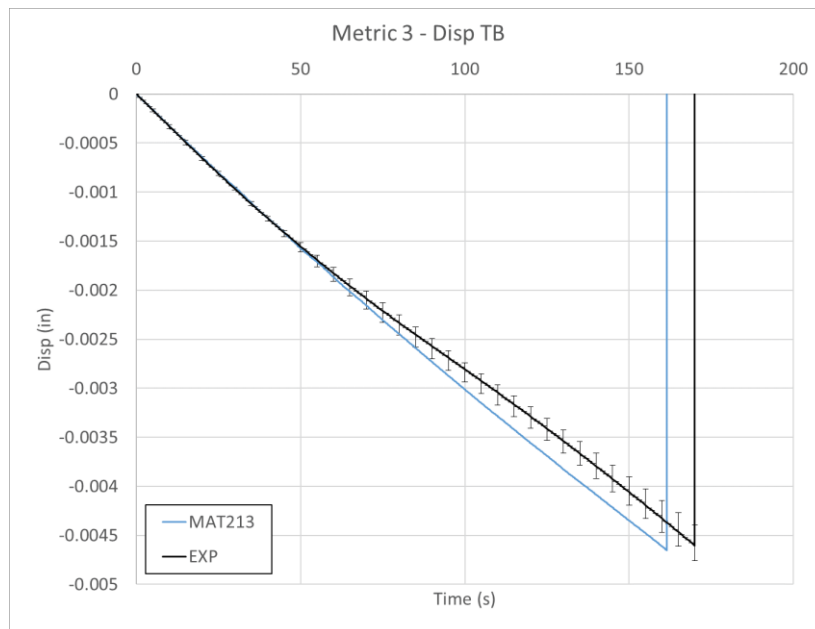


Figure 119. Metric 3 - y-direction displacement

A fringe plot of the y-strain is pictured in Figure 120. The range and color scheme depicting the strain field is identical for the simulation (a) and the experiment (b). The experimental plot shows asymmetry between the right and left side, with less strain concentration directly to the

left of the hole. The stress concentrations around the rest of the hole match well between the experiment and simulation.

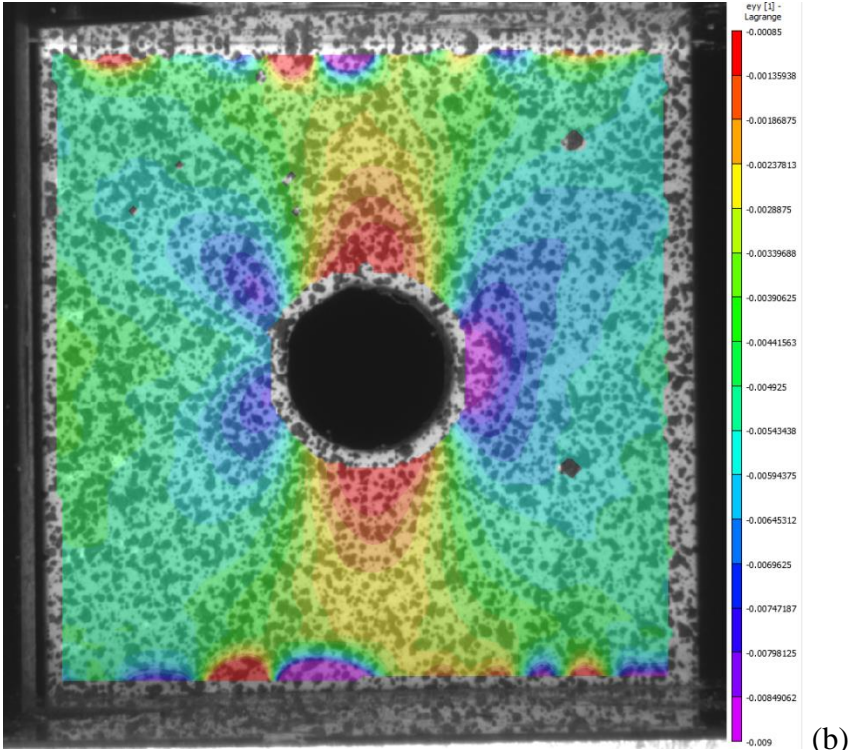
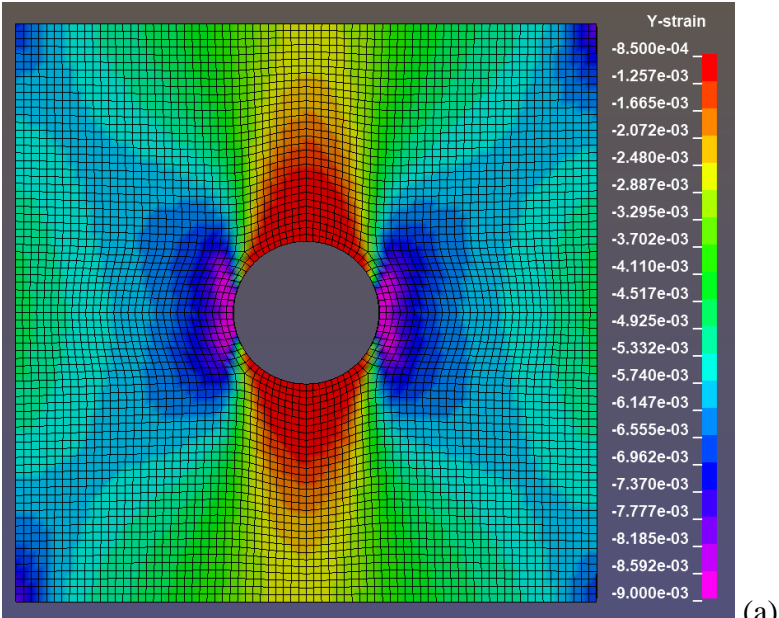


Figure 120. Y-Strain fringe plot of compression-hole test, at $t = 155$ s (a) Simulation (b) Experiment

6.6.4 Discussion

Several of the simulation curves used for comparison had data that was fitted using polynomial regression. The details of the polynomial regressions are shown in Table 49.

Table 49. Polynomial regression fitting of compression with hole simulation metrics

| Metric | Order of polynomial regression | R-squared of regression | Fig. # |
|---------------------------|--------------------------------|-------------------------|------------|
| Metric 1 – RL Strain exx | Quartic | 0.9958 | Figure 109 |
| Metric 1 – RL Strain eyy | None | n/a | Figure 110 |
| Metric 1 – RL Strain exy | Quadratic | 0.9863 | Figure 111 |
| Metric 2 – Top Strain exx | Quadratic | 0.9958 | Figure 112 |
| Metric 2 – Top Strain eyy | Quadratic | 0.9980 | Figure 113 |
| Metric 2 – Top Strain exy | Quadratic | 0.9995 | Figure 114 |
| Metric 2 – Bot Strain exx | Quadratic | 0.9928 | Figure 115 |
| Metric 2 – Bot Strain eyy | Cubic | 0.9982 | Figure 116 |
| Metric 2 – Bot Strain exy | Quadratic | 0.9995 | Figure 117 |
| Metric 3 – Disp RL | None | n/a | Figure 118 |
| Metric 3 – Disp TB | None | n/a | Figure 119 |

Metric 1 indicated that the MAT213 simulation predicted the longitudinal and shear strain to the right and left of the hole within the experimental values. The transverse strain predicted by MAT213 had a similar magnitude to the experimental values, but the simulation values were negative while the experimental values were positive.

Metric 2 indicated that the MAT213 simulation under-predicted the transverse and longitudinal strain above and below the hole by a factor of approximately one half compared to the experimental values. The shear strain was predicted by MAT213 within the experimental values.

Metric 3 indicated that the MAT213 simulation very closely predicted the y-direction displacement while it over-predicted the x-direction displacement compared to the experimental values. The x-direction displacement simulated values were within the experimental values for approximately a third of the duration of the test, at which time it began to over-predict the displacement in that direction.

The overestimation of the displacements around the hole in the x-direction could be due to errors in the simulated delamination around the hole. This result was similar to that of the stacked-ply tension with hole test. The differences between the simulation and experimental result could be amended as the cohesive zone parameters are tuned.

7 SEM imaging for MAT213 model validation

7.1 Objective

The purposes of the examination of untested, damaged, and failed specimens of the T800/F3900 composite included to observe and understand the underlying structure of the composite. Another purpose was to observe the behavior of the composite at the micro level once it has been loaded, including loading levels cause failure at the coupon level. To fulfill these objectives, tested coupons were obtained from the QS-RT tests detailed in the experimental report produced by Khaled et al. (Khaled, Shyamsunder, Schmidt, Hoffarth, & Rajan). These previously tested coupons were engaged in a process of cutting, grinding, polishing and imaging to determine the damage and failure patterns at the micro-level.

Four samples used this procedure to obtain SEM images. The samples used in this procedure are presented in Table 50.

Table 50. SEM image samples

| Sample Name | Original Test Name | Original Test Type |
|----------------|--------------------|---|
| Virgin | - | - |
| Damaged | TFC2T2C-7 | 2 direction, tension and compression coupled damage |
| Failed | TFC2-13 | Compression – 2 direction |
| Failed - Shear | TFS12-8 | Shear – 12 plane |

The objective of the study was to determine if there was damage at the micro-level that would result in the coupon-level damage or failure that was demonstrated in the original experimental procedure.

Types of micro-level damage that were searched for and discovered include fiber damage, fiber-matrix debonding, fiber interface damage, matrix damage, and interlayer delamination.

7.2 Procedure

SEM chamber sizes restricted the allowable sample size and required the specimens first be cut into smaller pieces. Specimens were cut with a Dynacut¹¹ high speed saw manufactured by National Scientific Company. The blade used for cutting was a silicon carbide abrasive wheel, #10-1146 14" X 1/16" X 3/4" Arbor - Grade 1527.

¹¹ <http://www.dynacut.com/diam.htm>

Specimens were cut at a minimum of 50 mm away from the area of interest to be used for imaging. This minimum distance prevented damaged induced in the specimen at the area of interest by the cutting process.

Embedding

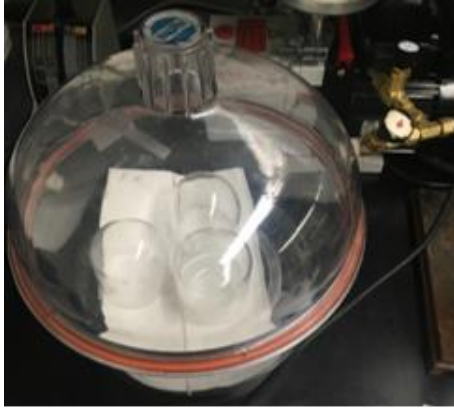
The samples were embedded in epoxy to preserve their post-test state during the grinding and polishing process. The epoxy was a two-part EpoxySet¹² manufactured by Allied High Tech Products. The epoxy is shown in Figure 121.



(a) (b)
Figure 121. Epoxy set components (a) Resin (b) Hardener

The embedding process utilized a vacuum chamber that ensured air bubbles were extracted from the mixed epoxy set. This vacuum chamber is shown in Figure 122(a). The mixed epoxy set was then poured into a cylindrical fixture containing the sample, as shown in Figure 122(b).

¹² <https://consumables.alliedhightech.com/EpoxySet-p/epxyst.htm>



(a)



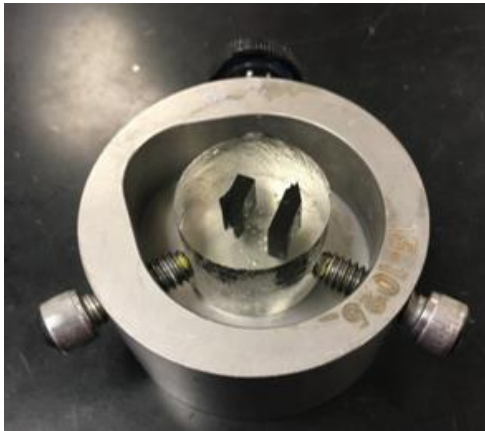
(b)

Figure 122. Epoxy embedding equipment (a) Vacuum chamber (b) Sample holder

Vacuum grease was used in the fixture to allow the embedded sample to be extracted from the fixture once the epoxy had cured.

Grinding and Polishing

Once the epoxy set had cured, the sample was extracted and applied in a grinding and polishing process to prepare it for microscopy. A Multiprep Polishing System¹³ was used to grind the sample to the location near the point of interest and then polish it for detailed microscope images. The Multiprep system is shown in Figure 123(b). The fixture used with this machine is shown in Figure 123(a). This fixture ensured a level viewing surface on the sample.



(a)



(b)

Figure 123. Grinding and polishing equipment (a) Allied machine specimen holder (b) Allied machine

¹³ <http://www.alliedhightech.com/Equipment/multiprep-polishing-system-8>

In addition to silicon carbide discs and water, a few materials were needed for the finer polishing steps. These are shown in Figure 124 and are detailed in Table 51.



Figure 124. Polishing materials (a) RedLube (b) Diamond suspension (c) Colloidal silica suspension

Six types of discs were used with the Multiprep machine to reach the area of interest and polish it to the desired level. Each step and its specifications for use with the Multiprep machine are detailed in Table 51.

Table 51. Grinding and polishing procedure

| Grinding/ Polishing Step # | Abrasive | Type | Carrier | Coolant | Platen Speed (RPM) / Direction | Force (N) | Time (min) |
|----------------------------------|--------------------|------------------|---|-----------------------|---|--------------|---------------------|
| 1 | P-800 | Silicon Carbide | Abrasive Disc | Water | 300/Comp | 25 | To area of interest |
| 2 | P-1200 | Silicon Carbide | Abrasive Disc | Water | 300/Comp | 25 | 2 |
| 3 | P-2400 | Silicon Carbide | Abrasive Disc | Water | 300/Comp | 25 | 2 |
| 4 | P-4000 | Silicon Carbide | Abrasive Disc | Water | 300/Comp | 25 | 2 |
| 5 | 1 μm | Diamond | Diamond Suspension ¹⁴ | RedLube ¹⁵ | 150/Comp | 30 | 5 |
| 6 | 0.04 μm | Colloidal Silica | Colloidal Silica Suspension ¹⁶ | Water | 150/Comp | 30 | 2 |

¹⁴ <https://consumables.alliedhightech.com/Diamond-Suspensions-Polycrystalline-Water-Based-p/diawtr-poly.htm>

¹⁵ <https://consumables.alliedhightech.com/RedLube-p/redlub.htm>

¹⁶ <https://consumables.alliedhightech.com/Colloidal-Silica-Suspension-Non-Stick-Formula-p/collsil04.htm>

As an example of the importance of the polishing process, Figure 125 shows a specimen that has been partly polished. This specimen was slightly un-level, which allowed the right side to be polished well with all six steps from Table 51 while the left half was only polished with the first couple of steps.

In Figure 125, the unpolished (left) side shows large scuffs on the surface. These can be seen streaking across the surface of the specimen. The polished (right) side has no such streaks and is smooth throughout.

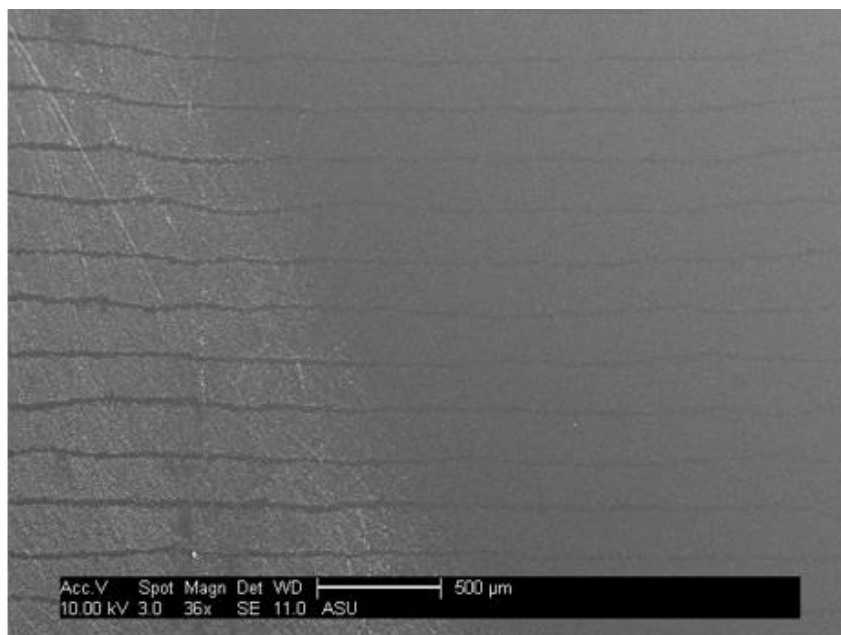


Figure 125. Example of half polished specimen

Imaging

Polished samples were coated with gold/palladium using a Denton Vacuum Desk II Sputter Coater¹⁷. The gold/palladium deposition rate was nearly 10 nm for 120 seconds. The samples were placed in the machine for a duration of 60 seconds to accumulate a deposition of approximately 5 nm. The sputter coater is shown in Figure 126(b).

¹⁷ <https://www.dentonvacuum.com/>

The samples were then examined with a Phillips Environmental Scanning Electron Microscope XL30 ESEM FEG¹⁸. This SEM featured a Schottky Field Emission Source and was used at voltages between 10 and 20 kV. The SEM is shown in Figure 126(a).



Figure 126. SEM imaging equipment (a) XL30 ESEM FEG (b) Sputter coater

7.3 Results

7.3.1 Virgin sample

The untested sample before the cutting process is shown in Figure 127.



Figure 127. Virgin sample before cutting

The schematic of the cut lines and polishing area is shown in Figure 128. The sample was polished in the hatched region of this figure, up to the imaging plane.

¹⁸ <https://le-csss.asu.edu/equipment/xl30-environmental-feg-fei>

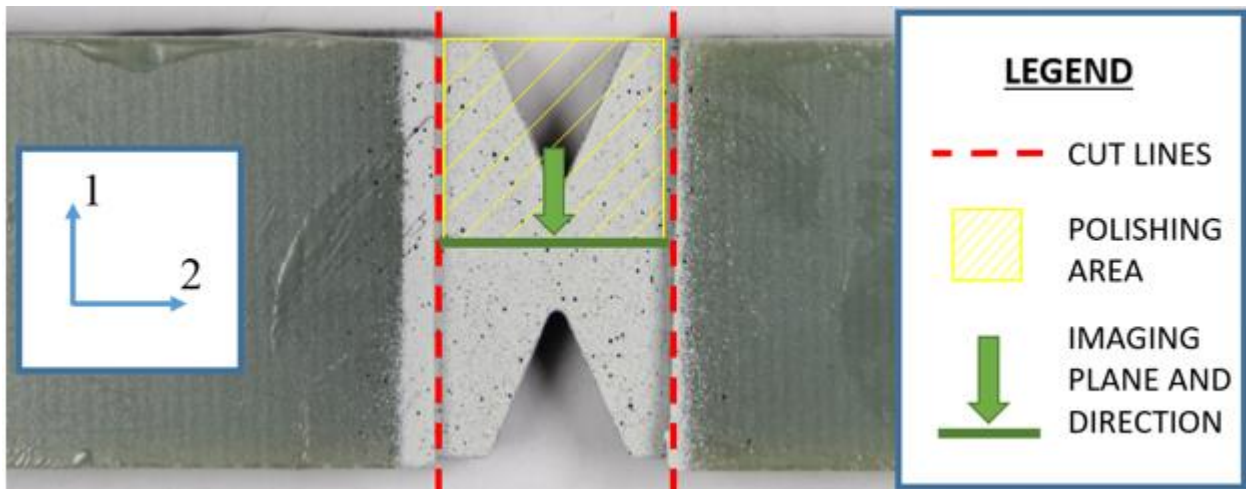


Figure 128. Virgin sample cutting layout

The interface of the interlaminar layer and two layers of the fiber composite is shown in Figure 129. No damage was found in this image.

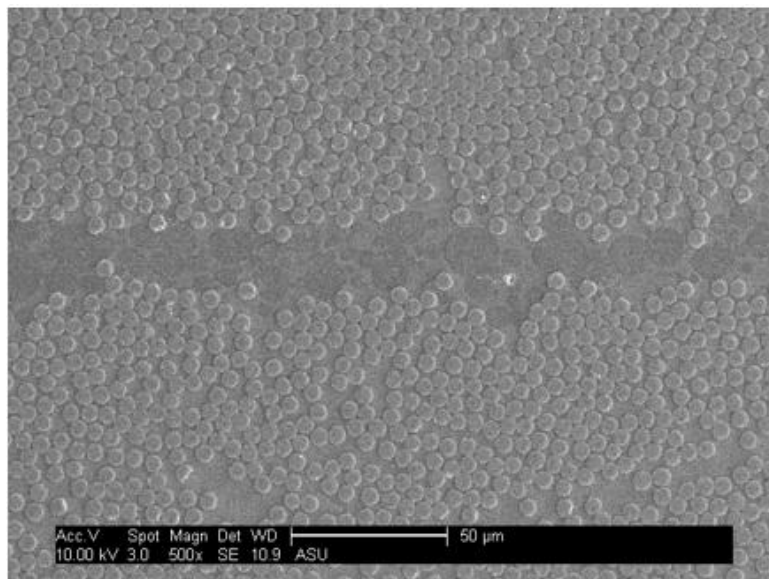
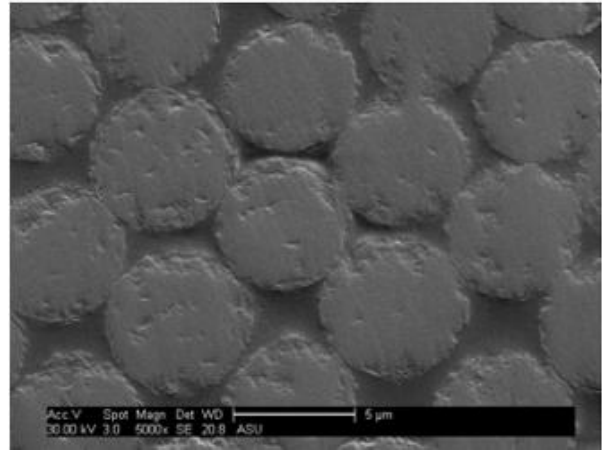
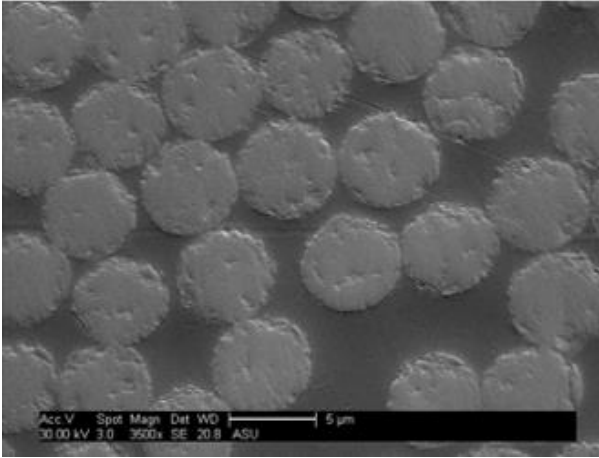


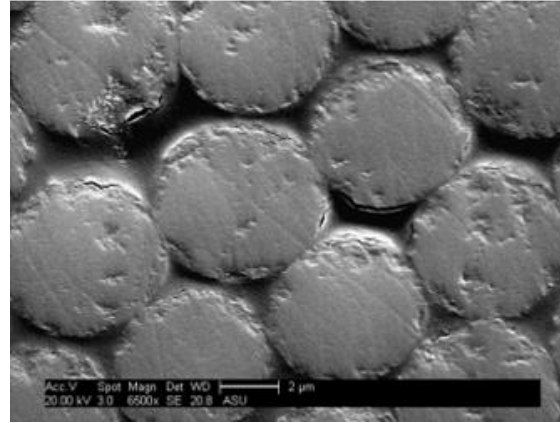
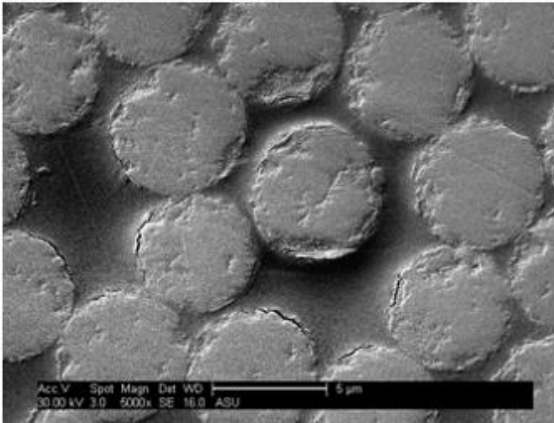
Figure 129. Virgin sample 500x

The majority of the surface area of the viewing plane showed no damage to the fibers or matrix. Figure 130 shows two images of undamaged areas of the sample at different magnifications.



(a) (b)
Figure 130. Virgin sample (a) 3500x (b) 5000x

Though not common, some areas of the virgin sample showed damage. The only damage visible on the sample was interfacial damage between fibers and matrix. Fiber debonding is shown in Figure 131.



(a) (b)
Figure 131. Virgin sample (a) 5000x (b) 6500x

Though there was debonding as shown in the images of Figure 131, the maximum portion of the perimeter debonded was approximately 1/8 of the total perimeter of the fiber. The debonding ratio refers to the ratio of the fiber perimeter length that is still bonded with the surrounding matrix to the fiber perimeter length that has become detached with the surrounding matrix. Thus, the fibers in Figure 131 have a maximum debonding ratio of 1/8 or 12.5%. It was undetermined whether this damage was inflicted during the manufacturing process or during the grinding and polishing of the sample. In either case, the virgin sample established a baseline for damage expected in an untested specimen.

7.3.2 Damaged sample

The post-test sample before the cutting process is shown in Figure 132.

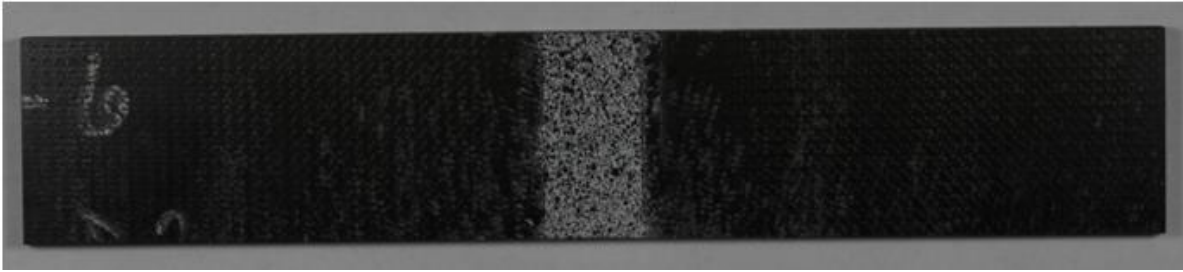


Figure 132. Damaged sample before cutting

The schematic of the cut lines and polishing area is shown in Figure 133. The sample was polished in the hatched region of this figure, up to the imaging plane.

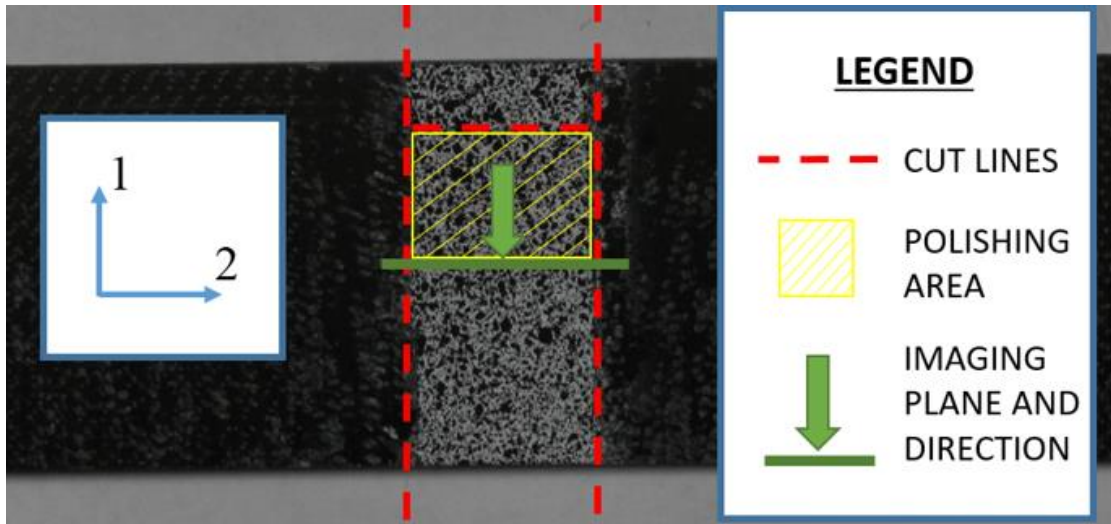
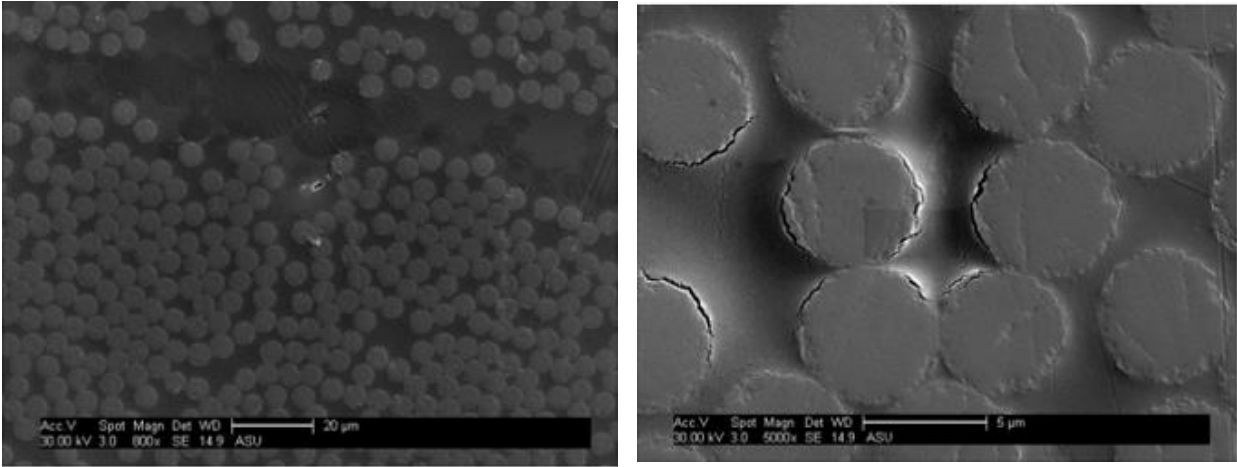


Figure 133. Damaged sample cutting layout

This sample showed more frequent and higher degree damage than the virgin sample in some areas, but the majority of the surface area of the imaging plane still showed no damage. The types of damage seen in the damaged sample were fiber debonding and matrix cracking

Figure 134(a) shows a small crack that had formed near the interlaminar layer. The crack is near the center of the image and is highlighted in white due to a charging effect of the SEM. Figure 134(b) shows an example found in the sample of fiber debonding. Comparing the fiber debonding in this image to that of Figure 131, it can be seen that the damaged sample sustained a larger degree of fiber debonding from the surrounding matrix. Some of these fibers had a debonding ratio of nearly 1/2 with the entire perimeter.



(a) (b)
Figure 134. Damaged sample (a) 800x (b) 5000x

Figure 135 shows another example of fiber debonding that appeared to be more extensive than the fiber debonding of the virgin sample.

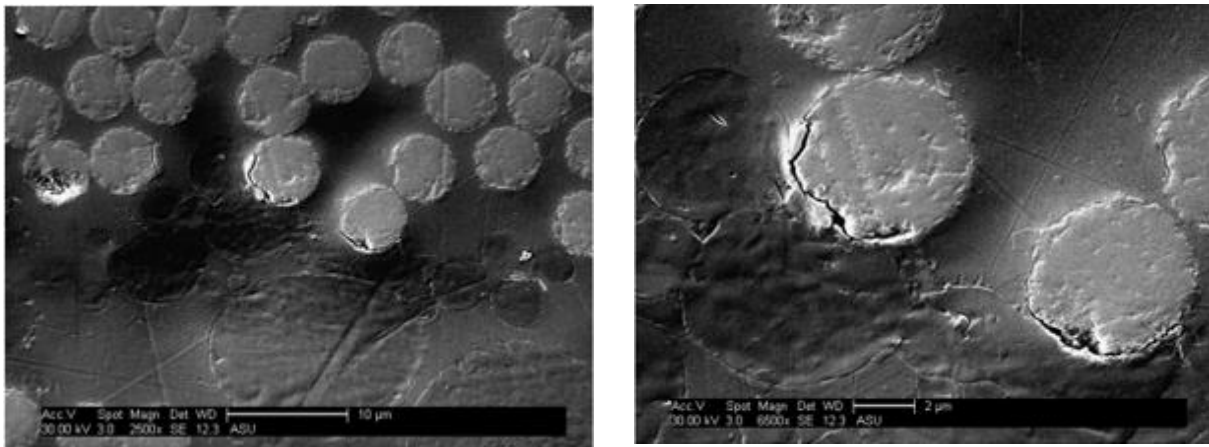


Figure 135. Damaged sample (a) 2500x (b) 6500x

The images of Figure 135 depict the same feature, with (a) providing a more magnified view. This image shows one of the fibers had debonded with a ratio of approximately 1/2 from the entire fiber perimeter.

7.3.3 Failed sample

The post-test sample before the cutting process is shown in Figure 136.

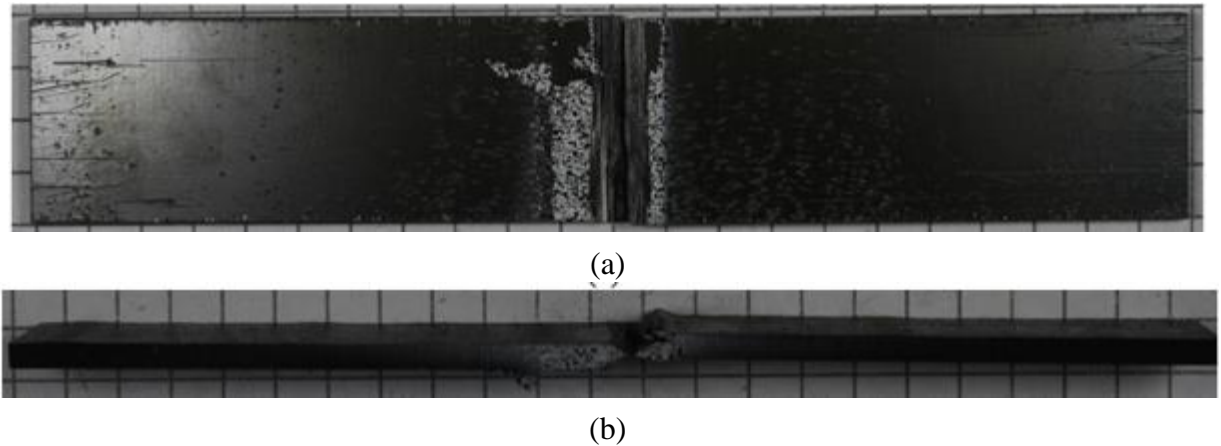


Figure 136. Failed sample before cutting (a) Width (b) Through thickness

Figure 137 shows the schematic of the cut lines and polishing area. The sample was polished in the hatched region of this figure, up to the imaging plane. This specimen was completely fractured, thus two pieces that were used for imaging.

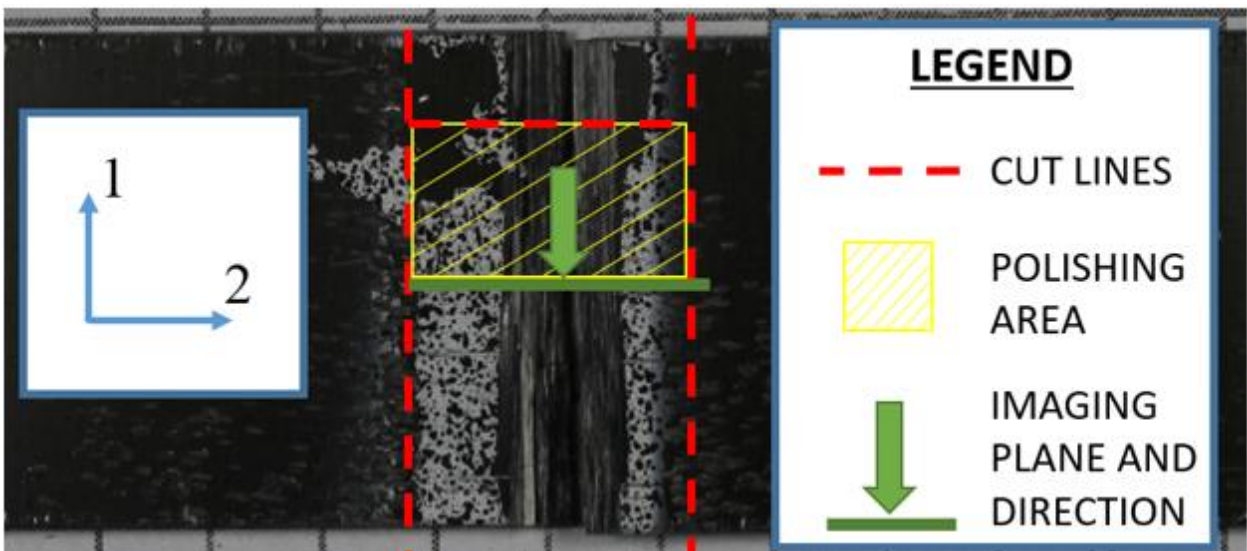


Figure 137. Failed sample cutting layout

Figure 138 shows the failed sample at the location near one of the cut lines from Figure 137. The image shows that a large crack formed and propagated almost entirely through the thickness of the specimen. Some of the crack filled with epoxy during the specimen embedding process. Air voids in the epoxy during curing left some of the crack void of any material (these are the darker spots surrounded by a white layer in Figure 138). The original test of this coupon was a 2-direction compression test, thus this large crack may have formed because of buckling of the composite.

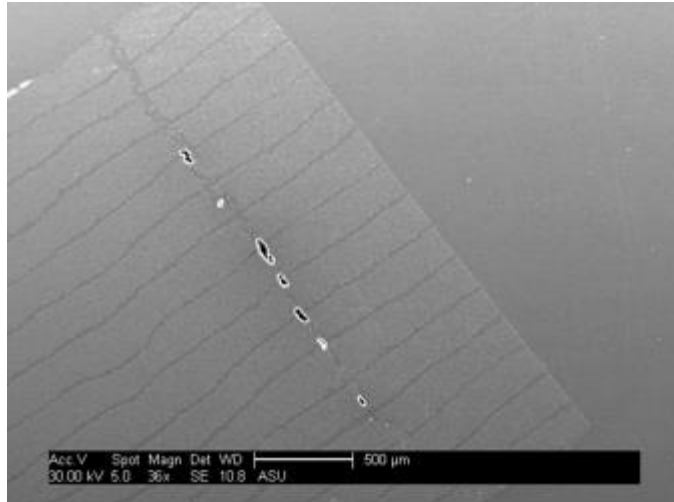
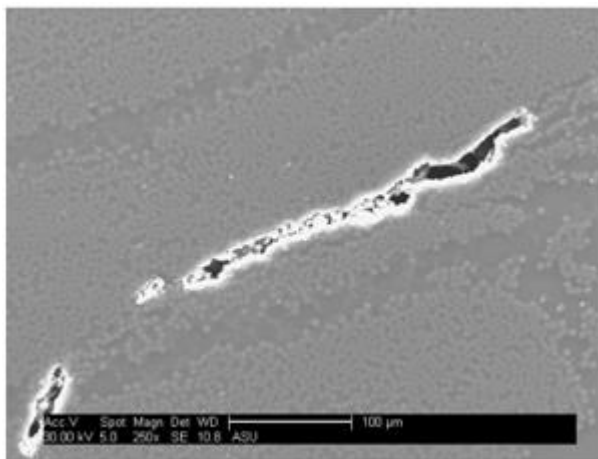
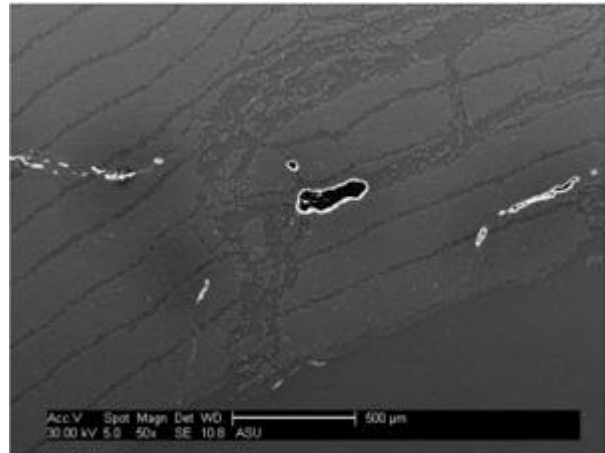


Figure 138. Failed sample 36x damage away from complete fracture zone

The failed specimen showed extensive damage of all kinds. Matrix damage included large cracks and openings between fibers, both interlaminar and intralaminar. Figure 139 shows extensive matrix damage. Figure 139(a) shows a large crack and opening occurring as intralaminar matrix damage. Figure 139(b) shows a variety of inter and intralaminar cracking.



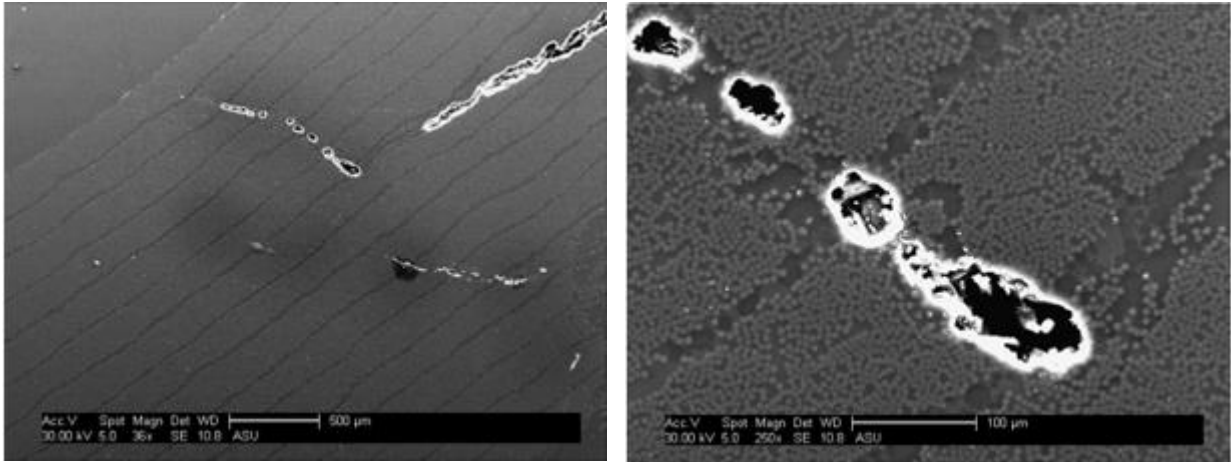
(a)



(b)

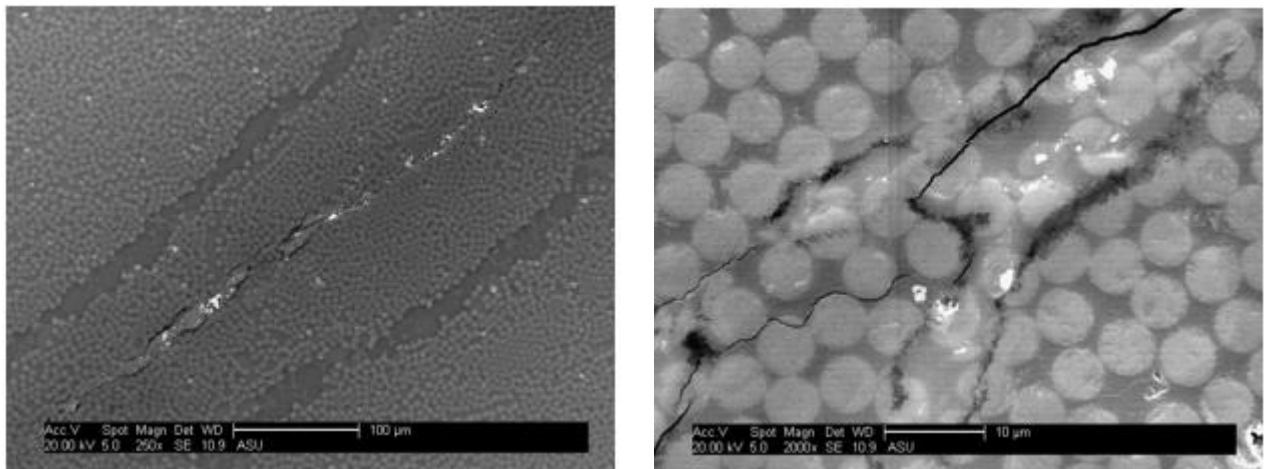
Figure 139. Failed sample (a) 250x (b) 50x

Large cracks also formed perpendicular to the composite layers and extended over multiple layers. Figure 140 shows this perpendicular crack formation.



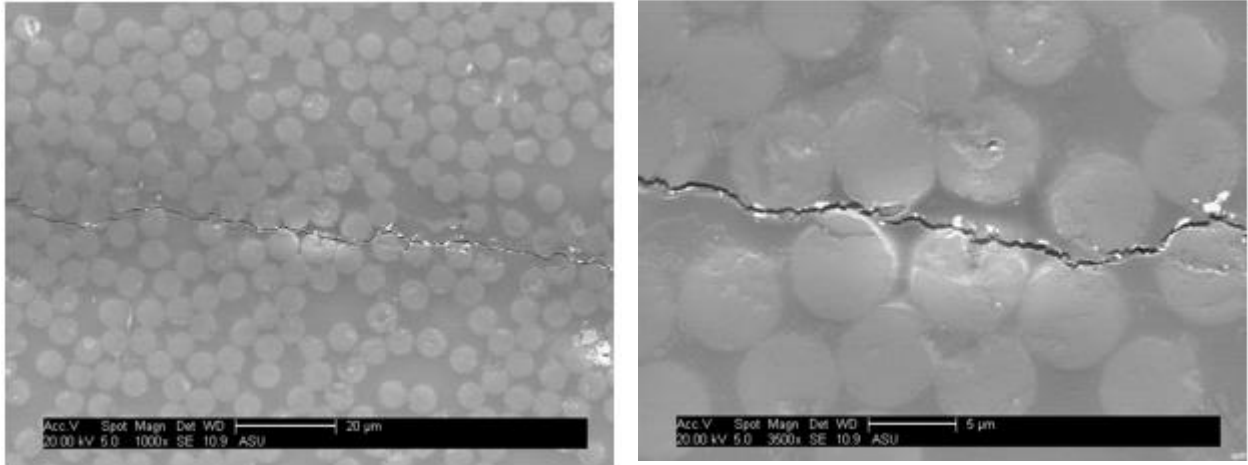
(a) (b)
Figure 140. Failed sample (a) 36x (b) 250x

In addition to the cracks that formed large openings between fibers. Matrix cracking also occurred that took the form of thin cracks between fibers. Figure 141 shows this type of matrix crack. Figure 141(a) depicts the crack from a lower magnification and shows that it is parallel with the composite layers. Figure 141(b) shows the crack at a higher magnification. This figure shows that the crack primarily winds around fibers, but there are some fibers that the crack splits.



(a) (b)
Figure 141. Failed sample (a) 250x (b) 2000x

This thin type of crack shown in Figure 141 as occurring parallel to the composite layers also occurred at an angle to the composite layers. Figure 142 shows a thin crack at different levels of magnification that occurred at an angle of approximately 45° to the composite layers.

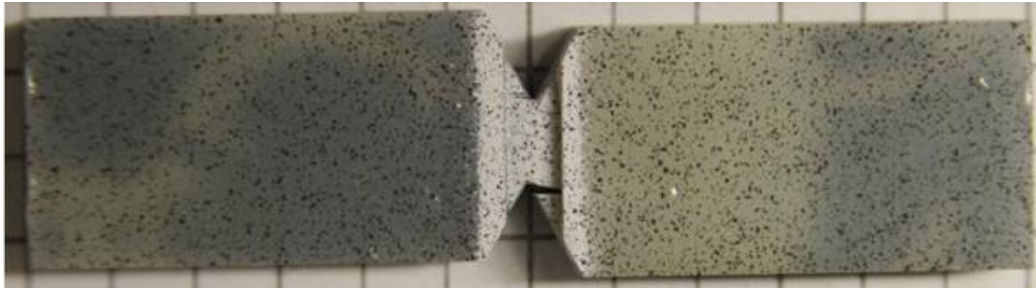


(a) (b)
Figure 142. Failed sample (a) 1000x (b) 3500x

The angle of the crack in Figure 142 is known because it was taken at the same angle with the composite as in Figure 141, where the layers are approximately at a 45° angle with the image frame. Since the crack shown in Figure 142 is nearly horizontal compared to the image frame, the crack and composite layers were approximately at a 45° angle with each other.

7.3.4 Failed shear sample

Figure 143 shows the post-test sample before the cutting process.



(a)



(b)

Figure 143. Failed-shear sample before cutting (a) Whole specimen (b) Gage area

The schematic of the cut lines and polishing area is shown in Figure 144. The sample was polished in the hatched region of this figure, up to the imaging plane.

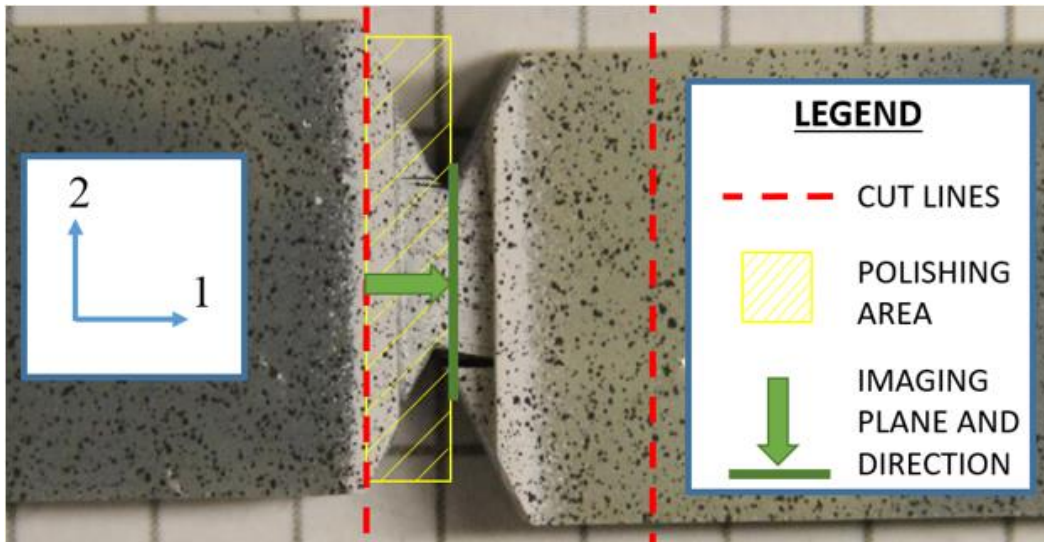
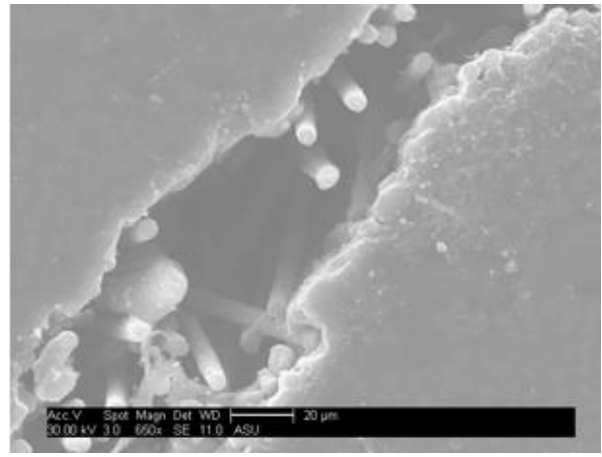
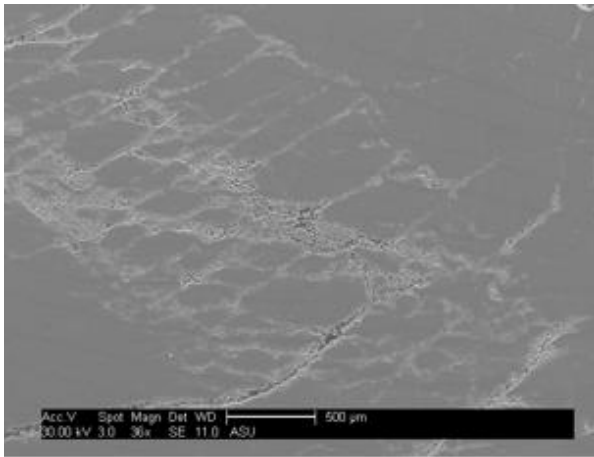


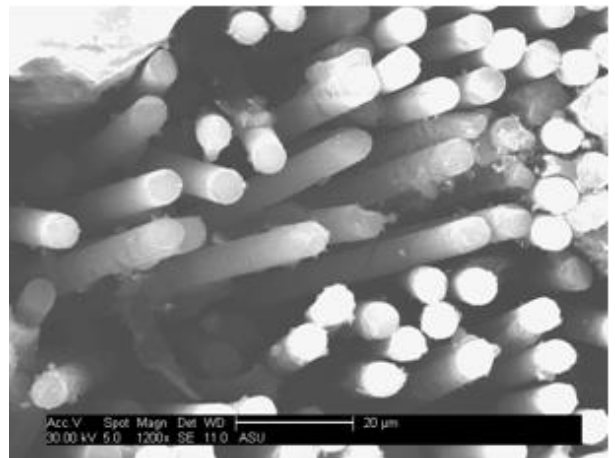
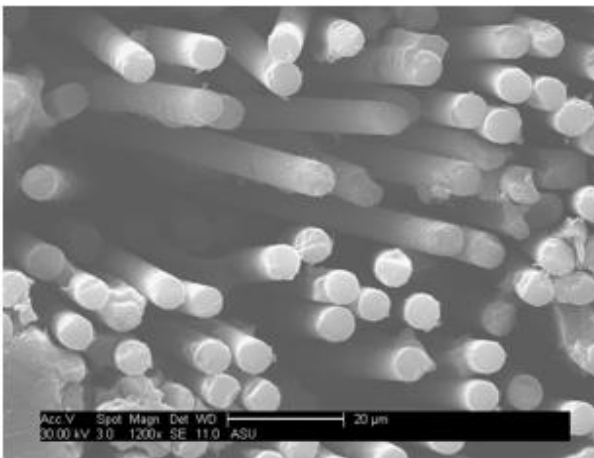
Figure 144. Failed-shear sample cutting layout

The failed-shear sample showed extensive damage in different forms than the other specimens. Figure 145(a) shows the overall specimen with an overall damage pattern at an approximately 30° angle with the composite layers. Extensive interlaminar matrix cracking is shown at a low magnification. Figure 145(b) shows that unlike the other test coupons, the fiber orientation changed during the test. Instead of only seeing the top surface of the fibers, they are seen to be at an angle with the image and extend into the image to some depth.



(a) (b)
Figure 145. Failed-shear sample (a) 36x (b) 650x

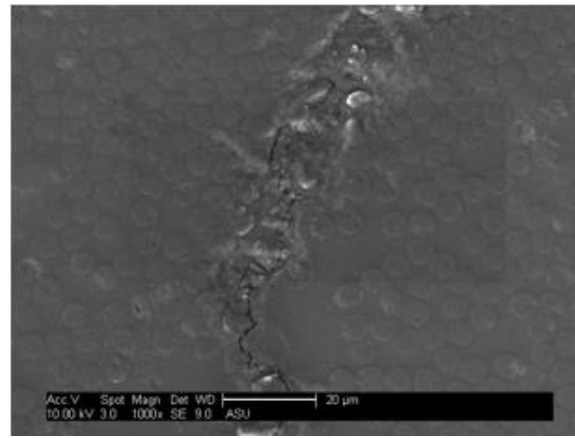
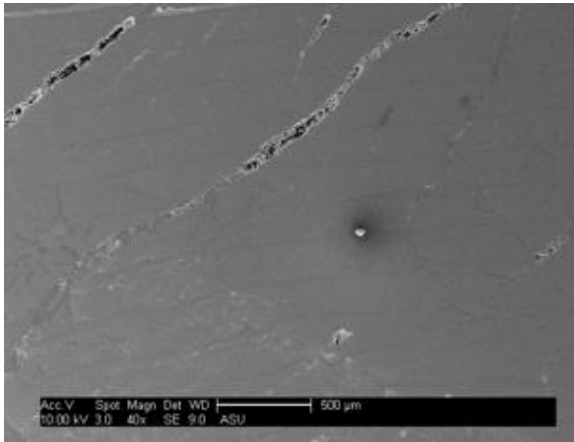
Figure 146 shows more examples of fibers skewed at an angle. Generally, the fibers appear skewed parallel with the composite layers. This was towards the direction of loading during the shear test.



(a) (b)
Figure 146. Failed-shear sample (a) 1200x (b) 1200x

The skewed angle of the fibers was expected as the material strength of the composite increased near the end of the shear test. The expectation was that the fibers were re-orientated so that they were in tension at the end of the test. This theory was confirmed with the images of Figure 145 and Figure 146

Matrix cracking was another type of damage seen extensively in the failed-shear specimen. Figure 147 depicts matrix cracking that led to large openings between fibers Figure 147(a) and thin matrix cracking winding between fibers Figure 147(b).



(a) (b)
Figure 147. Failed-shear sample (a) 40x (b) 1000x

8 Concluding remarks

This report summarized the details of the stacked-ply validation tests for MAT213 conducted at room temperature and at quasi-static loading conditions. Comparison metrics between experimental and simulated results included stress-strain relationships, strain profiles, and displacements.

Higher magnitude stresses and strains induced in the direction of loading were well predicted by MAT213 simulations. Lower magnitude strains induced in the transverse direction showed larger differences when compared to MAT213 simulations. In some cases, the MAT213 simulated results under predicted transverse strains measured in the experiments.

Initiation G_C values were obtained from ENF and DCB tests for mode I and mode II fracture of the interlaminar layers of the fiber reinforced material. Pre-cracked values were used from both tests as the critical energy release rate in cohesive zone models for interlaminar layers. The average experimental G_{IIC} value from the ENF tests was 10.50 psi-in. The average experimental G_{IC} value from the DCB test was 2.65 psi-in using the maximum load definition of crack initiation and the compliance calibration method of calculation. The ENF and DCB tests were modeled in LS-DYNA and used to calibrate other cohesive zone parameters to match experimental data.

SEM analysis revealed that some damage existed in untested specimens either from the manufacturing process or from grinding and polishing of the sample. However, a sample from a test coupon of the damage characterization tests revealed that there was more damage in this specimen in the form of matrix cracking and fiber interface decohesion.

9 References

- Achard, V., Bouvet, C., Castanié, B., & Chirol, C. (2014). Discrete ply modelling of open hole tensile tests. *Composite Structures*, *113*, 369-381. doi:10.1016/j.compstruct.2014.03.031
- Arrese, A., Boyano, A., De Gracia, J., & Mujika, F. (2017). A novel procedure to determine the cohesive law in DCB tests. *Composites Science and Technology*, *152*, 76-84.
- ASTM. (2011). D5766/D5766M-11 Standard Test Method for Open-Hole Tensile Strength of Polymer Matrix Composite Laminates. West Conshohocken, PA: ASTM International.
- ASTM. (2013). *D5528-13 Standard Test Method for Mode I Interlaminar Fracture Toughness of Unidirectional Fiber-Reinforced Polymer Matrix Composites*; . West Conshohocken, PA, 2013: ASTM International.
- ASTM. (2014). D6484/D6484M-14 Standard Test Method for Open-Hole Compressive Strength of Polymer Matrix Composite Laminates. West Conshohocken, PA: ASTM International.
- ASTM. (2014). D7905/D7905M-14 Standard Test Method for Determination of the Mode II Interlaminar Fracture Toughness of Unidirectional Fiber-Reinforced Polymer Matrix Composites. West Conshohocken, PA: ASTM International.
- ASTM. (2016). D3410/D3410M-16 Standard Test Method for Compressive Properties of Polymer Matrix Composite Materials with Unsupported Gage Section by Shear Loading. West Conshohocken, PA: ASTM International.
- ASTM. (2016). D6641/D6641M-16e1 Standard Test Method for Compressive Properties of Polymer Matrix Composite Materials Using a Combined Loading Compression (CLC) Test Fixture. West Conshohocken, PA: ASTM International.
- ASTM. (2017). D3039/D3039M-17 Standard Test Method for Tensile Properties of Polymer Matrix Composite Materials. West Conshohocken, PA: ASTM International.
- Bruyneel, M., Delsemme, J. P., Goupil, A. C., Jetteur, P., Lequesne, C., Naito, T., & Urushiyama, Y. (2014). Damage Modeling of Laminated Composites: Validation of the Intra-Laminar Law of SAMCEF at the Coupon Level for UD Plies. *Proceedings of the European Conference on Composite Material, ECCM16*.
- Chiu, L. N., Falzon, B. G., Chen, B., & Yan, W. (2016). Validation of a 3D damage model for predicting the response of composite structures under crushing loads. *Composite Structures*, *147*, 65-73. doi:10.1016/j.compstruct.2016.03.028

- Clay, S. B., & Knoch, P. M. (2017). Experimental results of quasi-static testing for calibration and validation of composite progressive damage analysis methods. *Journal of Composite Materials*, 51(10), 1333-1353. doi:10.1177/0021998316658539
- Correlated Solutions. (n.d.). Retrieved June 27, 2018, from <http://correlatedsolutions.com/>
- Deivanayagam, A., Vaidya, A., & Rajan, S. D. (2014). Enhancements to Modeling Dry Fabrics for Impact Analysis. *Journal of Aerospace Engineering*, 27, 484-490. doi:10.1061/(ASCE)AS.1943-5525.0000350
- Experimental Calibration of Cohesive Zone Models. (n.d.). Retrieved June 27, 2018, from <http://www.veryst.com/project/cohesive-zone-model-calibration>
- Goldberg, R. K., Carney, K. S., DuBois, P., Hoffarth, C., Harrington, J., Rajan, S., & Blankenhorn, G. (2016). Development of an Orthotropic Elasto-Plastic Generalized Composite Material Model Suitable for Impact Problems. *Journal of Aerospace Engineering*, 29(4), 04015083. doi:10.1061/(ASCE)AS.1943-5525.0000580
- Harrington, J., Hoffarth, C., Rajan, S. D., Goldberg, R. K., Carney, K. S., DuBois, P., & Blankenhorn, G. (2017). Using Virtual Tests to Complete the Description of a Three-Dimensional Orthotropic Material. *Journal of Aerospace Engineering*, 30(5), 04017025. doi:10.1061/(ASCE)AS.1943-5525.0000737
- Hoffarth, C., Rajan, S. D., Goldberg, R. K., Revilock, D., Carney, K. S., DuBois, P., & Blankenhorn, G. (2016). Implementation and validation of a three-dimensional plasticity-based deformation model for orthotropic composites. *Composites Part A: Applied Science and Manufacturing*, 91, 336-350. doi:10.1016/j.compositesa.2016.10.024
- Hongkarnjanakul, N., Bouvet, C., & Rivallant, S. (2013). Validation of low velocity impact modelling on different stacking sequences of CFRP laminates and influence of fibre failure. *Composite Structures*, 106, 549-559. doi:10.1016/j.compstruct.2013.07.008
- Jollivet, T., Peyrac, C., & Lefebvre, F. (2013). Damage of Composite Materials. *Procedia Engineering*, 66, 746-758. doi:10.1016/j.proeng.2013.12.128
- Kageyama, K., Kikuchi, M., & Yanagisawa, N. (1991). Stabilized End Notched Flexure Test: Characterization of Mode II Interlaminar Crack Growth. *Composite Materials: Fatigue and Fracture (Third Volume)*. doi:10.1520/STP17720S

- Khaled, B., Shyamsunder, L., Schmidt, N., Hoffarth, C., & Rajan, S. (n.d.). Experimental Tests to Characterize the Behavior and Properties of T800-F3900 Toray Composite. Arizona State University.
- Ladeveze, P., & LeDantec, E. (1992). Damage modelling of the elementary ply for laminated composites. *Composites science and technology*, 43, 257-267.
- León Becerra, J., González-Estrada, O. A., & Pertuz, A. (2019). Influence of the boundary condition on the first ply failure and stress distribution on a multilayer composite pipe by the finite element method. *Journal of Physics: Conference Series*, 1159(1), 012013. doi:10.1088/1742-6596/1159/1/012013
- Li, Q., Zhao, X., Xu, S., Leung, C. K., & Wang, B. (2019). Multiple impact resistance of hybrid fiber ultra high toughness cementitious composites with different degrees of initial damage. *Journal of Materials in Civil Engineering*, 31(2), 04018368. doi:10.1061/(ASCE)MT.1943-5533.0002576
- Livermore Software Technology Corporation. (n.d.). LS-DYNA Keyword User's Manual Volume II Material Models.
- LLorca, J., González, C., Molina-Aldareguía, J. M., & López, C. S. (2013). Multiscale Modeling of Composites: Toward Virtual Testing... and Beyond. *JOM*, 65(2), 215-225. doi:10.1007/s11837-012-0509-8
- Meo, M., & Thieulot, E. (2005). Delamination modelling in a double cantilever beam. *Composite Structures*, 71(3-4), 429-434.
- Nuggehalli Nandakumar, P. (2010). Rate sensitivity of the interlaminar fracture toughness of laminated composites. Doctoral dissertation, Wichita State University.
- O'Brien, T. K., Johnston, W. M., & Toland, G. J. (2010). *Mode II Interlaminar Fracture Toughness and Fatigue Characterization of a Graphite Epoxy Composite Material*. NASA.
- Sasser, D. (2015). Structural Analysis of Carbon Fiber-Epoxy Composite Surfaces with Polar Stacking Sequences. Doctoral dissertation University of Washington.
- Schmidt, N. (2016). Experimental Procedures and Data Analysis of Orthotropic Composites. Tempe, AZ: Arizona State University.

- Schuecker, C., & Davidson, B. (2001). Effect of Friction on the Perceived Mode II Delamination Toughness from Three- and Four-Point Bend End-Notched Flexure Tests. *Composite structures: theory and practice*. doi: 10.1520/STP14518S
- Serra, J., Pierré, J. E., Passieux, J. C., Périé, J. N., Bouvet, C., Castanié, B., & Petiot, C. (2017). Validation and modeling of aeronautical composite structures subjected to combined loadings: The VERTEX project. Part 2: Load envelopes for the assessment of panels with large notches. *Composite Structures*, 180, 550-567. doi:10.1016/j.compstruct.2017.08.055
- Sun, C. T., & Zheng, S. (1996). Delamination characteristics of double-cantilever beam and end-notched flexure composite specimens. *Composites Science and Technology*, 56(4), 451-459. doi:10.1016/0266-3538(96)00001-2
- T. C. M. America. (n.d.). Retrieved from <https://www.toraycma.com>
- Tamuzs, V., Tarasovs, S., & Vilks, U. (2001). Progressive delamination and fiber bridging modeling in double cantilever beam composite specimens. *Engineering Fracture Mechanics*, 513-525. doi:10.1016/S0013-7944(00)00131-4
- Wasseem H.S., M., & Kumar N., K. (n.d.). FEM for Delamination Analysis of Double Cantilever Beam | Fracture Mechanics | Fracture. Retrieved June 27, 2018, from <https://www.scribd.com/document/270149618/FEM-for-Delamination-Analysis-of-Double-Cantilever-Beam>
- Yoshihara, H., & Satoh, A. (2009). Shear and crack tip deformation correction for the double cantilever beam and three-point end-notched flexure specimens for mode I and mode II fracture toughness measurement of wood. *Engineering Fracture Mechanics*, 76(3), 335-346. doi:10.1016/j.engfracmech.2008.10.012
- Zabala, H., Aretxabaleta, L., Castillo, G., & Aurrekoetxea, J. (2016). Dynamic 4 ENF test for a strain rate dependent mode II interlaminar fracture toughness characterization of unidirectional carbon fibre epoxy composites. *Polymer Testing*, 55, 212-218. doi:10.1016/j.polymertesting.2016.09.001